



HAL
open science

Partial oxidation of methane in a dielectric barrier discharge plasma milli-reactor

Erick Osvaldo Martinez Ruiz

► **To cite this version:**

Erick Osvaldo Martinez Ruiz. Partial oxidation of methane in a dielectric barrier discharge plasma milli-reactor. Chemical engineering. Université Pierre et Marie Curie - Paris VI, 2017. English. NNT : 2017PA066736 . tel-02999129

HAL Id: tel-02999129

<https://theses.hal.science/tel-02999129>

Submitted on 10 Nov 2020

HAL is a multi-disciplinary open access archive for the deposit and dissemination of scientific research documents, whether they are published or not. The documents may come from teaching and research institutions in France or abroad, or from public or private research centers.

L'archive ouverte pluridisciplinaire **HAL**, est destinée au dépôt et à la diffusion de documents scientifiques de niveau recherche, publiés ou non, émanant des établissements d'enseignement et de recherche français ou étrangers, des laboratoires publics ou privés.

Université Pierre et Marie Curie

Ecole Doctorale 391 - Sciences Mécaniques, Acoustique, Electronique et
Robotique

Equipe 2PM / IRCP UMR8247 (CNRS-Chimie ParisTech)

Oxydation partielle du méthane dans un milli-réacteur plasma de type décharge à barrière diélectrique.

*Partial oxidation of methane in a dielectric barrier discharge
plasma milli-reactor.*

Par **Erick Osvaldo MARTINEZ RUIZ**

Thèse de doctorat en Génie des Procédés

Dirigée par Stéphanie OGNIER

Présentée et soutenue publiquement le 23 mai 2017

Devant un jury composé de :

M. COMMENGE Jean-Marc	Professeur Université de Lorraine	Rapporteur
M. FULCHERI Laurent	Maître de conférences HDR MINES ParisTech	Rapporteur
Mme. GALVEZ Maria Elena	Maître de conférences HDR UPMC	Examineur
Mme. OGNIER Stéphanie	Maître de conférences HDR ENSCP	Examineur
M. TATOULIAN Michaël	Professeur ENSCP	Examineur



Except where otherwise noted, this work is licensed under
<http://creativecommons.org/licenses/by-nc-nd/3.0/>

A mi familia.
Especialmente a mis abuelos
Naxaria y Jesús.

Acknowledgments

Je tiens à remercier en premier lieu ma directrice de thèse : Madame Stéphanie OGNIER, Maître de conférences HDR ENSCP pour toutes les heures qu'elle a consacrées à diriger cette recherche. Monsieur Michaël TATOULIAN, Professeur ENSCP et Directeur de l'équipe Procédés, Plasmas et Microsystèmes pour m'avoir accueilli au sein du laboratoire et pour ses précieux conseils tout au long de cette thèse.

J'adresse mes sincères remerciements à Monsieur Jean-Marc COMMENGE, Professeur Université de Lorraine et à Monsieur Laurent FULCHERI, Professeur à MINES ParisTech pour l'honneur qu'ils m'ont fait en acceptant d'être rapporteurs et membres du jury de ce travail.

Mes remerciements s'adressent également à Madame Maria Elena GALVEZ, Maître de conférences à l'Université de Pierre et Marie Curie, pour avoir accepté de participer au jury de ce mémoire de thèse.

Je remercie Monsieur Safwan AL AYOUBI et Monsieur Simeon CAVADIAS, pour leur aide et leurs conseils. Merci pour le temps consacré à cette thèse.

Je ne saurais oublier que ce travail a été possible grâce au soutien financier du Consejo Nacional de Ciencia y Tecnología (CONACyT).

Personal Acknowledgments

Gracias a Imelda Ortiz por ser mi gran pilar en esta gran aventura. Tantas experiencias compartidas, así como, batallas superadas, definitivamente nunca lo olvidaré. Esto no lo hubiera logrado sin ti.

Un gran gracias a mis otros tres pilares Guillaume Schelcher, Olivier Lesage y XI Rao. Ustedes forman parte de mi familia, gracias por enseñarme el profundo valor de su cultura e historia, por siempre serán mis hermanos.

Un especial gracias a Cedric Guyon y Frédéric Rousseau, el binomio incondicional que tanto admiro como profesional como humanamente.

Gracias a todo el equipo de Génie des procédés del CNAM dirigido por Jean-Louis Havet, los cuales siempre me acogieron y brindaron su apoyo, tanto moral como académico.

Gracias a Bradley y Alex por su aportación en contrastes ideológicos, y su siempre soporte moral que me brindaron.

Gracias a Aurelien y Julien, los cuales fueron de gran importancia, para lograr a la perfección el “Último estirón” en esta aventura.

Gracias a Mengxue por sus aportes teóricos, experimentales y a veces “políticos” para el buen desarrollo de mi trabajo.

Gracias a Axelle, Charlotte, Dhia, Diane, Jonathan, Maxime, Rafik, Wael, Sylvan, Paul, Matis, Manon (gracias por los postres), Stuart, Ines, y Magdalena. Por simplemente ser quienes son y transmitirme su valía.

Un Especial gracias a Phat que en este último trayecto formo parte importante en mi guía a la meta final.

Gracias a todos mis amigos tan cercanos que en todo momento me tendieron todo su apoyo incondicional: Kader (Adrien), Xavier, Olivier, Charles Cavaniol.

Abstract

Methane gas is known to be the most destructive greenhouse gas. The current world reserves of natural gas, which contains mainly methane, are underutilized due to high transportation costs. Thus, considerable interest is presently shown in conversion of methane to transportable liquid fuels and chemicals of importance to the petrochemical industry. One of the main solution for this problem is the partial oxidation of methane, actually this reaction requires a very high pressures and temperatures.

The partial oxidation of methane (POM) in a milli-plasma environment is one possible route for converting methane to more valuable higher hydrocarbons at room temperature and atmospheric pressure.

In that context, a Dielectric Barrier Discharge (DBD) transparent plasma-millireactor was designed for methane partial oxidation. A mixture of $O_2/CH_4/Ar$ was processed into the reactor. AC high voltage (10.8 kV, 3 kHz) was applied to generate the plasma discharge. Under our experimental conditions, a highly reactive environment at room temperature and atmospheric pressure was generated, leading to methane conversion as high as 30 percent. The main products of the reaction were identified as methanol, ethane, ethane, propane, hydrogen, CO and CO_2 . The influence of the specific input energy ($J/mol_{methanein}$), the gas composition and flow rate on the methanol selectivity and methane conversion were studied.

Comsol Multiphysics 5.1 was used as a simulation tool to perform a first study to understand the mechanism of the reaction involved in POM for the production of methanol. Two main models were discussed, the sinusoidal and multi-time scale models. This work defines the bases for the understanding of the POM for the production of methanol. This study generates new alternatives in the use of miniaturization technologies in order to efficiently convert methane to methanol.

Résumé

Le gaz méthane est connu comme le gaz à effet de serre le plus ravageur. Les réserves mondiales actuelles de gaz naturel, qui contient principalement du méthane, sont sous-utilisées en raison des coûts de transport élevés. Subséquemment, un intérêt important est démontré dans la conversion du méthane en carburants liquides transportables et en produits chimiques d'importance pour l'industrie pétrochimique. L'une des principales solutions à ce problème est l'oxydation partielle du méthane (POM acronyme en anglais), cette réaction nécessite des pressions et des températures très élevées.

L'oxydation partielle du méthane dans un milieu milli-plasma est une voie possible pour convertir le méthane en hydrocarbures supérieurs avec plus de valeur à conditions de température ambiante et pression atmosphérique. Dans ce contexte, un milli-réacteur plasma de type décharge à barrière diélectrique a été conçu pour l'oxydation partielle du méthane. Un mélange d' $O_2 / CH_4 / Ar$ a été utilisé, à une haute tension CA (10,8 kV, 3 kHz) pour générer la décharge du plasma. Dans les conditions expérimentales, un environnement hautement réactif à température ambiante et pression atmosphérique a été généré, ce qui a conduit à une conversion du méthane jusqu'à 30 %. Les principaux produits de la réaction ont été identifiés comme le méthanol, l'éthane, l'éthane, le propane, l'hydrogène, le CO et le CO_2 . L'influence de l'énergie d'entrée spécifique ($J / mol_{methanein}$), la composition du gaz, le débit sur la sélectivité au méthanol et la conversion du méthane ont été étudiés. Comsol Multiphysics 5.1 a été utilisé comme outil de simulation pour effectuer une première étude pour comprendre le mécanisme de la réaction impliquée dans la POM pour la production de méthanol. Deux modèles principaux ont été discutés, les modèles à l'échelle sinusoïdale et multi-temps. Ce travail définit les bases de la compréhension du POM pour la production de méthanol. Cette étude génère de nouvelles alternatives dans l'utilisation des technologies de miniaturisation afin de transformer efficacement le méthane en méthanol.

General introduction

The objective of this research was to build and study an atmospheric pressure non-thermal dielectric barrier discharge (DBD) plasma millireactor aimed to produce methanol by partial oxidation of methane.

Today, it is evidently noticed that public sensitivity regarding environmental issues has increased substantially in comparison with a recent past, due to the drastic exploitation and depletion of fossil fuels including oil and coal which have a great influence on environmental problems such as the global warming.

In addition as a consequence of burning of these carbon-based fuels the concentration of greenhouse gases increases mainly those concerning CO₂ and CH₄, the second one has until 30 more impact effect in the global warming phenomena in comparison to CO₂. In the other hand, a renewed interest in gas-to-liquid processes has been initiated by the increasing legislation for cleaner energy sources, which includes the production of liquid fuels from biomass derived sources. Another reason for interest in these reactions comes from the natural gas industry, where gas-to-liquid conversions, if carried out at remote offshore locations, could enable some governments to profit from stranded natural gas reserves at oil wells where the natural gas by-product is otherwise flared

However, methane is a very stable molecule due to the high strength of the four C-H bonds. Adverse reaction conditions are necessary in order to overcome the high activation energies required to break these bonds. Established industrial methods for methane reforming involve reacting CH₄ with steam or another oxidant under high temperatures, pressures and in the presence of catalysts that are prone to sintering and deactivation under these harsh operating conditions.

Nowadays, non-thermal discharges at atmospheric pressure are of great interest in many fields owing to the highly reactive environment provided at relatively low temperatures. Moreover, cold plasma processes are promising systems in order to be environmentally friendly and an energy saving processing route. Miniaturization of plasma reactors has the promise of producing the plasma at much lower voltages compared to a conventional scale reactor, thus achieving low power production. In addition, the milliscale dimensions increase the efficiency of both heat and mass transfer phenomena, and so provide a nearly isothermal and rapidly mixed

homogeneous environment allowing a better control of the chemical reactions. Thus, generation of plasma in micro and millichannels may lead to a better control of chemical transformations. Plasma reactors used as a milliscale source of ions, excited species and radicals open several opportunities for the chemical process intensification and could be an enabling technology across fundamental and applied sciences.

In that context, a Dielectric Barrier Discharge (DBD) plasma-millireactor was designed for the partial oxidation of methane. The millireactor was designed to operate at atmospheric pressure and possible temperature increases due to the nature of the reaction. It is possible to realize optical characterizations using a camera ICCD (intensified charge-coupled device) since the reactor possesses a transparent electrode elaborated with an alloy of Indium Tin Oxide (ITO)

In this thesis are studied and discussed the influence of the main operating variables of the DBD plasma millireactor for the POM for the production of methanol. Those variables are the composition of the reactive mixture, flow rate and injected power into the system. These variables were studied using characterization techniques such as gas chromatography (GC) and the use of the ICCD that allowed to evaluate the uniformity in the distribution of plasma discharges in the reactor.

There is also reported the use of Comsol Multiphysics 5.1 as a simulation tool to perform a first study to understand the mechanism of the reaction involved in POM for the production of methanol as well as the behavior of the intermediate species generated in the plasma discharge. In this thesis are proposed two main models to achieve this goal, the sinusoidal model and multi-time scale model. The advantages and disadvantages of each are discussed in this thesis.

Contents

Acknowledgments

Abstract

General Introduction

Chapter 1 : Literature review	15
1.1. Introduction	17
1.2. Natural gas	18
1.3. Global climate change	19
1.3.1. Biogas	22
1.4. Fischer-Tropsch processes	24
1.5. Industrial methanol synthesis	27
1.6. Introduction to plasma	28
1.6.1. Applications of plasma	29
1.6.2. Types of plasma	30
1.6.3. Generation of non-thermal plasma by electric fields.....	31
1.6.4. Townsend mechanism of electric breakdown	33
1.6.5. Continuous and pulsed direct current discharges.....	35
1.6.5.1. Corona discharges	36 37
1.6.5.2. Gliding arc discharges	39
1.6.5.3. Dielectric barrier discharges (DBD).....	40
1.6.5.3.1. Microdischarges	41
1.6.5.3.2. Memory effect in DBD plasma	41
1.7. Plasma chemistry for methanol production	42
1.7.1. Plasma reactor designs for partial oxidation of methane (POM).....	42
1.7.2. CH ₄ /O ₂ ratio	46
1.7.3. Noble gas effect.....	47
1.8. Conclusion	48
Chapter 2 : Analytical techniques	49
2.1. Plasma power measurements	51
2.2. Intensified charge coupled device (ICCD)	52
2.3. Gas chromatography	53
2.3.1. Micro-gas chromatography	55
2.3.2. Thermal conductivity detection	57
2.3.3. Flame ionization detection.....	58
2.4. Conclusion	59
Chapter 3 : Fabrication and performance of a DBD plasma milli-reactor	61
3.1. Introduction to milli-reactor development	63
3.2. Reactor fabrication	65
3.2.1. Plasma milli-reactor cellule fabrication.....	65
3.2.2. Borosilicate glass engraving	66
3.2.3. Electrode patterning.....	67
3.2.4. General description of the sputtering process.....	68
3.2.5. Electrode deposition for POM.....	69
3.2.6. Electrode deposition for discharge characterization	70
3.2.7. Sealing step.....	72

3.3. Electrical characterization of the reactor	73
3.3.1. Influence of the argon percentage on the electrical characteristics of the discharge..	77
3.3.2. Influence of the O ₂ /CH ₄	78
3.4. Characterization of discharge uniformity by ICCD measurements.....	78
3.4.1. ICCD measurements in pure gases.....	78
3.4.2. ICCD measurements CH ₄ /O ₂ /Ar mixture	79
3.5. Conclusion.....	82
Chapter 4 : Performance of the plasma milli-reactor for the partial oxidation of methane (POM).....	83
4.1. General performance for partial oxidation of methane (POM)	85
4.2. Methane to methanol in a plasma milli-reactor	89
4.2.1. Influence of flow rate on methanol selectivity (ICCD)	89
4.2.2. Influence of argon concentration on methanol selectivity	93
4.2.3. Influence of the O ₂ /CH ₄ ratio on methanol selectivity.....	96
4.3. Conclusion.....	99
Chapter 5 : Simulation of a DBD plasma milli-reactor for POM.....	101
5.1. Introduction to the simulation of a DBD plasma milli-reactor.....	103
5.2. Description of the filamentary aspect of DBD plasma	103
5.3. The DBD plasma modelling	104
5.3.1. Governing equations	105
5.3.2. Electron transport equations	105
5.3.3. Diffusive transport equations for heavy species.....	107
5.3.4. Poisson's equations and surfaces boundary conditions for DBD plasma	108
5.3.5. Chemical kinetics and source term treatment	110
5.4. Introduction to numerical simulation (plasma module COMSOL Multiphysics 5.1) and description of the different modeling approaches	111
5.4.1. Sinusoidal model	113
5.4.2. Multi-time scale model.....	114
5.4.2.1. DBD model for the simulation of one microdischarge	115
5.4.2.2. 0D model for time evolution of chemical species	117
5.5. Simulation results.....	118
5.5.1. Results obtained with the sinusoidal model	118
5.5.2. Results obtained with the multi-time scale model	126
5.5.2.1. Energetic aspects.....	126
5.5.2.2. Production of primary radicals	129
5.5.3. Comparison of sinusoidal model and multi-time scale model.....	131
5.5.3.1. Energetic aspects.....	131
5.5.3.2. Production of stables species at low constant SIEM	132
5.6. Comparison of multi-time scale model results and experimental results	134
5.6.1. Methane conversion.....	134
5.6.2. Influence of Argon percentage on methanol selectivity	136
5.6.3. Influence of O ₂ /CH ₄ ratio on methanol selectivity	137
5.7. Conclusion.....	138

General conclusions and outlooks

References

Annex

Annex I:
Annex II:
Annex III:

List of figures

List of tables

Chapter 1 : Literature review

1.1. Introduction

Today, it is evidently noticed that public sensitivity regarding environmental issues has increased substantially in comparison with a recent past, due to the drastic exploitation and depletion of fossil fuels including oil and coal which have a great influence on environmental problems such as the global warming.

In addition as a consequence of burning of these carbon-based fuels the concentration of greenhouse gases increases mainly those concerning CO₂ and CH₄, the second one has until 30 more impact effect in the global warming phenomena in comparison to CO₂ [1]–[3]. This is one of the main reasons why the conversion of methane to value-added chemicals and fuels is considered to be one of the challenges of the twenty first century [4]. In the other hand, methane is the predominant component of natural gas and has formed a major part of the energy market for many years. In Britain, the discovery of natural gas in the North Sea in 1965 meant that a cleaner form of gas became accessible. At that time, town gas manufactured from coal was supplied to homes by a national network until a program for conversion to natural gas was completed in 1976. To this date, natural gas is distributed to homes where it is combusted in a highly exothermic reaction to provide energy for central heating, gas heating and cooking. It is also utilized in gas fired power stations to generate electricity for the national grid, where the energy released during combustion is used to drive a gas or steam turbine.

In the other hand, a renewed interest in gas-to-liquid processes has been initiated by the increasing legislation for cleaner energy sources, which includes the production of liquid fuels from biomass derived sources. Another reason for interest in these reactions comes from the natural gas industry, where gas-to-liquid conversions, if carried out at remote offshore locations, could enable some governments to profit from stranded natural gas reserves at oil wells where the natural gas by-product is otherwise flared.

However, methane is a very stable molecule due to the high strength of the four C-H bonds, which have an average bond enthalpy of 413 kJ mol⁻¹. Adverse reaction conditions are necessary in order to overcome the high activation energies required to break these bonds. Established industrial methods for methane reforming involve reacting CH₄ with steam or another oxidant under high temperatures, pressures and the presence of catalysts that are prone to sintering and deactivation under these harsh

operating conditions. Frequent replacement of spent catalysts and high energy consumption add to the overall running costs of methane reforming processes. Many research efforts are focused on the development of alternative technologies that allow methane reforming to proceed under milder reaction conditions, in attempt to make it a more economically favorable process.

There are several different industrial approaches to methane reforming; the challenges associated with these methods are reported in this chapter, which explains the motivation behind the research in this thesis.

1.2. Natural gas

Natural gas is defined as a gas obtained from a natural underground reservoir. It generally contains a large quantity of methane along with heavier hydrocarbons such as ethane, propane, isobutane, etc. Also, it often contains a considerable amount of non-hydrocarbons such as nitrogen, hydrogen and carbon dioxide [5]. Different types of fossil fuels including natural gas have been formed over millions of years, deep beneath the Earth's surface. **Figure 1.1** shows the natural gas proved reserves by geographical distribution. The most significant proportions are found in Middle East countries (80 trillion of m³), Europe & Eurasia (56 trillion of m³).

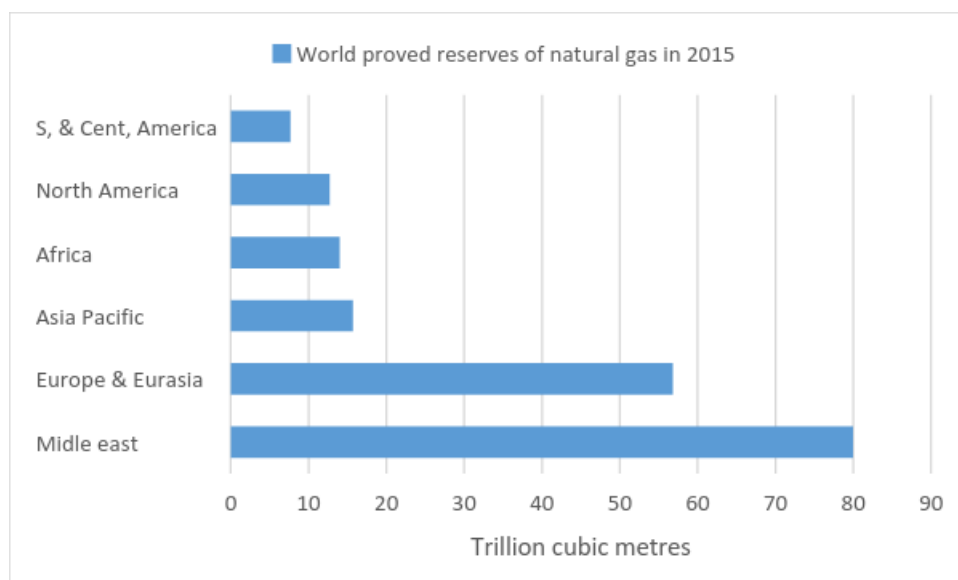


Figure 1.1. Proven world natural gas reserves by geographical region in 2015 [6] .

Environmental concerns as well as uncertainties about the sustainability and cost of future sources of natural gas have led to considerable interest to research the others alternatives of methane sources, such as the biogas production to cite an example.

1.3. Global climate change

Actually the main source of energy is based on the exploitation of oil, natural gas and carbon as reported in **figure 1.2**. However the combustion of natural gas and other fossil fuels for domestic, industrial and automotive energy demands creates considerable emissions of CO₂ (one of greenhouse gas). As a consequence carbon dioxide concentrations in the atmosphere have increased dramatically (more than what could be considered a natural fluctuation) since the use of fossil fuels became widespread and intensified.

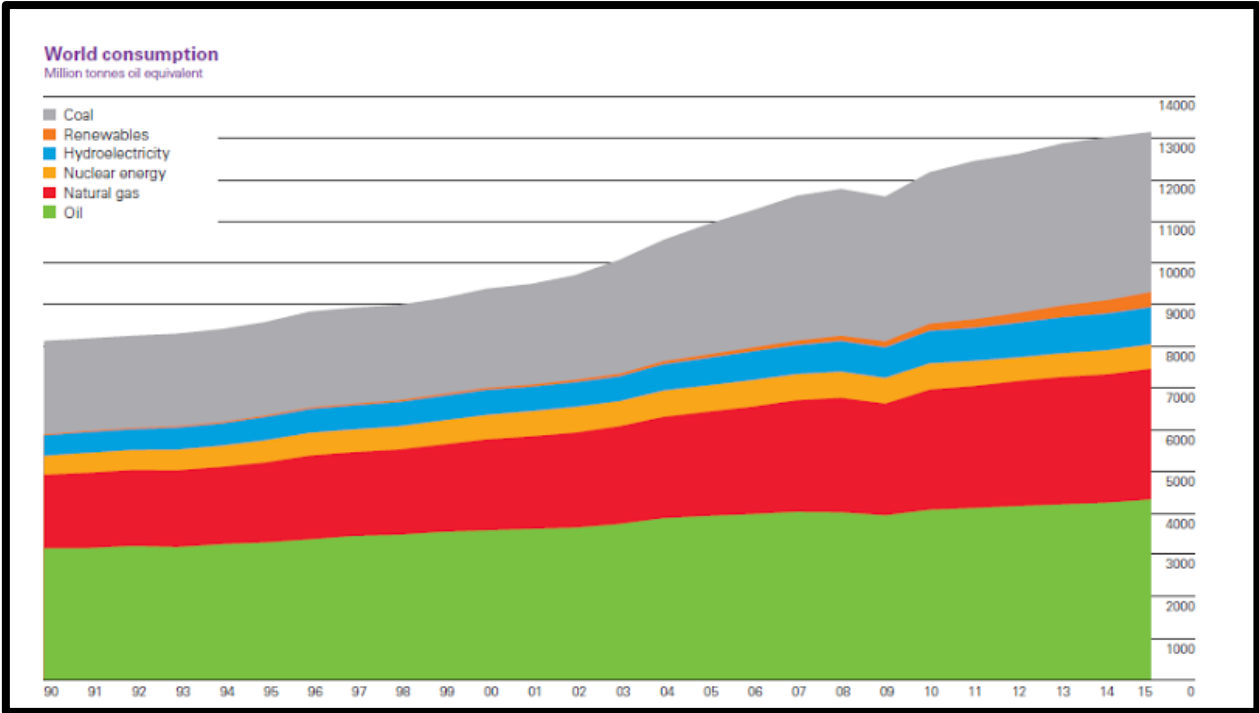


Figure 1.2. World primary energy consumption from 1990 to 2015 [6].

Naturally greenhouse gases exist in the atmosphere and have a key role in maintaining the energy balance on earth, by absorbing and reflecting radiation back to the Earth’s surface (**Figure 1.3**), a concept that is widely known as the greenhouse effect. The excessive greenhouse gases emission due to the anthropogenic activity, which

includes CO₂, methane, nitrous oxide (N₂O), Sulphur hexafluoride (SF₆), chlorofluorocarbons (CFCs) and hydrochlorofluorocarbons (HCFCs) have led to an enhanced greenhouse effect, whereby increased levels of radiation are trapped in the Earth's atmosphere.

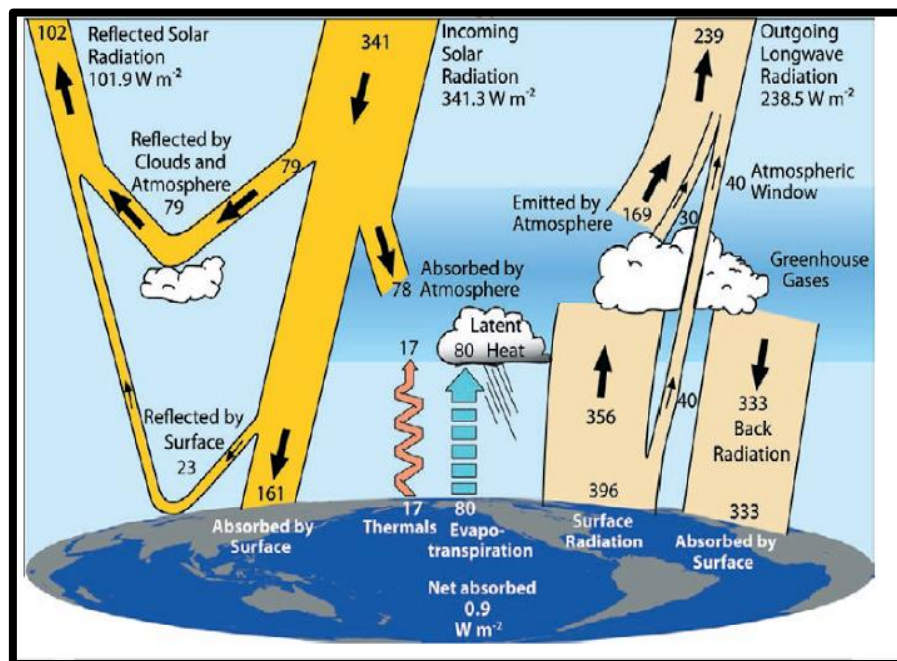


Figure 1.3. The global annual mean Earth's energy budget for the March 2000 to May 2004 period (W m⁻²). The broad arrows indicate the schematic flow of energy in proportion to their importance [7].

This is the principal cause in the increment of global average temperature, decrement in pH of the ocean surface and significant change to local weather systems: collectively known as global climate change.

One of the first significant efforts reported in order to solve this problem was carried out by the United Nations Framework Convention of Climate Change (UNFCCC) in 1997, through the signing of the "Kyoto Protocol", whose principal objective is to reduce greenhouse gas emissions. From that, carbon dioxide emissions from fossil fuel combustion are believed to be the most significant contributor to global climate change (figure 1.4).

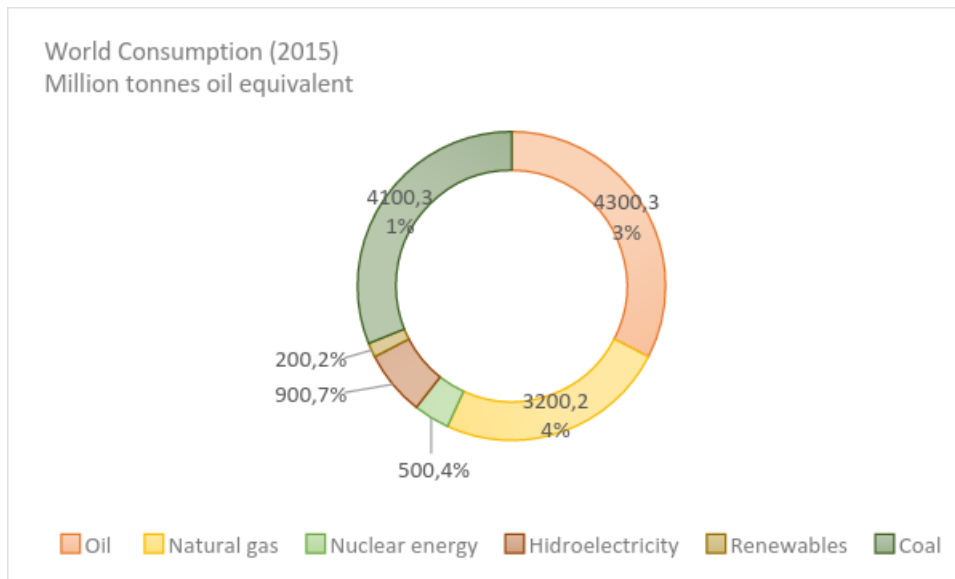


Figure 1.4. World consumption (2015) in Million tonnes oil equivalent of the energy sources [6].

As mentioned before methane is also a greenhouse gas which contributes to global warming phenomena. Despite methane does not linger as long in the atmosphere as carbon dioxide, it is initially far more devastating to the climate because of how effectively it absorbs heat. In the first two decades after its release, methane is 84 times more potent than carbon dioxide. Both types of emissions must be addressed if we want to effectively reduce the impact of climate change [8]. About 25 % of the manmade global warming we are experiencing today is caused by methane emissions.

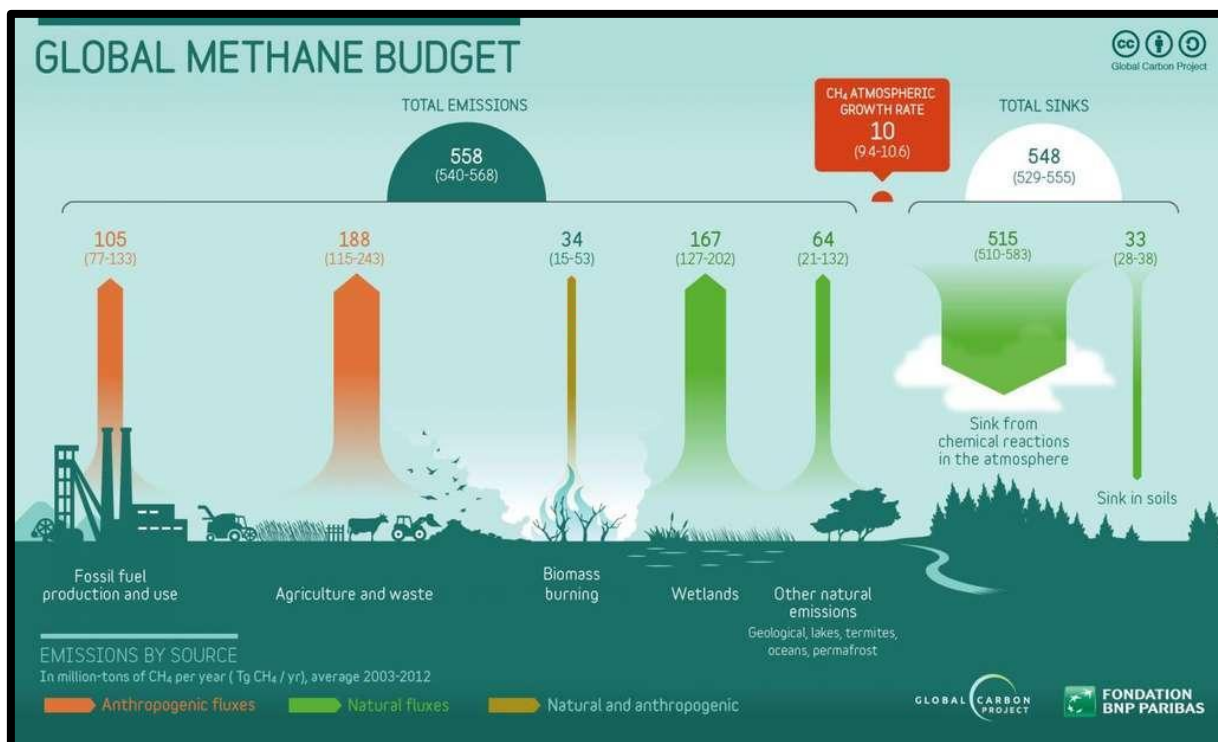


Figure 1.5. Global methane budget in millions of tons of CH₄ per year [9].

In **figure 1.5** is presented a diagram which shows the main sources of methane emissions into the atmosphere. In orange, those of anthropic origin and in green, those of natural origins. Natural emissions, fossil fuels, biomass burning, wetlands and agriculture and waste account respectively for 64, 105, 34, 167 and 188 million tons per year. Agriculture and waste are then responsible for the major part of methane emissions. Anyway, this methane can be used as a source of renewable energy thus reducing the impact of its environmental impact, the following section describes some current technologies for the processing of methane from waste and agriculture in general.

1.3.1. Biogas

Naturally the organic matter has an anaerobic decay what formed an important renewable source of methane. The methane obtained from these processes is usually called biogas. Almost all organic matter can be used as a biogas feedstock. The use of waste products could be particularly advantageous as it could prevent the unnecessary waste of useful energy sources and offer increased financial profits to plant operators. Industries that generate biogas from waste products could use it directly on-site as a fuel and/or for electricity generation [10]. Waste biomass that have potential for industrial biogas generation include:

Food waste – Waste materials from food processing industries, agricultural processes and forestries all have the potential to generate biogas through the use of anaerobic digesters. In the U.K, several plants of this type are in operation including the use of brewery by-products, potato peelings, fish waste, sugar cane waste and other food wastes from kitchens [11].

Wastewater treatment – the sludge generated by the treatment of wastewater has to be chemically treated and disposed of, in a process that represents a considerable financial cost. One encouraging alternative is the generation of the biogas from wastewater sludge in anaerobic digestion tanks. This process has been considered economically feasible [10], this kind of processes are already operated in several sites across the U.K.

Animal manure – One important source of biogas is the manure which has important uses in farming as a fertiliser, and recently also as a source for biogas generation on farm. The usual practice is to store the manure for several months until it is needed. During this time, gases that are produced from the manure can be released straight into the atmosphere, if they are not properly collected. To make use of these gases, the manure can be transferred to an anaerobic digester for biogas generation. The remaining substrate after biogas production still contains nutrients that give it value as a fertiliser [12].

Landfill gas – the organic fraction of municipal solid waste in landfill sites is biologically digested by microorganisms, releasing a stream of methane-rich gas. Currently, landfill gas is often flared to prevent a risk of explosion on mixing with oxygen. Collection of this gas and subsequent use for energetic purposes could be a viable alternative [12], [13]. Challenges associated with landfill gas collection include inconsistent gas pressure and variable gas composition resulting from differences in local ecosystems within the landfill, as a result of the heterogeneous nature of the waste.

Other methods for biogas generation include the collection of biogas from large-scale cultivation of algae [14] and the growth and subsequent anaerobic digestion of dedicated energy crops such as rape. The latter method is more controversial as it

requires the occupation of land that could otherwise be used for growing food as well as substantial energy expenditure associated with the farming of these crops [11].

Combustion of renewable methane sources can emit CO₂, but it is more favorable than fossil fuel combustion. This is possible because the carbon in biogas was originally absorbed from the atmosphere by plants during photosynthesis. After, the same amount of carbon is returned to the atmosphere during combustion of the plant-derived fuel; therefore no additional carbon is introduced into the Earth's carbon cycle. Thus maintaining null contribution to the feeding of the amounts of carbon dioxide in the atmosphere and the fuel can be considered *carbon-neutral*. This is in contrast to combustion of fossil fuels where carbon that has been removed from the carbon cycle for millions of years is reintroduced without an efficient removal mechanism.

Anyway, a renewed interest in gas-to-liquid processes has been initiated by the increasing legislation for cleaner energy sources, which includes the production of liquid fuels from biomass-derived sources. Another reason for interest in these reactions comes from the natural gas industry, where gas-to-liquid conversions, if carried out at remote offshore locations could enable some governments to profit from stranded natural gas reserves at oil wells where the natural gas by-product is otherwise flared [11]. There is little economic interest in transporting gas from remote locations due to the low volumetric energy content of natural gas compared with liquid oil [15], [16]. This because natural gas is transported from several countries after liquefaction, by cooling to -162 °C at atmospheric pressure. It is then reheated to recover the gas when it reaches the destination. However, this is an expensive solution and it does not address the need for sustainable sources of energy.

1.4. Fischer-Tropsch processes

The Fischer-Tropsch process was established in 1923 by German researchers, Franz Fischer and Hans Tropsch. They discovered that syngas CO + H₂ could be converted into a mixture of linear and branched hydrocarbons and alcohols using various metal catalysts at elevated temperatures. For commercial F-T synthesis, iron and cobalt catalysts are used at temperatures of 200 – 300 °C and pressures of 1000 – 6000 kPa. A syngas ratio of H₂/CO = 2 is generally required. Potassium and iron catalysts are

used to promote the water-gas shift reaction which is used to modify the H₂/CO ratio [11]. The main reactions are shown in **table 1.1**.

Table 1.1. Main reactions in the Fischer-Tropsch synthesis, where n, x and y are integers and M represents a metal catalyst [17]

The main reactions	
1. Alkanes	$(2n+1) H_2 + n CO \rightarrow C_n H_{2n+2} + n H_2O$
2. Alkenes	$2n H_2 + n CO \rightarrow C_n H_{2n} + n H_2O$
3. Water-gas shift	$CO + H_2O \leftrightarrow CO_2 + H_2$
Side reactions	
4. Alcohols	$2n H_2 + n CO \rightarrow C_n H_{2n+2}O + (n-1) H_2O$
5. Boudouard reaction	$2 CO \rightarrow C + CO_2$
Catalyst Modifications	
6. Catalyst oxidation	$x M + y O_2 \leftrightarrow M_x O_{2y}$
7. Catalyst reduction	$M_x O_y + y H_2 \leftrightarrow y H_2O + x M$
8. Bulk carbide formation	$y C + x M \leftrightarrow M_x C_y$

Conventional refinery processes are used to separate and upgrade the syncrude mixture into useful products such as diesel, kerosene, naphtha and waxes. High quality liquid fuels can be produced by this method with very low aromaticity and zero sulphur impurities [17]. F-T processes are a well-established set of reactions that have been improved greatly over the years with advances in catalysis and reactor design.

Parameter	Chain length	Chain branching	Olefin select.	Alcohol select.	Carbon deposition	Methane select.
Temperature	↓	↑	*	↓	↑	↑
Pressure	↑	↓	*	↑	*	↓
H ₂ /CO	↓	↑	↓	↓	↓	↑
Conversion	*	*	↓	↓	↑	↑
Space velocity	*	*	↑	↑	*	↓
Alkali content iron catalyst	↑	↓	↑	↑	↑	↓
Increase with increasing parameter: ↑						
Decrease with increasing parameter: ↓						
Complex relation: *						

Figure 1.6. Selectivity control in Fisher-Tropsch synthesis by process conditions and catalyst modifications [18].

The Fisher –Tropsch synthesis is a complex process In which a variety of variables can be operated for the purpose of increasing the selectivities of different products or conversions in the same system. **Figure 1.6** presents the general influence of the main variables of the process on the selectivities and conversions of the system, which leaves evidence of its versatility and complexity.

However, further breakthroughs are necessary if the large scale manufacture of liquid fuels from biomass sources is to become viable for “today’s energy” markets [19]. Specific challenges arises from the high cost of syngas production and preparation including sulphur removal, partial oxidation or steam reforming of methane, heat recovery and the cooling of syngas; these processes have been estimated to induce 66 % of the total costs of the production of liquid fuels from natural gas [20].

Natural gas is becoming a new promising resource to replace petroleum oil. Currently there is a large amount of information related to the use of methane for different

purposes and this continues to increase. One field of this knowledge and maybe the most challenging, is the direct conversion of methane to liquid chemicals.

Methanol is a major raw material for petrochemical production and is currently under consideration as the principal liquid fuel [21]. In the past, the methanol was produced catalytically by the reaction of hydrogen and carbon monoxide at high pressure (≈ 20 bar) and high temperature (≈ 200 °C).

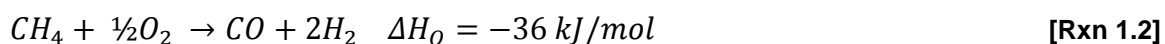
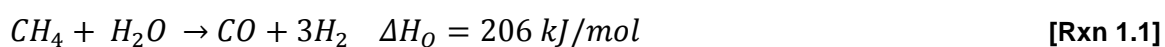
Many attempts have been made to produce methanol directly from methane [22]. Recently, some studies are still carried out in producing methanol from methane by plasma. Actually most of the research studies are focused on finding the best catalyst to improve the yields of methanol [23-25].

This combustible actually has great demand because it serves like an intermediate clean renewable source of energy of our daily life, for example: space heating, automobiles, fuel cell, and electric power generation.

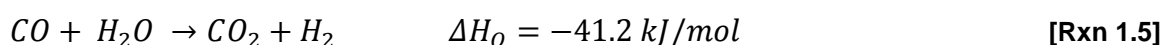
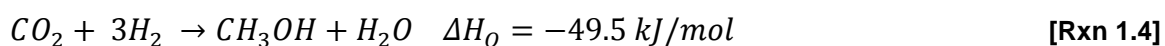
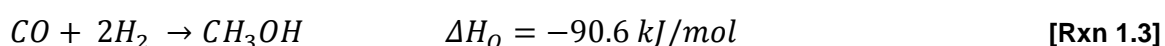
Probably the most common and developed use is the environmental friendly replacement for methyl tertiary butyl ether (MTBE) in the transportation sector used as an additive in petroleum in order to increase the oxygen content of reactants. Therefore, methanol could prove to be a major fuel for the twenty first century [26].

1.5. Industrial methanol synthesis

Actually, methanol is manufactured by a two-step method, which means that it is necessary to begin with synthesis gas (syngas which is produced from methane).



Then, methanol synthesis from syngas. This process is called indirect routes.



As the first reaction is highly endothermic, the process suffers from high cost and thermal insufficiencies. The second process is an exothermic reaction and needs copper as a catalyst. The synthesis reactor is usually operated at the condition of high temperature and high pressure to achieve high yields of methanol. On the other hand, this environment tends to shorten the lifetime of the catalyst due to sintering of the active metal on the surface of the catalyst.

Due to the fact that the commercial methanol synthesis process is energetically demanding, it may not be more economical when the natural gas could be utilized directly. Therefore, a desirable alternative could be the direct partial oxidation of methane to methanol since a one-step process could potentially reduce both capital and operational costs. Meanwhile, an increasing number of applications and manufacturing processes that require methanol in much smaller quantities or methanol mobile-plans for example fuel cell applications [27], would deliver a strong message about the importance of methanol-based process in the future. Compared to hydrogen, methanol fuel is safer and easier to handle. A comprehensive review of this comparison has been done by Olah [28]. Developing new techniques and processes of direct conversion of methane to methanol is becoming a challenging research subject. Among other methods and techniques, non-thermal plasma chemical process is one of the most promising technologies in synthesizing methanol.

1.6. Introduction to plasma

Plasma is an ionized gas, a distinct fourth state of matter. The term “ionized” means that at least one electron is not bound to an atom or molecule, converting this atoms or molecules into positively charged ions. When energy is applied to a substance, the molecules become more energetic and transform through four distinct states of matter: solid, liquid, gas and finally plasma. Generally, this increased energetic state is associated with heating, however, plasma can also be generated from a gas by the application of an electric field, energetic beam or by adiabatic gas compression [29]. Under these conditions of increased energy, the gas molecules can become dissociated or ionized. This results in a complex mixture of freely moving charged particles and neutral gas species, sufficient to make the plasma electrically conductive,

a property that distinguishes plasma from neutral gas which is an electrical insulator. Approximately equal concentrations of positive ions and electrons make the plasma quasi-neutral.

Plasma is naturally abundant throughout the universe and comprises ~ 99 % of the observable cosmos, including the solar corona, solar wind and nebula [29], [30]. Plasma is also present in the upper region of the Earth's atmosphere (at altitudes higher than 100 km) where interactions with cosmic radiation lead to the dissociation of atmospheric gas molecules. This produces a region of ions and freely moving electrons, known as the ionosphere. Plasmas can be visible on Earth as naturally occurring phenomena including lightning, the Aurora Borealis and the Aurora Australis [29].

1.6.1. Applications of plasma

The innovative studies of Siemens in the 1850s led to the first important industrial application of plasma in order to obtain ozone (O_3) from oxygen using a silent discharge, the ozone obtained was destined for water purification. Anyway, the first investigations into electrical arcs which involves several laboratory techniques have been developed for the generation of man-made plasma discharges since the early 19th century [31].

However, Langmuir named this phenomenon as a "plasma" until the 1920s [32]. In recent years, plasma technologies have progressed to include a wide range of applications across many industries. Some important applications are listed below:

Surface modification, etching of semiconductors, "plasma hardening" of metallic components for cars and aircrafts [30].

Thin film deposition, deposition of diamond and cubic boron nitride films for cutting tools [33], anti-reflective coatings for lenses, hydrophilic and hydrophobic coatings for textiles [30].

Pollutant remediation, destruction of odorous molecules and volatile organic compounds (VOCs) from diesel exhausts and flue gases [31], destruction of odorous molecules [34].

Chemical synthesis, ozone production [34] , synthesis of acetylene (C_2H_2) [31].

Lighting, excimer based UV and fluorescent lamps [31].

Plasma display panels, large area flat-screen televisions [35].

Lasers, CO₂ laser discharges for cutting and welding [35].

Biomedical techniques, blood coagulation, desactivation of micro-organism, tissue engineering, sterilisation of instruments and surfaces [29].

Several of these plasma technologies are relatively developed. However, the empirical approach has focused on the production of deliverables, which leads to limited knowledge and understanding of plasma chemistry [30].

1.6.2. Types of plasma

All plasmas consist of multiple components including electrons, excited molecules and atoms, ions, radicals, neutral gas species and photons. There are two main types of plasmas: high-temperature plasma (such as thermonuclear fusion plasmas or thermal arc torches) and low-temperature plasma. The extent to which these constituents have reached thermal equilibrium is used to further classify the plasma as thermal or non-thermal (which are also known as equilibrium and non-equilibrium plasmas respectively). These classifications are shown in **Table 1.2**.

Table 1.2. Subdivision of plasmas by temperature, where T_0 = gas temperature, T_i = ion temperature, T_r = rotational temperature, T_v = vibrational temperature and T_e = electron temperature (Hippler et al., 2001).

Low-Temperature Plasma		High Temperature Plasma
Non-Thermal Plasma		Thermal Plasma
$T_0 \approx T_i \approx T_r < T_v \ll T_e$ $\leq 10^5$ K	$T_0 \approx T_i \approx T_r \approx T_v \approx$ $T_e \leq 2 \times 10^4$ K	$T_0 \approx T_i \approx T_r \approx T_v \approx T_e \geq$ 10^7 K

In thermal plasma, sufficient applied energy and time for equilibration has resulted in a plasma discharge that can be defined by a single temperature. In the other hand, non-thermal plasmas are characterised by multiple temperatures relating to different plasma species. Electrons with high energetic values ($10^3 - 10^5$ K) can exist together with species of so much lower temperatures such as excited species, ions and

neutral molecules. Heavy gas molecules usually exhibit the lowest temperatures in these systems and in many cases the bulk gas remains close to room temperature [29].

1.6.3. Generation of non-thermal plasma by electric fields

The most used method for the formation of non-thermal plasma is by the application of an external electric field between two electrodes surrounded by a volume of gas. The plasma can be operated either at low pressures (10^{-3} Pa) or at atmospheric pressure and above.

The breakdown voltage (V_b) defines the minimum voltage required to breakdown a gas (or mixture of gases) to form a plasma discharge. V_b is dependent on the gas pressure (p) and the distance between the electrodes (d). This relationship is described by Law of Paschen, where a and b are constants that are dependent on the gas type [36].

$$V_b = \frac{a p d}{\ln(p d) + b} e \quad \text{Eq. 1.1}$$

An applied voltage causes free electrons that exist to some extent in a gas volume as a result of an interaction with cosmic radiation, to become accelerated. At the point where the breakdown voltage is reached, the current flow will increase sharply due to an intensive avalanche of electrons in the discharge gap between the electrodes. These high energy electrons will collide with gas molecules leading to the formation of new “active” plasma species including excited molecules and atoms and their relevant degrees of freedom, radicals, ions and new stable gas molecules. These collision processes are shown in **Table 1.3**.

Table 1.3. The main plasma processes. A and B represent atoms and M stands for a temporary collision partner [31].

Electron/Molecular Reactions	
Excitation	$e^- + A_2 \rightarrow A_2^* + e^-$
Dissociation	$e^- + A_2 \rightarrow 2 A + e^-$
Attachment	$e^- + A_2 \rightarrow A_2^-$
Dissociative attachment	$e^- + A_2 \rightarrow A^- + A$
Ionisation	$e^- + A_2 \rightarrow A_2^+ + 2 e^-$
Dissociative ionisation	$e^- + A_2 \rightarrow A^+ + A + e^-$
Recombination	$e^- + A_2^+ \rightarrow A_2$
Detachment	$e^- + A_2^- \rightarrow A_2 + 2 e^-$
Atomic/Molecular Reactions	
Penning dissociation	$M + A_2 \rightarrow 2 A + M$
Penning ionisation	$M^* + A_2 \rightarrow A_2^+ + M + e^-$
Charge transfer	$A_{\pm} + B \rightarrow B_{\pm} + A$
Ion recombination	$A^- + B^+ \rightarrow AB$
Neutral recombination	$A + B + M \rightarrow AB + M$
Decomposition	
Electronic	$e^- + AB \rightarrow A + B + e^-$
Atomic	$A^* + B_2 \rightarrow AB + B$
Synthesis	
Electronic	$e^- + A \rightarrow A^* + e^-$, $A^* + B \rightarrow AB$
Atomic	$A + B \rightarrow AB$

During collisions between electrons and heavy gas molecules only a small portion of the energy is transferred, due to the relative sizes of the species involved. In most non-thermal plasma systems applied for gas processing, the pressure is the atmospheric one and the plasma is only weakly ionised. The degree of ionisation in the plasma can be defined as the ratio of the density of charged particles to the density of neutral species [29].

In addition to the plasma species shown in **table 1.3**, photons are also generated in the plasma volume. In an electronically excited gas molecule or atom, an electron

exists in a high energy orbital further from the nucleus, whilst an electron “hole” exists in the lower energy orbital that it was originally excited from. This excited state is metastable and can spontaneously return to its more stable ground state. When an electron is excited back to its lower energy orbital, the excess of energy is released in the form of a photon. This initiates a chain of reactive photon absorptions and emissions as molecules are excited and de-excited within the plasma. Consequently, the plasma can exhibit a visible glow if the energies of the emitted photons are in the visible region of the electromagnetic spectrum.

In plasma processing of gases, each of the plasma species may have different roles in the plasma chemistry. Electrons, being the first to receive energy from the electric field, distribute this energy through collisions, generating new reactive species. Vibrationally excited molecular states can transfer a significant proportion of energy into gas heating, which will accelerate chemical reactions in the plasma. Ions and radicals are able to make a significant contribution in plasma chemical synthesis due to their ability to react in plasma at lower temperatures than would be required by thermal reaction methods. Control over the complex chemical processes in a plasma by selection of appropriate gases, plasma type and operating conditions could allow the selective synthesis of the desired end products[29].

1.6.4. Townsend mechanism of electric breakdown

Consider breakdown in a plane gap d by DC voltage V corresponding to electric field

$$E = \frac{V}{d} \quad \text{Eq. 1.2}$$

Occasional primary electrons near a cathode provide low initial current i_0 . The primary electrons drift the anode, ionizing the gas and generating avalanches. The ionization production of electrons per unit length along the electric field: $dn_c/dx = \alpha n_e$, $n_e(x) = n_{e0} \exp(\alpha x)$. The Townsend ionization coefficient is related to the ionization rate coefficient $k_i(E/n_0)$ and electron drift velocity v_d as

$$\alpha = \frac{v_i}{v_d} = \frac{1}{v_d} k_i \left(\frac{E}{n_0} \right) n_0 = \frac{1}{\mu_e} \frac{k_i \left(\frac{E}{n_0} \right)}{E/n_0} \quad \text{Eq. 1.3}$$

Where v_i is the ionization frequency and μ_e is electron mobility, which is inversely proportional to pressure. The Townsend coefficient α is usually presented as similarity

parameter α/p depending on the reduced electric field E/p . Dependences $\alpha/p = f(E/p)$ for different gases can be found in Fridman and Kennedy [36].

Each primary electron generated near a cathode produces $\exp(\alpha d) - 1$ positive ions moving back to the cathode. The ions lead to extraction of y^* $[\exp(\alpha d) - 1]$ electrons from the cathode due to secondary electron emission characterized by the Townsend coefficient y . Typical y - values in discharges are 0.01-0.1. Taking into account the current of primary electrons i_0 and electron current due to the secondary electron emission from the cathode, the total electronic part of the cathode current i_{cath} is

$$i_{cath} = i_0 + yi_{cath}[\exp(\alpha d) - 1] \quad \text{Eq. 1.4}$$

Total current in the external circuit is equal to the electronic current at the anode, where the ion current is absent. The total current can be found as $i = i_{cath} \exp(\alpha d)$, which leads to the Townsend formula:

$$i = \frac{i_0 \exp(\alpha d)}{1 - y[\exp(\alpha d) - 1]} \quad \text{Eq. 1.5}$$

The current in the gap is non-self-sustained as long as the denominator in Eq.1.5 is positive. When the electric field and Townsend coefficient α become high enough, the denominator in Eq. 1.5 goes to zero and transition to self-sustained current takes place, which is called the Townsend breakdown mechanism:

$$y[\exp(\alpha d) - 1] = 1, \alpha d = \ln\left(\frac{1}{y} + 1\right) \quad \text{Eq. 1.6}$$

The similarity parameters α/p and E/p are related semi-empirically according to (Eq.1.3) as

$$\frac{\alpha}{p} = A \exp\left(\frac{B}{E/p}\right) \quad \text{Eq. 1.7}$$

Where parameters A and B are constants which depend of gas nature usually founded at $E/p = 30-500$ (V/cm*Torr) range.

Combination of relations (Eq.1.6) and (Eq.1.7) gives formulas for calculating the breakdown voltage and breakdown reduced electric field as functions of an important similarity parameter pd :

$$V = \frac{B(pd)}{C + \ln(pd)}, \frac{E}{P} = \frac{B}{C + \ln(pd)} \quad \text{Eq. 1.8}$$

Here $C = \ln(A) - \ln(\ln(1/y) + 1)$ is almost constant. The breakdown voltage

dependence on the similarity parameter pd is usually referred to as the Paschen curve. These curves have a minimum corresponding to easier breakdown conditions, which can be found from (Eq.1.8):

$$V_{min} = \frac{2.72 \cdot B}{A} \ln \left(1 + \frac{1}{y} \right), \left(\frac{E}{p} \right)_{min} = B, (pd)_{min} = \frac{2.72}{A} \ln \left(1 + \frac{1}{y} \right) \quad \text{Eq. 1.9}$$

Reduced electric field E/p required for breakdown (Eq.1.8) decreases only logarithmically with pd . Breakdown of larger gaps is less sensitive to the secondary electron emission and cathode material, which explains the E/p reduction with pd . This reduction of breakdown electric field in electronegative gases is limited by electron attachment processes, characterized by Townsend coefficient β :

$$\beta = \frac{v_a}{v_b} = \frac{1}{v_d} k_a \left(\frac{E}{n_0} \right) n_0 = \frac{1}{\mu_e} \frac{k_a(E/n_0)}{E/n_0} \quad \text{Eq. 1.10}$$

In this relation $k_a(E/n_0)$ and v_a are the attachment rate coefficient and frequency with respect to an electron. The Townsend coefficient β characterizes electron losses due to attachment per unit length:

$$\frac{dn_c}{dx} = (\alpha - \beta)n_c, n_c(x) = n_{e0} \exp[(\alpha - \beta)x] \quad \text{Eq. 1.11}$$

The Townsend coefficient β , similarly to α , is an exponential function of the reduced electric field although not as strong. Therefore, the ionization rate much exceeds attachment at high electric fields, and the coefficient β can be neglected with respect to α in this case. When the gaps are relatively large (≥ 1 cm at 1 atm), the Townsend breakdown electric fields in electronegative gases become almost constant and limited by attachment processes.

Several different types of non-thermal plasma can be formed depending on the type of applied electric field used to drive the plasma formation. This may be a continuous or pulsed direct current (DC) or an alternating current (AC) which may utilise radio frequencies (kHz – MHz) or microwave frequencies (GHz).

1.6.5. Continuous and pulsed direct current discharges

Several types of direct current (DC) discharge can be obtained depending on the voltage-current characteristics as depicted in **figure 1.7**. The initial breakdown of a gas at low current is known as a Townsend discharge. The transition from Townsend discharge to corona, through to subnormal glow discharge and normal glow discharge

is accompanied by an increase in current and simultaneous decrease in the applied voltage. A normal glow discharge can be characterised by a constant current density at the cathode surface, which is only partially covered by the discharge. As the current is increased with increasing voltage, an abnormal glow discharge develops which completely covers the cathode surface. At even higher currents, an irreversible glow-to-arc transition can occur. The arc is sustainable at low voltage and high current due to heating of the cathode to the point of thermionic emission (heat-induced current flow) [37].

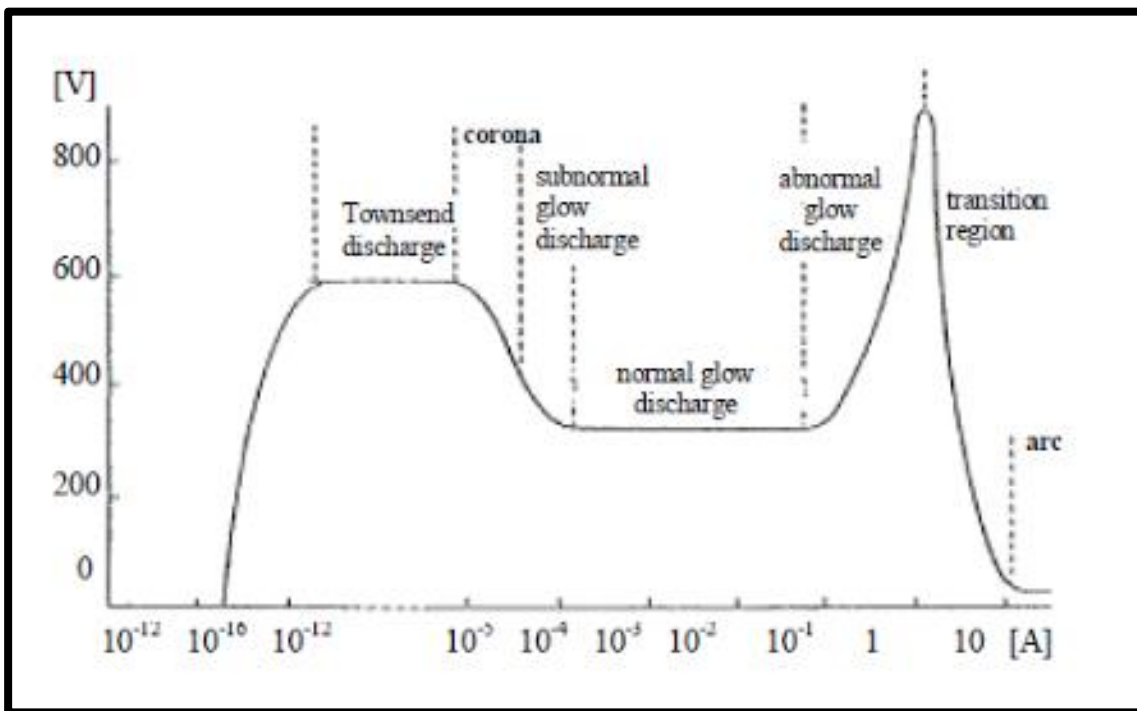


Figure 1.7. The dependence of voltage upon current for various kinds of DC discharges [38].

The most used DC discharges in plasma processing of gases are the corona discharge and the gliding arc discharge, typical reactor configurations for these are described in the following sections [11].

1.6.5.1. Corona discharges

A corona is a weakly luminous discharge, which appears at atmospheric pressure near

sharp points, edges, or thin wires where the electric field is sufficiently large, the corona discharge are always non uniform: a strong electric field, ionization and luminosity are located in the vicinity of one electrode. Charged particles are dragged by the weak electric fields from one electrode to another to close the electric circuit (the electric field at one or both electrodes is stronger than in the surrounding gas) [29]. A corona discharge can be formed by applying either continuous or pulsed DC voltage between two electrodes. The electrodes are most commonly arranged as a grounded cylindrical outer electrode (stainless steel tube) with a high voltage wire or rod inner electrode (**Figure 1.8**) or as a point-to-plate (**Figure 1.9**) or point-to-point electrode configuration. The area between the electrodes where the corona is formed is occupied by a continuous flow of gas.

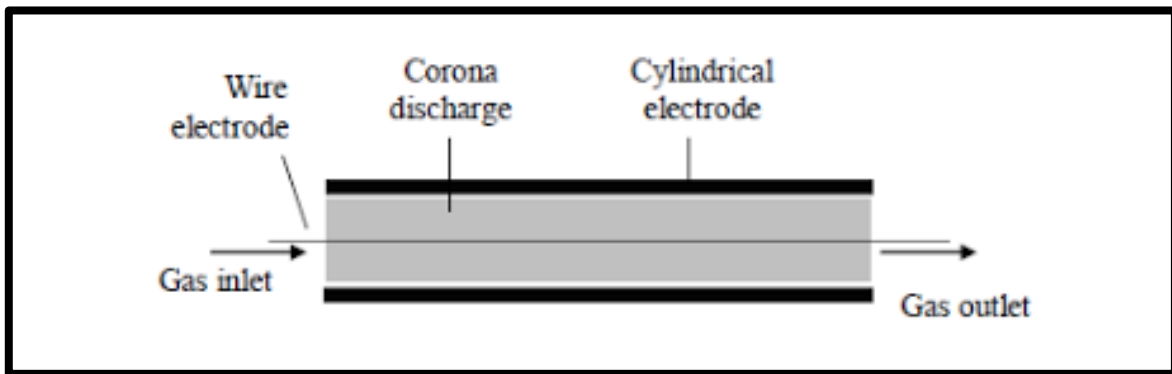


Figure 1.8. Schematic diagram of a corona discharge reactor in a coaxial wire-cylinder configuration [11].

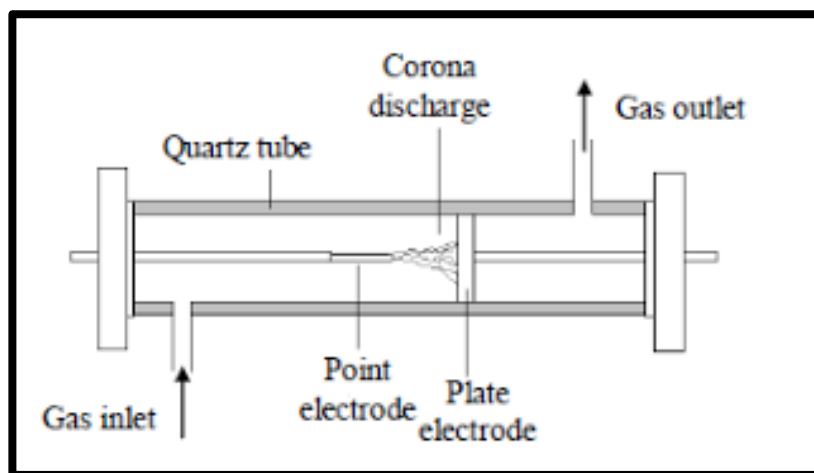


Figure 1.9. Schematic diagram of a corona discharge reactor in a point-to-plate configuration [11].

Corona discharges can take on several forms depending on the relative polarity of the

electrodes. The polarity electrode where the high electric field is located distinguish between negative corona (around the cathode) and positive corona (around the anode) [29]. For a point-to-plate electrode configuration, the different types of corona discharge are shown in **Figure 1.10**, where the applied voltage increases from left to right. Positive corona is formed at a pointed anode, whilst negative corona is formed at a pointed cathode. In a positive corona, the initial breakdown of the gas produces a burst pulse, which is limited to the area immediately surrounding the electrode. The discharge is space-charge limited and therefore requires an increase in voltage to create additional charged species, leading to the formation of streamers. Streamers extend into the inter-electrode gap and several transient streamers can be observed at a given time. In this mode, the corona occupies a relatively large active volume and has a low temperature of $\sim 27\text{ }^{\circ}\text{C}$ [39].

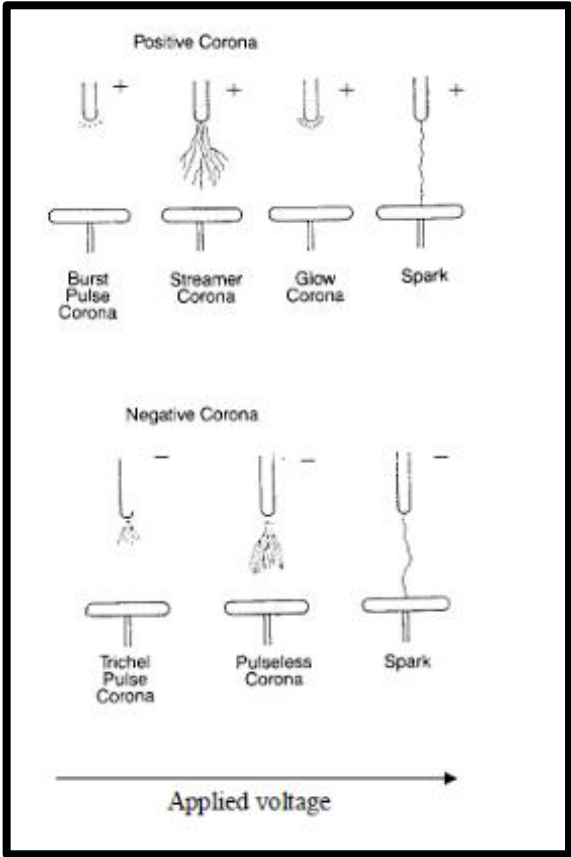


Figure 1.10. Schematic diagrams showing different forms of corona discharges in a point-to-plate electrode configuration [11].

In both positive and negative corona, high current flow will result in complete breakdown and the formation of a single spark discharge that bridges the discharge

gap. A spark discharge is confined to a narrow channel and produces an unsteady current. The spark is usually noisy and causes local heating in the channel in which it is formed and is therefore not a desirable outcome. The use of short DC pulses, typically of nanosecond duration can overcome the problem of unwanted spark formation. By varying between plasma pulses and plasma afterglow, the current flow can be controlled. This can improve the energy efficiency of the process and allow operation at higher powers [37].

1.6.5.2. Gliding arc discharges

A gliding arc is an auto-oscillating discharge between at least two diverging electrodes submerged in gas flow. Self-initiated in the upstream narrowest gap, the discharge forms the plasma column connecting the electrodes. This column is dragged by the gas flow toward the diverging downstream section. The arc grows with the increase interelectrode distance until it extinguishes, but it reignites itself at the minimum distance between the electrodes to start a new cycle as shown in **Figure 1.11** [29].

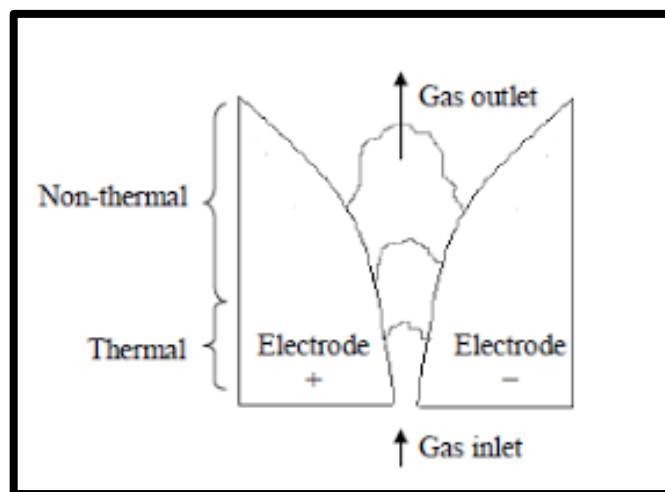


Figure 1.11. Schematic diagram of a gliding arc discharge reactor [11].

Gliding arcs may be thermal or non-thermal, depending on the applied power and gas flow rate. It is also possible to operate in the transitional regime, whereby the discharge has thermal characteristics in the lower part of the gliding-arc and evolves into a non-thermal discharge as it proceeds up the electrodes [29]. Gliding arc discharges are suitable for applications that require relatively large gas flows (several L min^{-1}) and can be either DC or AC driven.

1.6.5.3. Dielectric barrier discharges (DBD)

The corona to spark transition is prevented in a pulsed corona by employing nanosecond pulse power supplies. Another approach which avoids spark formation in streamer channels is based on the use of a dielectric barrier in the discharge gap that stop current and prevent spark formation. Such a discharge is called the DBD. The presence of a dielectric barrier precludes DC operation of DBD, which usually operates at frequencies of 0.05-500 kHz. Sometimes DBDs are called the silent discharges due to the absence of the spark, which are accompanied by local overheating and the generation of local shock waves and noise.

The dielectric barrier discharge (DBD) or silent discharge (as it was originally known) is a strongly non-thermal plasma that can be operated at atmospheric pressure. DBDs are able to form stable discharges in a range of different gases at relatively high discharge powers, making them particularly suitable for many industrial applications. The DBD reactor consists of two electrodes with one or more dielectric barriers positioned in the discharge gap (in the path of current flow). Materials with high relative permittivity such as quartz, glass and ceramics are suitable for use as dielectric barriers. Several DBD configurations are possible including planar, cylindrical and surface discharges, as illustrated in **Figure 1.12**. The spacing in the discharge gap can vary from hundreds of micrometers to several centimeters.

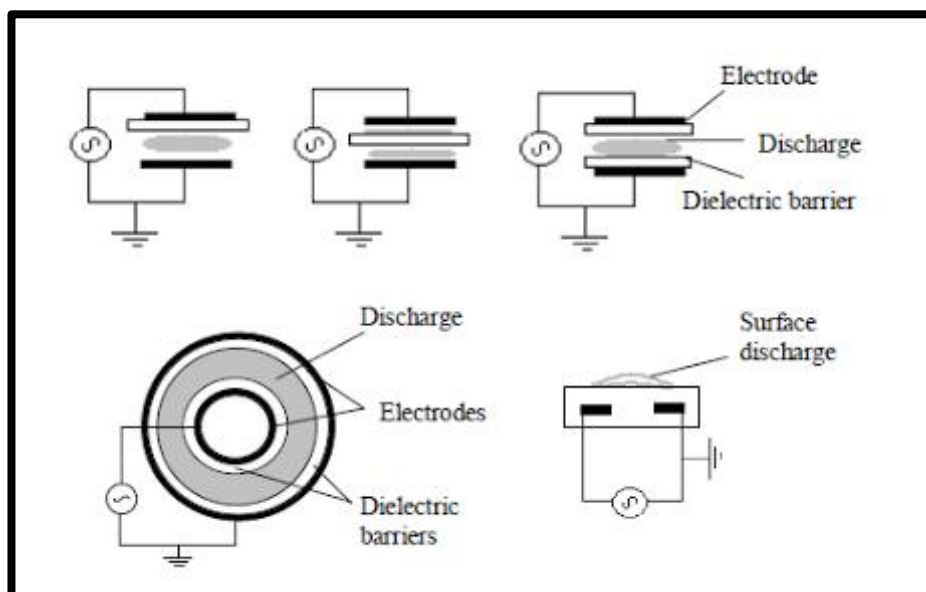


Figure 1.12. Schematic diagrams of planar, coaxial and surface DBD configurations [34].

1.6.5.3.1. **Microdischarges**

The term microdischarge is not clearly defined; sometimes it just indicates the generation of plasma smaller than 1 mm. According to such a definition, even DBD can be considered a microdischarge; the DBD gaps are often smaller than 1 mm, and the DBD filaments have a typical diameter of 0.1 mm [29].

The DBD is a non-uniform plasma discharge, it consists of many tiny breakdown channels known as microdischarges or filaments that cover the entire surface of the dielectric material and extend across the discharge gap. The dielectric barrier limits the flow of current causing the microdischarges to become extinguished, leaving significant charge deposition on the dielectric surfaces. As the polarity of the electrodes is rapidly changing, the microdischarges are reformed at the point where the breakdown voltage is reached in the next half cycle of the AC voltage sine wave. This results in the continuous formation of nanosecond microdischarges at a frequency which is twice that of the applied frequency [34]. The microdischarges appear as “spikes” on the current waveform. In appearance, the microdischarges are randomly distributed over the surface of the dielectric. In reality, the position of the microdischarge formation is dependent on the residual charge distribution on the dielectric surface [40], [41].

Where DBD plasmas are concerned, exclusive use of the term “dielectric constant” is used, but the terms “relative permittivity” and “dielectric constant” are synonymous, meaning the ability of a material to store electrical charge relative to a vacuum.

1.6.5.3.2. **Memory effect in DBD plasma**

The formation of the filaments is a complex process. Avalanches are first initiated, followed by cathode-oriented streamers bridging the gap. They form conducting channels of weakly ionized plasma until the local electric field is collapsed caused by the charges accumulated on the dielectric surface and ionic space charge. After electron current termination, there is still a high level of electronic excitation in the channel volume, along with charges deposited on the surface and ionic charges in the volume, allowing this region to be separated from the rest of the volume.

The fact that the remnant is not fully dissipated before the formation of the next microdischarge is called memory effect, which will facilitate the formation of a new filament in the same location. It is possible that with the increase in the flow rate value these remnant can displace through the channel and facilitate the appearance of discharge [42], [43].

1.7. Plasma chemistry for methanol production

There is currently promising research on the partial oxidation of methane in a non-thermal discharge, especially on DBD plasma. These experiments indicate that this kind of systems are able to create a highly reactive environment at low temperatures and therewith opens up an alternative, highly flexible and environmentally friendly processing route.

However, atmospheric pressure plasmas have a tendency to become unstable due to rapid transition to arcs. Confinement of high pressure plasma to dimensions below about one millimeter is useful to avoid instability problems and maintain a self-sustaining discharge. Such a plasma is often referred to as microplasma. In this respect, utilization of microplasma in microreaction technology can bring unconventional thermochemical conditions to materials processing, enabling better control over process parameters to selective synthesis of desirable products [44].

1.7.1. Plasma reactor designs for partial oxidation of methane (POM)

Various designs of plasma reactor for methane and oxygen conversion to methanol have been proposed shown in **Figure 1.13**. The typical tubular discharge reactor consists of two concentric cylinders. The outer cylinder functions as ground electrode and the inner cylinder usually made from glass or quartz tube, serves as the dielectric. A steel or copper metal rod is located inside the inner cylinder and performs as another electrode. When plasma is turned on, the micro-discharges appear on the surface of the inside electrode.

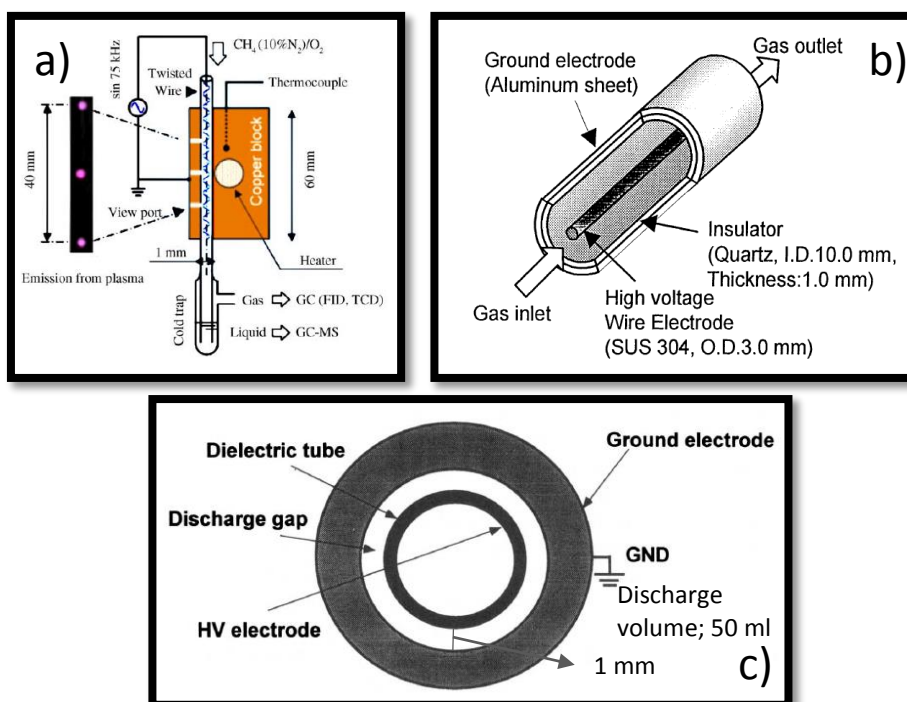


Figure 1.13. Schematic diagram of the plasma DBD reactor a) [45], b) [46] c) [47]

The DBD plasma ability to reduce the required temperature and pressure needed for reactions to occur as well as its ability to control the products selectivity could be considered as a catalytic effect following the idea of Larkin et al. [48].

The partial oxidation of methane to methanol with oxygen or air was also investigated experimentally and theoretically by Zhou et., al. [47].

The reactor presented in **figure 1.13c**, consists in an annular discharge gap of 1 mm width formed by an outer steel cylinder of 54 mm inner diameter and an inserted cylindrical quartz tube of 52 mm outer diameter and 2.5 mm wall thickness. The length of the discharge gap is 310 mm, giving a discharge volume of about 50 ml. The outer steel cylinder serves as the ground electrode and an alternating sinusoidal high voltage of up to 20 kVpp amplitude and about 30 kHz frequency is applied to the HV electrode, a metal foil mounted inside of the quartz tube [47]. It is reported that the partial oxidation of methane in two different types of reaction mixtures: the first one consists in methane and oxygen and the second one in methane and air. The highest value of methanol yield of 3% was achieved in CH_4/O_2 (8/2) mixture. In CH_4/O_2 (7/3) mixtures 2% was obtained.

Another interesting reactor design was also proposed by Nozaki et al. (2004) [45], called micro-plasma reactor, shown in **figure 1.13a**. In their studies, the DBD reactor was used to synthesize methanol from methane and oxygen. It consists of a Pyrex thin glass tube with an internal diameter of 1.0 mm and a length equal to 60 mm, a twisted metallic wire inside the tube serves as electrode. The reactor is secured in a heat reservoir to maintain a constant reaction temperature. A high-voltage sine wave is applied between the twisted metallic wire and the grounded heat reservoir. The principle of generating plasma was similar to the DBD which was characterized by a variety of filamentary micro discharges. In this experiment, methanol was the major product, whose selectivity reached 34% at 30% of methane conversion. However, methanol, oxidized partially from methane, could further react to form other oxygenates such as formic acid and formaldehyde.

Another type of DBD reactor was proposed independently by Aghamir et al. (2004) and Okumoto et al. (1997) [49,50]. The general scheme of the reactor is presented in **Figure 1.13b**. The discharge reactor consisted of a 10 mm as an inner diameter quartz tube, which was also used as dielectric barrier. A stainless steel rod and a 15 cm long aluminum foil, formed respectively the anode and cathode of the discharge. The aluminum foil was tightly wrapped around the quartz tube, which had outer diameter of 12 mm. The stainless steel electrode was placed on the symmetric axis inside the tube. Two gas inlets located at the top and the bottom of the reactor were provided as an inlet of the reactants and an outlet of products [46]. C₂ hydrocarbons and methanol were mainly produced and the selectivity of methanol reached 30% with high voltage pulses of approximately 10⁻¹⁰ s of rise time, +25 kV of peak voltage, 440 Hz of pulse frequency and argon concentration of 30 % (v/v).

1.7.2. CH₄/O₂ ratio

O₂-rich condition could lead to an over-oxidation of methane where the main product will be CO₂ in detriment of methanol [52]. In the other hand, when the concentration of O₂ in the feed is low, the lack of oxygen will inhibit the synthesis of methanol and methyl coupling will be the major pathway [26].

Aghamir et al. (2004) reported that the presence of oxygen in gas mixture lead to the production of methanol and that with the increasing of the ratio O₂/CH₄, the selectivity of methanol first increased rapidly and then decreased. In **table 1.4** they reported a maximum of methanol selectivity equal to 70 % at 0.05 O₂/CH₄ ratio [50]. Another important result reported by Nozaki et al. (2004) report until 37 % of methanol selectivity at 0.5 O₂/CH₄ ratio [45], the results at 0.1 and 1 of O₂/CH₄ reported methanol selectivities of 6.25 and 0 respectively. Meanwhile Okumoto et al. (2001) reported a maximum in methanol selectivity of 32% with a 0.17 O₂/CH₄ ratio [52] and Indarto et al. reported an optimum ratio of oxygen to methane equal to 0.25. Which resulted in a methanol selectivity of 26 % [53].

Table 1.4. Comparison methanol selectivity and methane conversion by different authors

Authors	Aghamir et al. (2004) [50]	Nozaki et al. (2004) [45]	Okumoto et al. (2001) [52]	Indarto et al. (2006) [53]
O ₂ /CH ₄ ratio	0.05	0.5	0.17	0.25
CH ₄ conversion (%)	-----	45	7	20
Methanol selectivity (%)	70	37	32	26
Inert gas (%)	He (composition not specified)	Not used	Ar (0-90)	Not used
SIEM (kJ/mol _{methanein})	-----	400-110	21.1	3125-5000
Residence time (s)	7.2	0.094-0.18	1-4	17.6
Type of electrical signal	-----	Sine wave	Pulse	Sine wave

It is difficult to compare these different optimums because the methanol selectivity is also affected by other variables and all these studies were carried out in various conditions in terms of residence time, percentage of noble gas or nature of the high voltage applied. For example Larkin et al. (2001) pointed that at long residence time, the produced methanol will be consumed to form organic acids and formaldehyde [48].

Also the way the power is supplied can affect the formation of respective amounts of O° , CH_3° and CH_4^* because the energy distribution of electrons will be affected. The amount of methane activated was mainly influenced by the discharge characteristics, but the rates of oxidation of $\bullet CH_3$, $\bullet CH_2$, and $\bullet CH$ to CO and CO_2 were dependent on oxygen concentrations [53].

1.7.3. Noble gas effect

In many researches of methanol synthesis from partial oxidation of methane by plasma, noble gas like helium, neon, argon, was added to feed gas to help the performance of the process. These gases (noble gas) act not only as an inert dilution gas but can also play an important role on the reactions.

The introduction into the stream to be processed of a noble gas is not only responsible of the decreasing the partial pressure of reactants, but also it can change the density of the discharge active species generated in the plasma-zone. The breakdown potential of inert gas, such as helium and argon, is lower than that of methane or oxygen at the same condition. It means that the plasma can be initiated at lower supplied voltage [26]. Another consequence is that the population of energetic free electrons might increase at higher concentrations of noble gas, thus leading to an increment of the conversion of methane.

The details of the effect of the inert gas on the partial oxidation of methane are much less discussed in the literature than the variables previously presented. Anyway, one of the first report about this effect is presented by Okumoto et al. [49]. They mentioned that the increment of the dilution ratio of noble gas resulted in the decrease of the O_2 partial pressure and methanol selectivity could reach the maximum point. The maximum of methanol selectivity was reported at $O_2/CH_4=15/85$ and 50 (% v/v) of argon concentration based on the total flow of CH_4 and O_2 . On the other hand the ethane production increased linearly. They also found that when the O_2 partial pressure was kept constant, the methanol synthesis increased when the noble gas concentrations increased and the ethane production was constant. Another interesting reported conclusion was the number of electrons produced in a full pulse wave was increased at higher dilution ratios [49].

1.8. Conclusion

The topics of conversion and utilization of methane are important issues to tackle global warming. Controlled partial oxidation of methane to methanol through the catalytic reactions has been studied for a very long time as an alternative to methane disposal in the environment. Unfortunately, there is still no process that produces reasonable methanol yield, but there has been encouraging progress.

The aim of this chapter was to present the generalities about partial oxidation of methane (POM) to produce methanol as a liquid fuel and in particular shows the advantages and opportunities that plasma processes have for the application in POM to the production of methanol.

The literature presents several production processes for the conversion of methane to methanol by plasma. However, there are still many problems needed to be solved which means a large space for further researches. An innovated and promising way in plasma chemical process of methanol synthesis is the use of non-thermal plasma (dielectric barrier discharge) in milli-reactors. This is due to the fact that with the miniaturization the stability of the microdischarges is increased and the process control is improved. Many works have been done and some are still in progress. The combination of miniaturization technology and plasma chemistry can give rise to controllable sustainable chemical processes which can be industrialized by numbering up millireactors.

In the following sections it is presented an experimental study and discussion of a partial oxidation of methane in a DBD plasma Millireactor. The design and conception of the reactor are presented in Chapter 2.

Chapter 2 : Analytical techniques

2.1. Plasma power measurements

Measuring the energy injected is usually done through Lissajous cycles. This method collects all loads passing through the gas measurement capacitors added in the circuit for this purpose. It is therefore an integral method that will not give enough information for the individually filaments. Nevertheless it is essential here to test the effect of gas composition as well as many geometric and reaction parameters of the system. The DBD can be modeled by just two capacities in series: the gas capacity (C_g) and the dielectric capacity (C_{di}). They are in fact two insulating medium in which a voltage is applied in **figure 2.1** is showed the basic method schema. A third measure of capacity (C_M) is added in series to this method. This capacity should be selected substantially larger than the equivalent capacitance of the DBD to avoid excessively disturbing the voltage applied across the reactor[54]. In the experiment the determined capacitor was 2.5 nF. The real circuits may comprise other parasitic capacitances. It is possible however that a parasitic capacitance appears in parallel with the reactor. This is the case for example of the capacity formed by the inner electrode disposed horizontally at about 2 mm from the ground plane. To take in to account possible disturbances measures by this phenomena, the scheme includes in a parallel respect to C_{di} and C_g , a parasitic capacitance C_{pa} . In practice, the tension that can be measured are the voltage applied across the whole circuit (U_A), and the terminal voltage near of C_M , denoted U_M . One current passive high voltage probe (PMK-PHV attenuation 1000:1) was used for the measurement of the electric current in the ground signal.

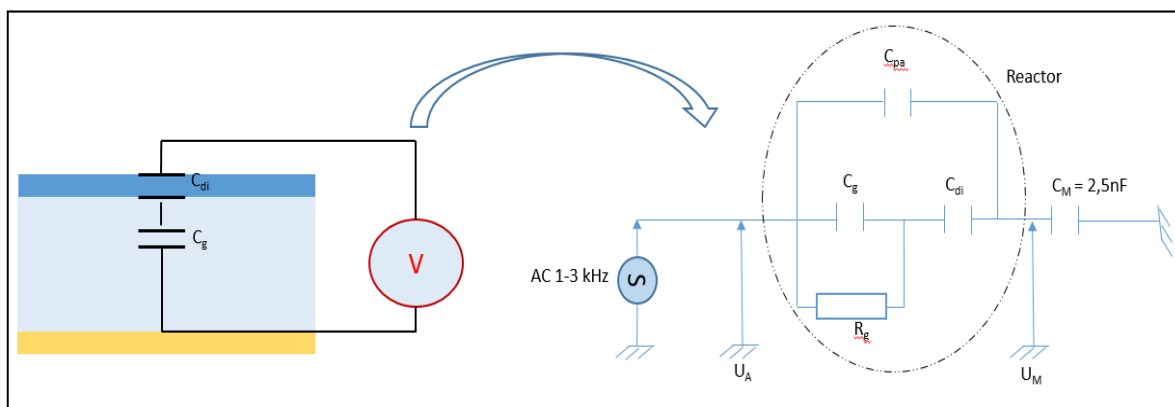


Figure 2.1. Electric scheme electric utilized for the measurements of energy from Lissajous curve

2.2. Intensified charge coupled device (ICCD)

To determine the uniformity of the discharge, pictures have been taken by use of a commercial intensified charge couple device. In ICCD cameras, ultra-low-light detection is achieved by high amplification of incoming photons by an intensifier. Time resolution is possible due to the fact that the intensifier can be switched on and off (gated) in very short intervals (**figure 2.2**).

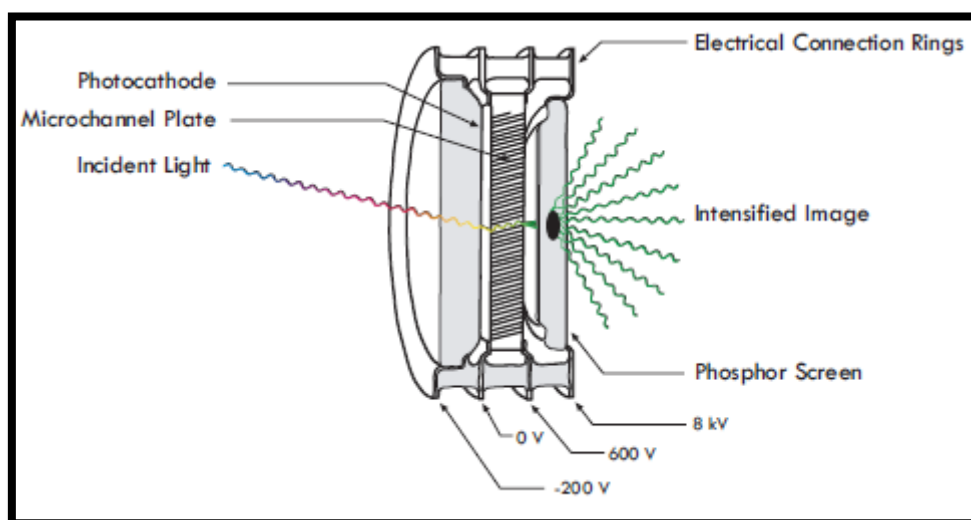


Figure 2.2. Cross-section view of an image intensifier tube utilizes in a Princeton instrument ICCD camera [55]

The intensifier consists of a photocathode, a microchannel plate (MCP), and a phosphor screen. A fraction (the quantum efficiency, or QE) of the photons incident on the photocathode is converted into clouds of electrons by MCP, which acts as a distributed electron multiplier. The electrons released from the MCP then strike the fluorescent screen (phosphor) and cause it to emit far more photons than were incident on photocathode[55].

The analysis of images is based on a PI-MAX 4 ICCD camera with high quantum efficiency manufactured by Princeton Instruments. The ICCD camera comprises a Kodak KAI-1003 CCD array of 1024 x 1024 pixels. A gating < 500 pico-second gating delivers high temporal resolution for effective background discrimination.

In all ICCD experiments the gating of the camera was set equal to the time of a half period of frequency with an accumulation of 20 photos and a gate delay 0.31 μ s.

2.3. Gas chromatography

In this thesis gas chromatography (GC) has used for the analysis of gas mixtures during the experiments. In general, chromatography refers to the separation of mixtures into pure substances and can be used for both gases and liquids (little quantities). Essentially, chromatography requires a “mobile phase” (containing the mixture to be separated) and a “stationary phase” through which the mobile phase can be eluted.

GC columns originally consisted of a little tube containing a packing of solid support material in GC, the mobile phase is usually an inert carrier gas such as helium or argon. The carrier gas is continuously passed through a column containing the stationary phase. Most GCs now use capillary columns, which offer several advantages over packed columns. The stationary phase is coated uniformly on the inside of a capillary tube which eliminates problems associated with uneven packing.

Capillary columns are made of a flexible material so that longer lengths can be wound into compact coils that allow for a better resolution of the separated gas mixture [56].

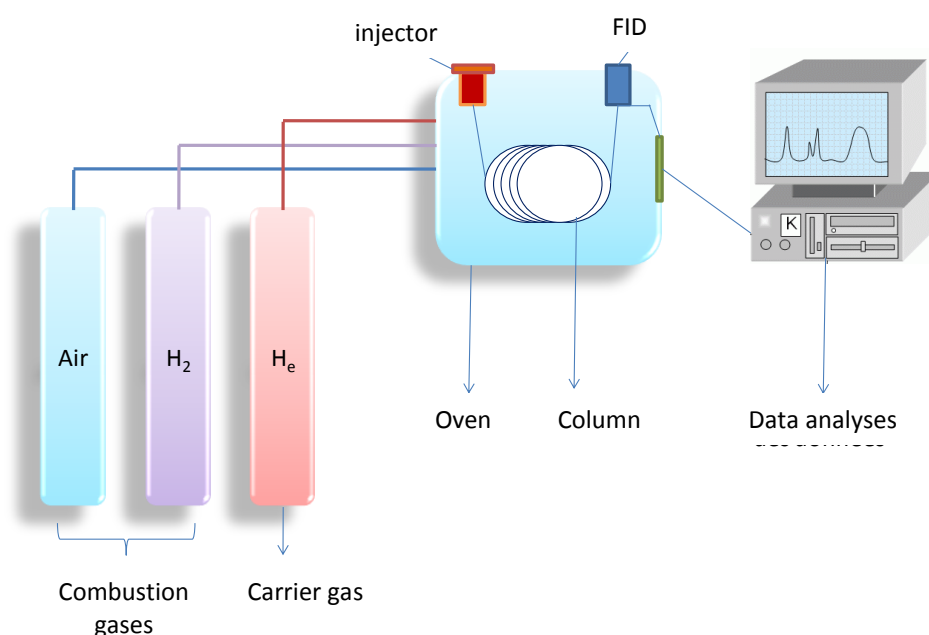


Figure 2.3. Schematic description of a gas chromatograph.

The mixture to be separated is injected into the column. Different gas species pass through the column at different rates depending on the strength of electrostatic interactions with the walls of the column. This causes the gas mixture to become

separated into individual components that reach the end of the column and are detected at different times (**Figure 2.3**).

By measuring the retention time of each species in the column, the component gases can be identified by comparison with chromatograms for known species. Retention times are affected by the gas concentration, flow rate and pressure as well as the column material and temperature [56], therefore selection of appropriate column materials and operating conditions are critical for resolution of the gas mixture. The signal produced by each gas as it reaches the detector results in a peak on the chromatogram at a residence time that is characteristic for that gas. The peak area is proportional to the gas concentration.

In this work, the organic compounds such as methane (CH_4), propane (C_3H_8), ethane (C_2H_6), ethyne (C_2H_2) and methanol (CH_3OH) were analysed by GC-mass spectrometry (Agilent technologies 7890B GC system coupled to a 5977B MSD) coupled with a flame ionization detector (FID) equipped with a HP-plot U column (HP-PLOT/U, length of 30 m x 0.32 mm i.d. 0.10 μm film thickness), helium was utilized as a carrier gas (1 ml/min). The operating condition were oven temperature of 140°C. for 15 minutes; FID temperature 180°C; Split injection 100:1; Injection temperature 110°C; Volume injected 0.5 ml. [Peux tu préciser la ref du liner?](#)

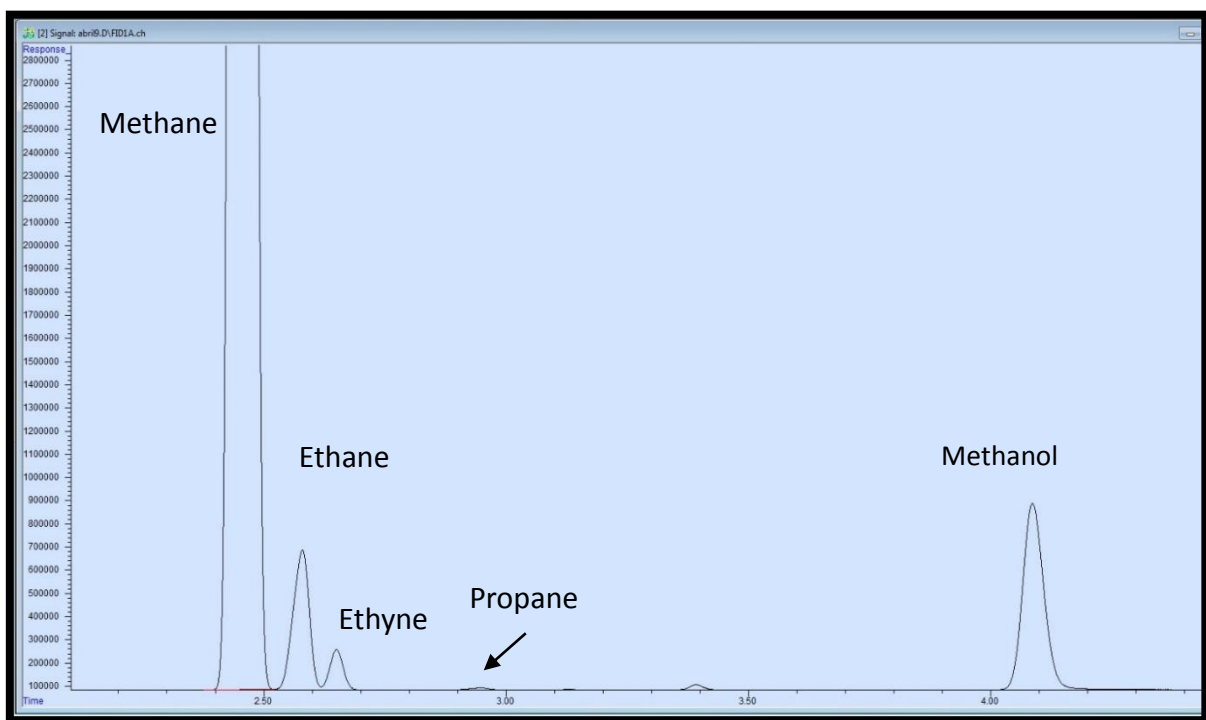


Figure 2.4. Example of a GC chromatogram of different organic compounds.

2.3.1. Micro-gas chromatography

Micro-GCs have several advantages over conventional instruments for gas chromatography, such as the small size of the required sample and of the instrument, which allow micro-GCs to be used for bench-top or portable applications. The run time for each sample is 5 minutes and it is not necessary to work with temperature programs which samples can be run back to back without the need for column cool down, which is necessary with conventional GC instruments.

A micro gas chromatography (Agilent technologies 490 micro GC) equipped with a thermal conductivity detector (TCD) has been used in this thesis for the gaseous analysis equipped which is presented schematically in **figure 2.5**. The micro-system contains two columns of different materials that use different carrier gases (Ar and He). The first one was used to calculate carbon monoxide (CO), hydrogen (H₂) and oxygen (O₂) concentrations (molecular sieve), the second column (HP-plot U column) was used for the quantification of methane (CH₄) and carbon dioxide (CO₂).

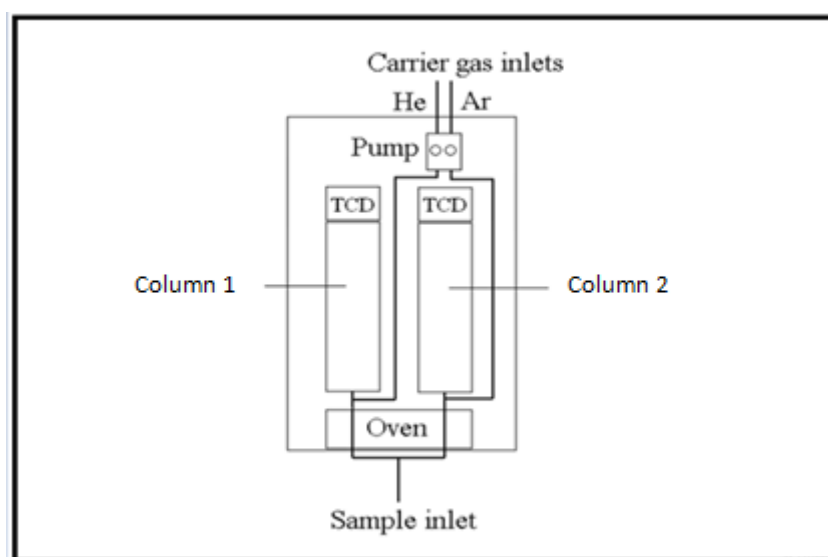


Figure 2.5. A schematic diagram of a two-channel Agilent 490 micro-GC with thermal conductivity detection.

Gas samples were pumped into the GC automatically and heated to a set temperature (80°C) before reaching the temperature-controlled column. The operating conditions for column 1 (molecular sieve) are injector temperature of 90°C, injection time of 50 ms, backflush time of 35 seconds to avoid the CO₂ contamination, the column

temperature was fixed at 50°C with a static pressure mode and initial pressure of 150 kPa, argon was used as a carrier gas in this column (**Figure 2.6b**).

For column 2 (Plot U), injector temperature of 90°C, injection time of 50 ms, the column temperature was fixed at 50°C with a static pressure mode and initial pressure of 150 kPa, helium was used as a carrier gas in this column (**Figure 2.6a**).

The micro-GC used for the experiments was regularly calibrated over a wide range of concentrations for each of the gases of interest. The methane (2.5 –50 %), carbon dioxide (5 –60 %) and hydrogen (5 –60 %) were calibrated using dilutions of the pure gases. The carbon monoxide (0.5 –4.5 %) was calibrated using dilutions (C₃H₈, CO and CO₂/N₂) of a 4.5 % carbon monoxide mixture. Calibration curves (GC peak area vs. concentration) were plotted for each gas and were used to determine accurate gas concentrations from GC peak areas during the experiments.

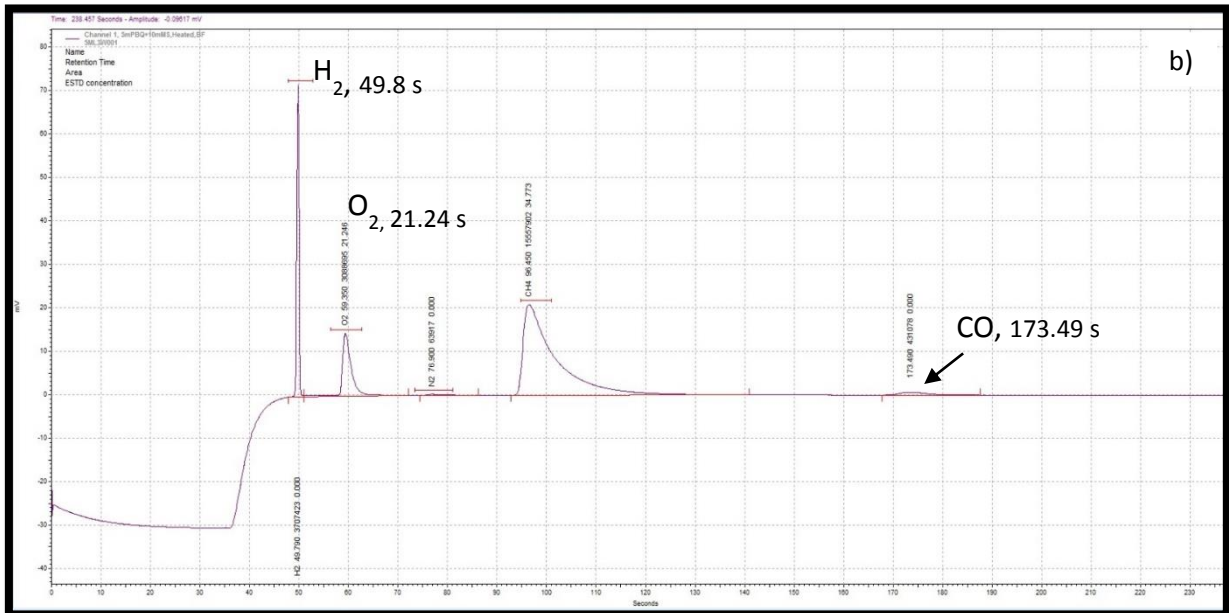
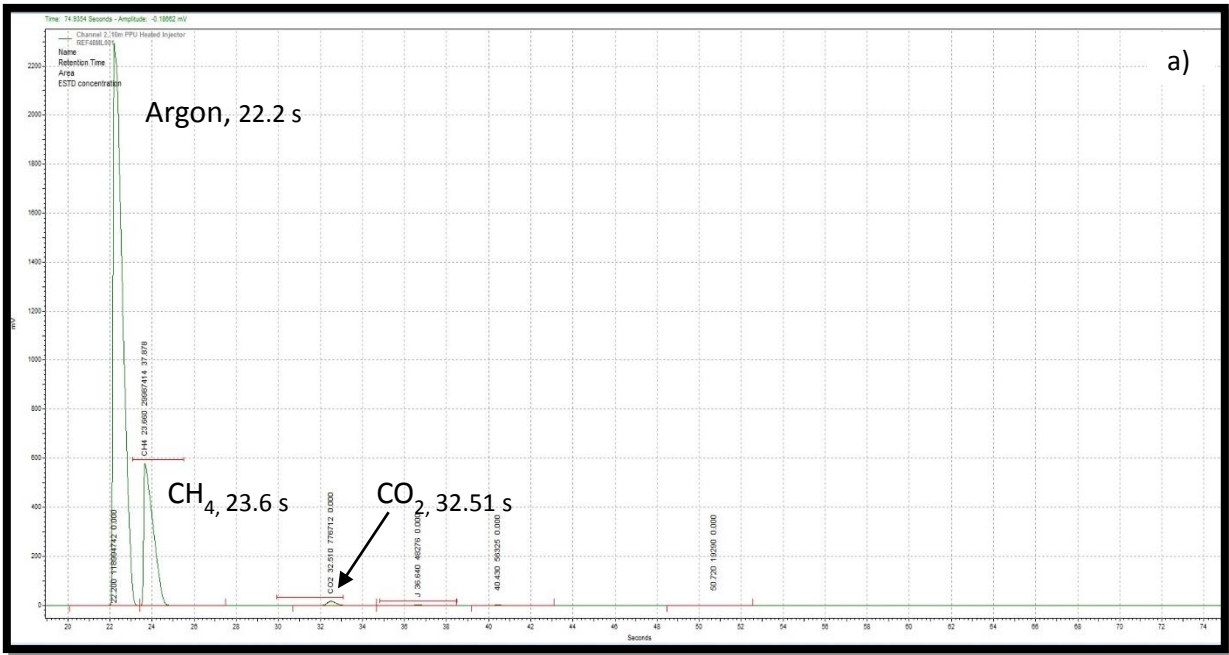


Figure 2.6. Gas chromatograms using Plot-U (a) and molecular sieve (b) in an Agilent 490 micro-GC with thermal conductivity detection

2.3.2. Thermal conductivity detection

Any gases which have a value of thermal conductivity different from the carrier gas can be identified by thermal conductivity detectors (TCD). TCD detectors integrate a many filaments in a Wheatstone bridge arrangement as depicted in **figure 2.7**.

The column effluent and reference gas enter cells containing analytical filaments, R3 and R4. The other filaments that make up the bridge (R1 and R2) have fixed

resistances therefore the change in voltage across the bridge is proportional to the change in resistance when a constant current is applied. The resistance of the analytical filament varies depending on the temperature, which is influenced by the thermal conduction of the gas being detected. The voltage across the bridge is measured and the signal is amplified to provide the GC response signal. Electrically heated tungsten-rhenium or platinum wires are typically employed for the analytical filaments [57].

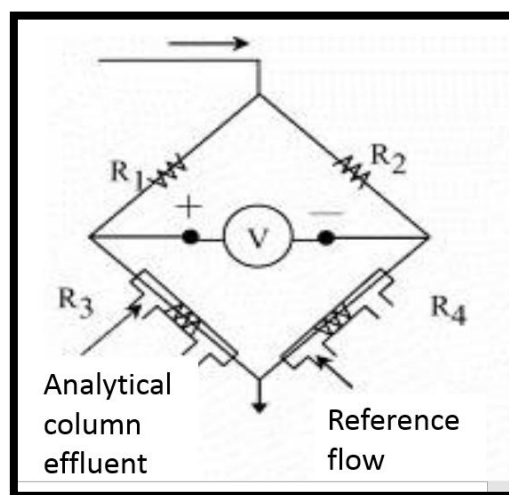


Figure 2.7. Schematic diagram of a typical thermal conductivity detector [57]

In the other hand is important to notice that the sensitivity in a TCD detector is usually low compared to an import variable flame ionization detector to measure low concentrations in addition the filaments often have a non-linear response and therefore require individual calibration for each type of gas being analyzed. Those are the main reasons for using a FID detector for the identification of hydrocarbons such as ethane, ethyne, propane and methanol.

2.3.3. Flame ionization detection

Due to their high detection limits flame ionization detectors (FIDs) are the most commonly used GC detectors for organic gases due to their high detection limits. In FID, the effluent gas from the column is mixed with H₂ and passed through a jet into a chamber, where it is mixed with air and ignited to produce a continuous flame. As different gases are eluted from the column, they pass into the flame and undergo combustion. A very small proportion (0.001 %) of the organic sample is ionized during combustion. The carbon ions are collected onto a polarized electrode, creating an

electrical signal that is amplified to provide the GC response signal [57]. There are correction factors between different families of hydrocarbons for a signal in FID, which allows to determine concentrations of hydrocarbons of different families with a single calibration. A major limitation of this method is the inability to detect H₂ and O₂ gases.

2.4. Conclusion

This chapter presents the materials to design a DBD plasma Millireactor and also the detection devices of compounds. This design and methods reported allow to characterize and lead to the understanding of the system during the reaction. In the following sections it is presented an experimental study and discussion about the performance of reactor and also the different reactions compounds. The implementation of the methodology is indispensable for an adequate monitoring of the behavior of the reactor and its characterization, which allows an adequate analysis of the results and a discussion as appropriate in the following chapters.

Chapter 3 : Fabrication and performance of a DBD plasma milli-reactor

3.1. Introduction to milli-reactor development

In this thesis, was studied the elaboration and investigation of a DBD plasma milli reactor system aimed at the partial oxidation of methane (POM) for methane valorisation.

Borosilicate was chosen as a base material for the fabrication of the proposed plasma-millireactor. Borosilicate is a type of glass with silica and boron trioxide as the main glass-forming constituents which can function as excellent dielectric ($\epsilon=4.6$ 20°C/1 MHz), essential property in the DBD systems to stabilize the discharge. Borosilicate glasses are known for having very low coefficients of thermal expansion ($3.3 \times 10^{-6} \text{ K}^{-1}$ at 20/300°C), making them resistant to thermal shock, more so than any other common glass.

It is transparent in the visible spectrum what facilitates the characterization experiments. It is also a material used for the design of different structures for ease of handling and it can be easily coated using conventional vacuum techniques without any surface processing. Thus, this material can withstand several technological steps including photo-patterning development. Sputter deposition and sub-micron size surface features could be easily reproduced using conventional laser graving techniques due to the good handling of the borosilicate material. Owing to these properties, the borosilicate is a great candidate for a plasma millireactor material.

Gold electrode was chosen due to its great chemical inertness to eventually avoid some oxidation problems which could degrade the electrode itself. Indeed, copper was used as the electrode material in the first prototypes and rapid degradation due to oxidation was observed as shown in **figure 3.1**.



Figure 3.1. Typical oxidation of electrode (made with copper) in presence of oxygen.

The **figure 3.2** shows the main technological steps: the borosilicate cap engraving by a laser (**Figure 3.2a**), the electrode elaboration by a combination of photopatterning and sputtering (**Figure 3.2b**), the alignment and finally the UV bonding of the chip by Norland Optical Adhesive (NOA) 81 (**Figure 3.2c**). The metallic electrodes were integrated by the use of a combination of photopatterning and sputtering which ensures good adhesion to the borosilicate surface. The geometry, dimensions and shape of the electrodes can be easily tuned. Finally, the bonding step consists of the application and UV exposition of NOA 81 in both borosilicate parts.

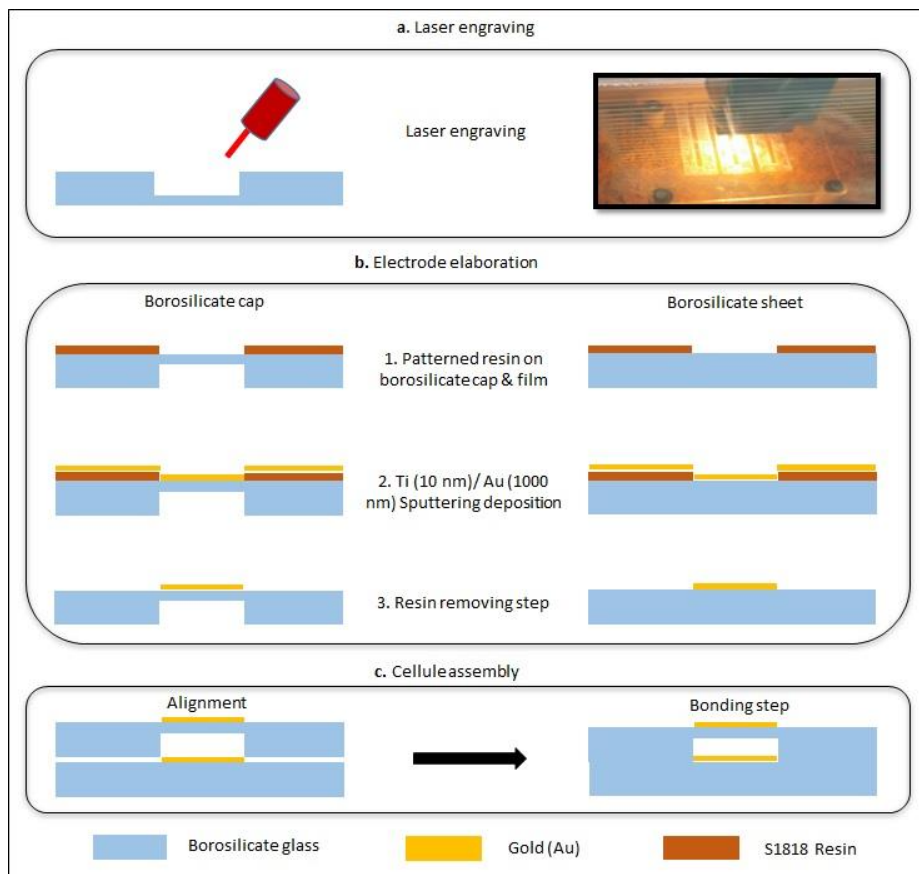


Figure 3.2. Principle of the multistep process investigated: (a) laser engraving, (b) electrode elaboration and (c) cellule assembly.

3.2. Reactor fabrication

In the following section is reported the development of a DBD plasma milli-reactor for the POM. The reactor was designed to be operated at atmospheric pressure and withstand possible temperature increases, with the ability to perform optical characterization (ICCD).

3.2.1. Plasma milli-reactor cellule fabrication

Borosilicate was purchased from Codex International ($\epsilon=4.6$ 20°C/1 MHz, transformation temperature equal to 510°C, 2 mm thick) and the gold target to use in the sputtering in order to make the electrodes deposition was purchased from NEYCO (99.999% w/w). The S1818 photoresin and Microposit 351 developer were obtained from Shipley®. The liquid adhesive NOA 81 was purchased from Norland Products Incorporated. It is sensitive to the entire range of long wavelength light from 320 to 380 nanometers with peak sensitivity around 365 nm. In order to complete the sealed

processes of the millireactor, a UV exposure ($30 \text{ mWatts.cm}^{-1}$, 2 minutes) is required.

3.2.2. Borosilicate glass engraving

Borosilicate glass sheet ($7\text{cm} \times 8\text{cm} \times 0.2\text{cm}$) was disposed in a laser machine in which we made an engraving in a serpentine form in order to have the borosilicate cap.

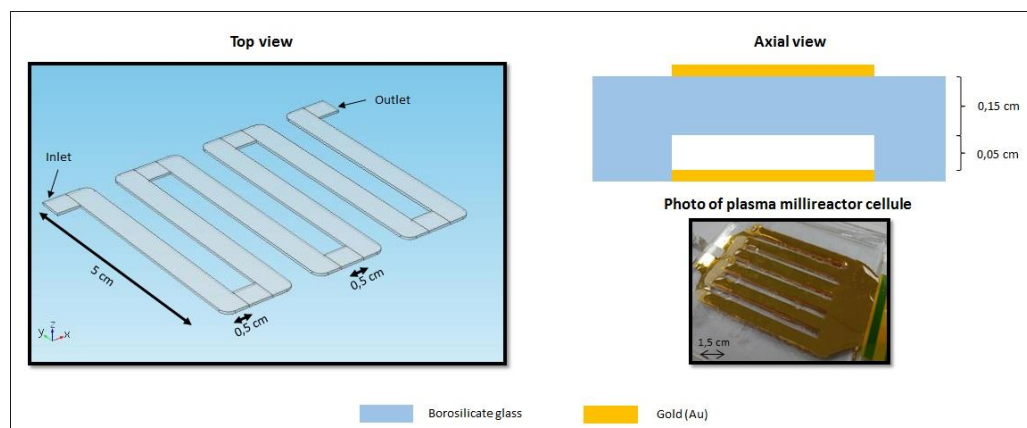


Figure 3.3. Geometry and dimensions of the plasma millireactor cellule.

Figure 3.3 shows its geometry and dimensions, the total channel consists of a 32.5 cm long x 0.5 cm wide x 0,05 cm high, obtaining an effective reaction volume of 0.8125 ml in the millireactor. This channel configuration allows to work in a wide range of residence times and provides in addition a high ratio of surface electrode relative to the millireactor volume.

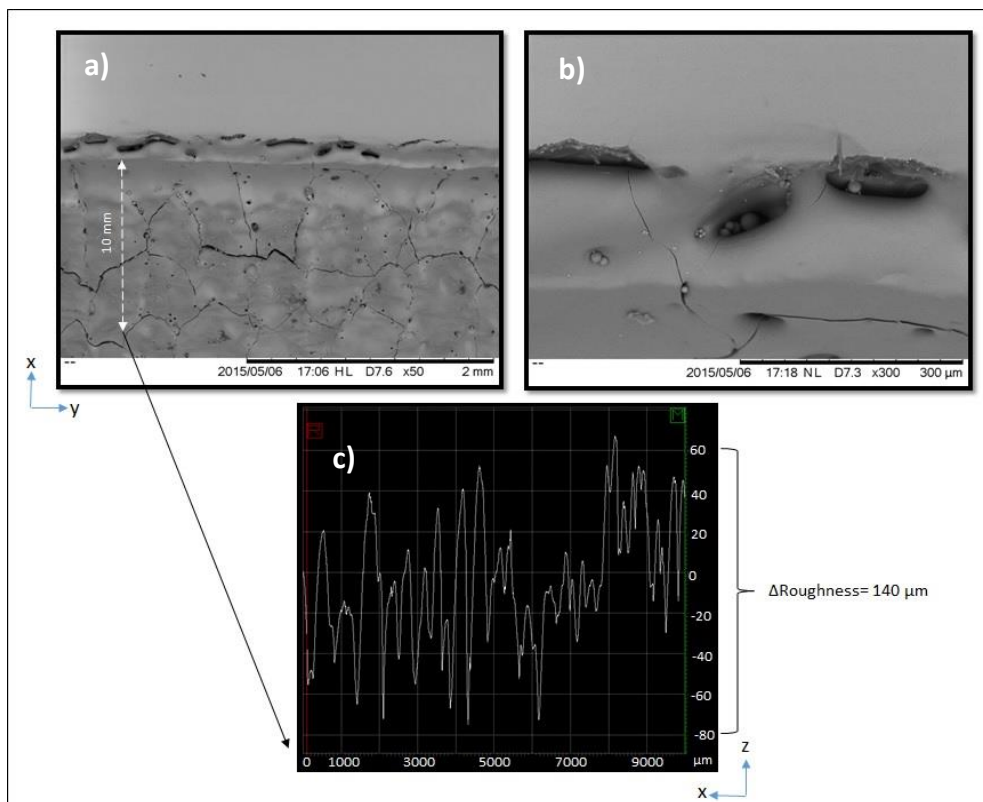


Figure 3.4. SEM Images at 2 mm (a) and 300 micrometers (b) of the bottoms and the roughness profile ($\Delta=140\mu\text{m}$) by mechanical profilometer (c) of the bottoms in the reactor.

Scanning electron microscope images in the edge of the engraving (millireactor's channel bottoms) are shown in **figure 3.4**.

The bottom of the channel has a highly rough surface, with the relief of up to 140 micrometers with a mechanical profilometer (Dektak). At the edges of the reactor channel it is possible to observe cavities of approximately 120 micrometers due to the borosilicate melt by the laser used for the engraving of the channel.

3.2.3. Electrode patterning

As shown in **Fig. 3.2b**, the electrodes were elaborated by lift off on the borosilicate cap and on a 2 mm thick borosilicate sheet with the same following conditions. First, a photopatterning step was completed. A 1.8 μm thick photoresin (S1818) was spin coated on the borosilicate substrates and cured for 90 s at 115 °C on a hotplate. Afterwards, each borosilicate substrate was aligned with a dedicated plastic mask which corresponds to the electrode geometric shapes and then exposed to UV using an EVG-620 Double Sided Mask Aligner (a main exposure wavelength of 365 nm). Finally, the resin was removed from the irradiated area using a mixture of deionized

water and 351 developer solution with a volume ratio of 1:4.

3.2.4. General description of the sputtering process

Sputter deposition is a physical vapor deposition (PVD), method of thin film deposition by sputtering, currently one of the most used in surface treatment. It was chosen because it presents a high degree of uniformity in the deposited film, it works at low temperatures, it is possible to make multicomponent depositions and it has a high control degree over the thickness of the film to be deposited.

The process is mainly an ionic bombardment, which achieves the vapor phase deposition of the bombarded material on a substrate, in this case borosilicate. In this technique, the ions formed in a plasma are accelerated towards the material to be deposited by an electric field.

Plasma is formed by process gases, in this case argon and oxygen, ionized by the strong electric field. The high voltage between the cathode and the anode causes the process gas ions to strike the target with enough energy to pull atoms out of the cathode surface by a moment transfer process as it is reported in Figure 3.5a.

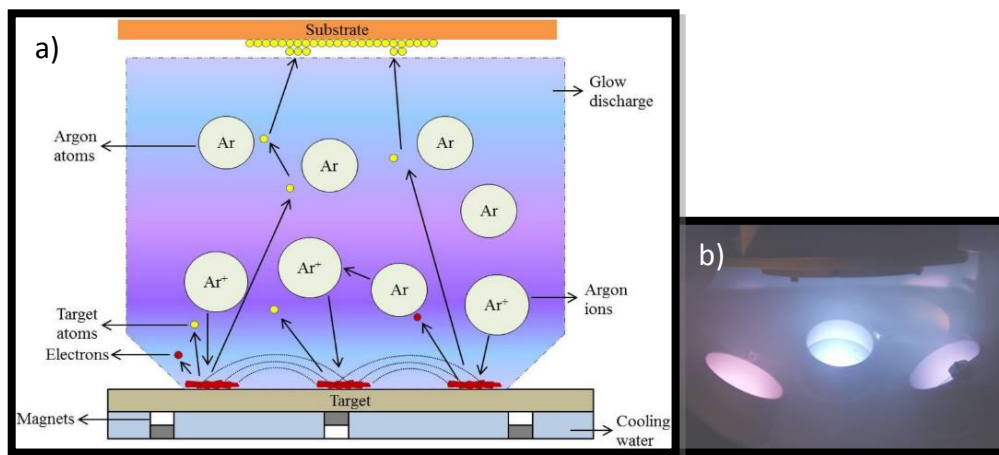


Figure 3.5. a) Graphical diagram of the operation of Sputter deposition and b) interior view photo.

When the ion strikes the surface of the material, it transfers some of its energy to the atoms that form it, and then a cascading collision occurs. The multiple collisions make it possible for some atoms in the material to acquire sufficient energy to leave the surface, reach the substrate and adhere to it. Most of the energy provided by the

incident ions is converted into heat, which is dissipated by a cooling circuit which prevents the cathode overheating[58].

Nonetheless, the process is limited by low deposition rates, high substrate heating and low ionization efficiencies. These limitations have been overcome by the development of magnetron sputtering system.

Magnetron sputtering is now considered as the most effective process for the deposition of a wide range of thin film materials. Magnetron sputtering systems generate a strong magnetic field near the target area, which causes the travelling electrons to spiral along magnetic flux lines near the target. This arrangement confines the plasma near the target area without causing the damage to the thin films being formed on the substrate, and maintains the stoichiometry and thickness uniformity of the deposited thin film. Moreover, in a radio frequency (R.F.) magnetron sputtering system, the generated electrons travel a longer distance, hence increasing the probability of further ionizing the inert gas atoms (Ar^+) and generating stable high-density plasma that improves the sputtering process efficiency [59].

R.F. magnetron sputtering offers additional advantages, including the use of non-conductive targets, charge-up effects and reduced arcing due to the use of alternating electric field (R.F.). It is important to note that R.F. magnetron sputtering is especially advantageous in the deposition of thin films using non-conductive target materials. This is at the cost of R.F. power supplies and an impedance matching network between the R.F. generator and the sputtering target [60].

3.2.5. Electrode deposition for POM

Sputtering was carried out using a hybrid deposition system (Plasmionique HSPT520). Once the resin layer was patterned, the electrodes were elaborated through magnetron sputtering. Borosilicate substrates were fixed on a rotated substrate holder to provide a uniform deposition (5 rpm). The chamber was first pumped down to reach a pressure of 6×10^{-6} Torr. Then a mixture of Argon and O_2 (2:1 mass flow ratio, Argon 20 sccm and O_2 10 sccm) was introduced into the chamber to reach the desired work pressure of 6 mTorr. First, the borosilicate surfaces were treated by argon/oxygen plasma in order to remove the low molecular weight fragments and to favour grafting of reactive oxygenated species. This was done by applying a RF bias (13.56 MHz) on the substrate holder. Secondly, borosilicates substrates were metallized with an 300 nm thick gold layer by DC magnetron sputtering from a gold target (Au, 99.99% pure, 2.00”

diameter.0.125" thick, Neyco S.A., France) with an applied power of 100 W. Prior to gold deposition, a 10 nm thick titanium layer (titanium target 99.97%, R.F. 75 W) was deposited in order to enhance the adhesion of the metallic layer onto the Borosilicate material. The thickness of the metallic electrodes was evaluated by White Light Interferometry (Zoomsurf 3D system from Fogale Nanotech Company). The resist was finally removed in an acetone bath in combination for 30 min. Then the acetone was allowed to evaporate itself from the samples.

3.2.6. Electrode deposition for discharge characterization

For the discharge characterization was used the ICCD technique allowing to observe continuously the evolution of the homogeneity of the discharge respect to the voltage, frequency and conversion of the system. For that purpose, an ITO/Au/ITO multilayer films was made In order to increase the conductivity of deposited ITO films in the top part of the reactor, This allows to have the transparency and conductivity desired for these technique. The following process was inspired in the thesis reported by Zhang [61].

The ITO target ($\text{In}_2\text{O}_3/\text{SnO}_2$, 90/10 wt%, 99.99% pure, 2.00" diameter, 0.125" thick indium bonded to 2.00", diameter 0.125" thick of HC copper backing plate, Kurt J. Lesker Company Ltd., UK) was mounted on one of the RF magnetrons. A 2" gold target (Au, 99.99% pure, 2.00" diameter.0.125" thick, Neyco S.A., France) was mounted on the DC magnetron of the reactor.

Table 3.1. Deposition protocol for ITO/Au/ITO films.

<i>Sub-process</i>	<i>Parameter</i>	<i>Value</i>
Substrate cleaning		
	Gas	Argon (30 sccm)
	Pressure	6 mTorr
	Power	50 Watts
	Time	2,5 min
Deposition		
	Gas	Argon (30 sccm)
	Pressure	6 mTorr
Pre-sputtering (ITO target)	Initial Power	30 Watts
	Final power	60 Watts
	Power ramp	5 Watts/min
Sputtering (ITO target)	Sputtering power	60 Watts
	Sputtering time	20 min (two steps)
Pre-sputtering (Au target)	Sputtering power	30 Watts
	Sputtering time	1 min
Sputtering (Au target)	Sputtering power	30 Watts
	Sputtering time	4 min

In **Table 3.1** are reported the different parameters and their values for the electrode deposition for discharge characterization. The sputtering chamber was first pumped down to reach a pressure of 6×10^{-6} Torr then a first deposition of ITO was performed at a R.F. 60 W and a deposition time of 10 min. After that a second deposition made in gold was performed at R.F. 30 W and 4 min as a deposition time. Finally a third deposition of ITO with the same parameters of the first deposition was made. A thermal treatment was made in order to increase the conductivity of the deposited ITO thin films, the increment of temperature was fixed at 100 °C/hr until reaches 300 °C for 2 hours.

In **figure 3.6a** shows the final cellule tested in a flow of argon at 50 sccm (10.8 kV 1000 Hz).

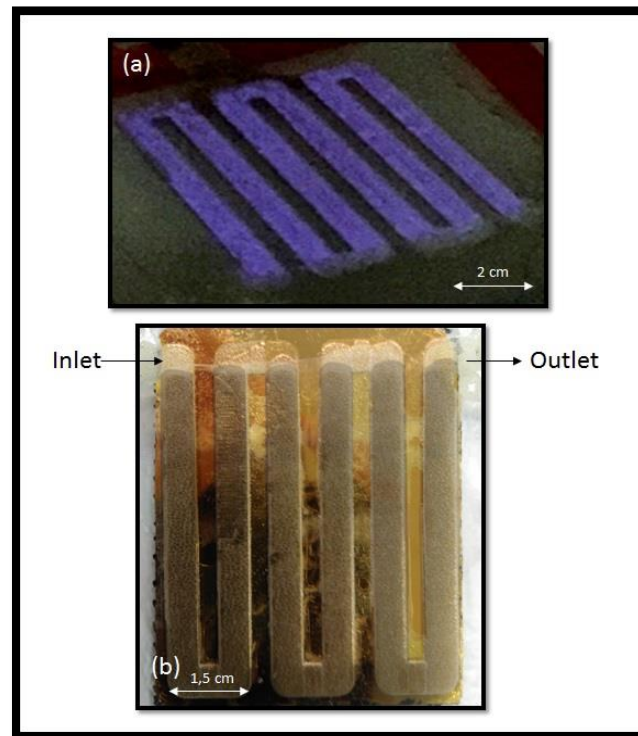


Figure 3.6. (a) Argon (50 sccm) discharge performed within the millichannel and (b) Transparent plasma millireactor cellule. The experiment was carried out at atmospheric pressure and room temperature (10.8 kV, 1 kHz).

3.2.7. Sealing step

For the sealing process of the reactor, it is necessary to have a technique that is safe, clean and does not present losses of transmission of visible light. NOA 81 is a liquid adhesive that cures in seconds to a tough, hard polymer when exposed to ultraviolet light and can provide excellent light transmission over a wide spectral range. Also it has a long shelf-life. Optical glues are designed for bonding when required strain resistance, optical clarity or low outgassing. The optical glues are currently used in different areas such as military equipment, aerospace, fiber optics or commercial optics.

NOA 81 is sensitive to the entire range of long wavelength light from 320 to 380 nanometers with peak sensitivity around 365 nm. Cure time is dependent on light intensity and thickness of the drop applied. To fully cure the material requires 2

Joules.cm⁻² of energy. The adhesive is designed to be cured with small hand held or desktop UV light sources that are easy to use.

Afterwards, the upper and lower borosilicate substrates were aligned and bonded together by the use of a syringe for the application of small drops of NOA 81, thus avoiding splits inside by NOA 81 with a time of exposure of two minutes in a UV lamp with 30 mW.cm⁻².

Gaseous flow along the channel was ensured by plugging commercially available microfluidic connections. Figure 3.6b shows the final cellule.

3.3. Electrical characterization of the reactor

In **table 3.2** are presented the values of breakdown voltages for different gases, including gas reaction mixtures, when the gas flows in the plasma millireactor cellule at constant flow rate of 48 sccm and pressure in the milli-reactor around 1 atm.

Table 3.2. Values of breakdown voltages for different pure gases and gas reaction mixtures at constant flow rate of 48 sccm

Gas concentration (v/v)	Experimental breakdown voltage kV
Ar=1	2,8
CH ₄ =1	7,2
O ₂ =1	7
a)O ₂ /CH ₄ =0,5	7
b)O ₂ /CH ₄ =0,5 ; Ar =0,375	5.1

It is observed that the breakdown voltage of argon is 2.8 kV and that this value is significantly lower than methane and oxygen which present breakdown voltages of 7.2 and 7 kV respectively. Those results show the ease with which plasma discharges are created in noble gases such as Ar.

The breakdown voltage dependence on the parameters p*d is usually referred as the Paschen curve, and is presented for a given gas. The values of breakdown voltage for methane, oxygen and argon are shown in **table 3.3**. These values were taken from

curves of Paschen for each gas considering atmospheric pressure (p) and gaseous gap (d) equal to 0.5 mm.

Table 3.3. Semi-empirical values of breakdown voltage for methane, oxygen and argon at 38 (Torr.cm), [29] c), [62] a), b).

Gas	Semi-empirical breakdown voltage (kV)
a) Methane	1.6
b) Oxygen	1.7
c) Argon	0.6

It is observed the values of breakdown voltage for methane and oxygen are very similar between them (1600 and 1700 V respectively). In the other hand the breakdown voltage for argon is around 2.5 times lower than the breakdown voltages of methane and oxygen, with a value equal to 600 V.

This behavior in the breakdown voltages is very similar to that reported in **table 3.2** for the experimental breakdown voltages. The difference between the experimental and semi-empirical values of breakdown voltages is mainly due to the fact that the experimental values presented in **table 3.2** give the voltage to be applied across the experimental composite system consisting of a gas layer and a dielectric whereas the values in **table 3.3**, obtained from Paschen curve, take into account the gas layer only.

In **table 3.2** also is reported the breakdown voltage for the reaction mixture (b) which is equal to 5.1 kV. It is important to notice that the incorporation of argon in the mixture decreases the breakdown voltage of the total gas reaction mixture, compared with the O₂ and CH₄ mixture (a) without argon reported in the same table.

Electrical breakdown is a complicated multistage threshold process that occurs when the electric field exceeds some critical value. This mechanism of ignition of a self-sustained current in a gap controlled by the secondary electron emission coefficient (α) is usually referred to as the Townsend breakdown mechanism [29].

This coefficient indicates the production of electrons per unit length along the electric field.

It is important to notice that the value of α for noble gases is higher than other gases [36], which explained that if we introduce argon the breakdown voltage of the global mixture decreases.

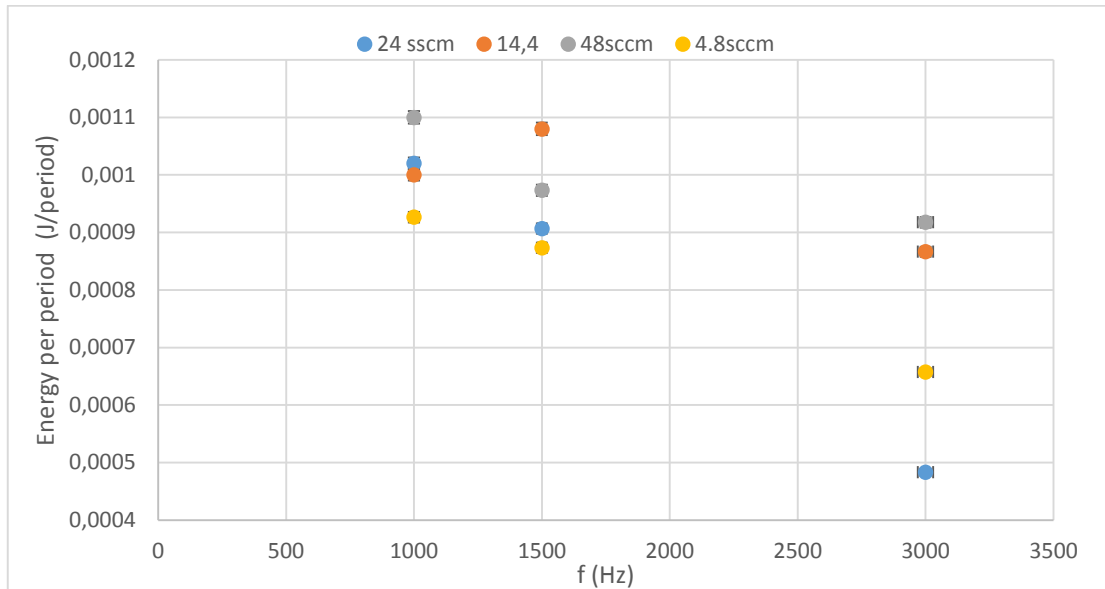


Figure 3.7. Energy per period injected in the reactor as a function of frequency at constant tension equal to 10.8 kV, O_2/CH_4 ratio equal to 0.5 (v/v) and concentration of argon equal to 0.375 (v/v)

In **figure 3.7** are presented the energy per period as a function of frequency at constant tension equal to 10.8 kV for a gas reaction mixture composed by a ratio of O_2/CH_4 equal to 0.5 and concentration of argon equal to 0.375 (v/v). It is observed that the energy per period decreases if the frequency increases and that there is not a notable influence of the flow rate on the energy per period at 1000 and 1500 Hz.

Nevertheless, at 3000 Hz, it is noticed that the energy per period varies a lot, from 0.0005 J to 0.0009 J, when the flow rate varies. However there is not a clear relation between the value of the energy per period and the value of the flow rate.

The decrease of the energy per period when the frequency increases could be due to the change of the gas mixture composition. Indeed at constant voltage and flow rate, higher frequencies are associated to higher methane conversions.

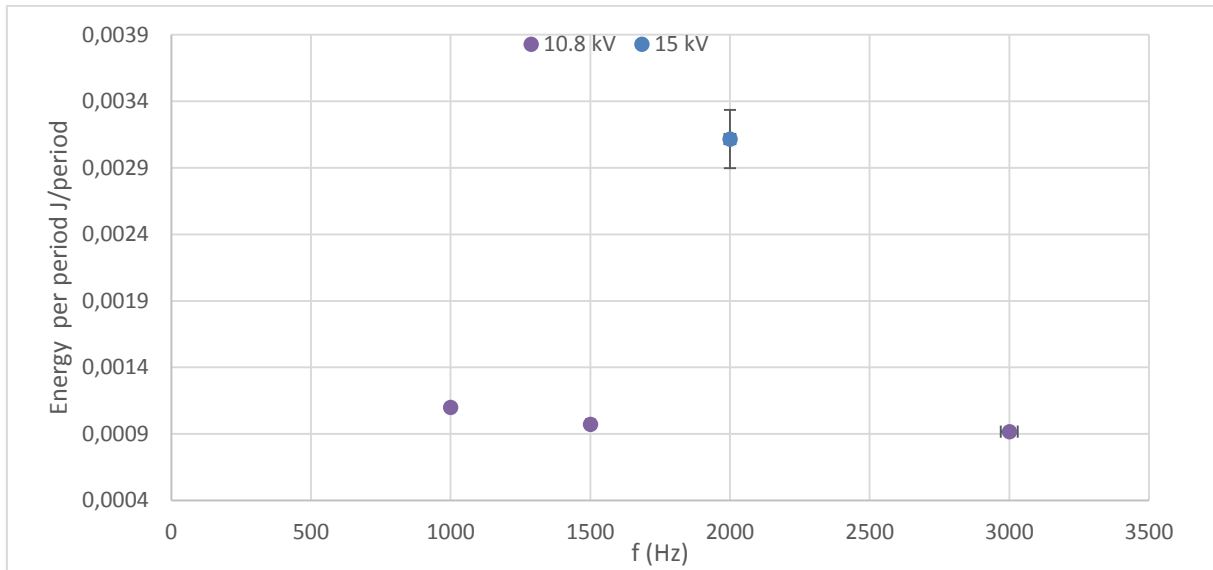


Figure 3.8. Energy per period as a function of the frequency at two different values of tension for the reaction mixture for a flow rate of 48 sccm, O_2/CH_4 ratio equal to 0.5 (v/v) and concentration of argon equal to 0.375 (v/v).

In **figure 3.8** is showed the energy per period as a function of the frequency at two different values of tension for the reaction mixture for a flow rate of 48 sccm, O_2/CH_4 ratio equal to 0.5 (v/v) and concentration of argon equal to 0.375 (v/v). It is observed that at 10.8 kV the energy per period has an almost constant value as the frequency increases. On the other hand, if the voltage increases (15 kV) at a comparable value of frequency, the energy per period increases logically significantly.

3.3.1. Influence of the argon percentage on the electrical characteristics of the discharge

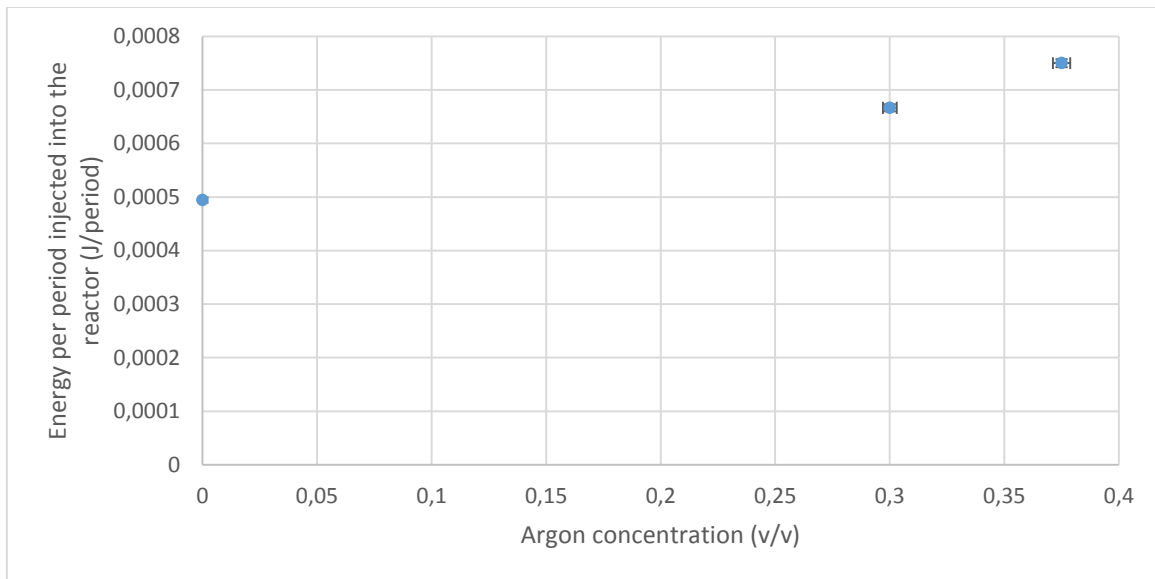


Figure 3.9. Energy per period injected in the reactor as a function of argon concentration at constant tension, frequency, O₂/CH₄ ratio and flow rate equal to 10.8 kV, 3000 Hz, 0.3 v/v and 48 sccm respectively.

In **figure 3.9** is showed the behavior of the energy injected into the system as a function of the concentration of argon at constant value of tension, frequency, O₂/CH₄ ratio and flowrate. It is observed that the energy value per period increases if the concentration of argon increases from a value of $5 \cdot 10^{-4}$ to $7.5 \cdot 10^{-4}$ (J/period) at a delta of concentration of argon equal to 0.375 (v/v).

This behavior is consistent with that reported by Okumoto et al. [49], [52]. This possibly due to the fact that the increment of concentration of argon favors the production of metastable argon (Ars) which then reacts with stable gas molecules (penning effect) changing to a reactive medium with higher energy demand.

3.3.2. Influence of the O₂/CH₄ ratio on the electrical characteristics of the discharge

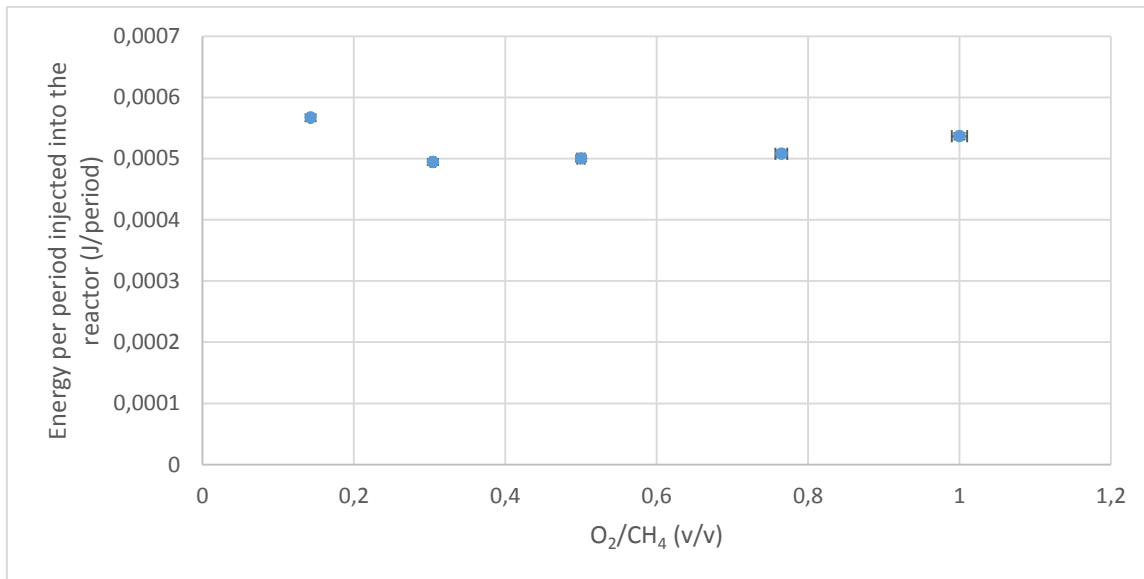


Figure 3.10. Energy per period injected in the reactor as a function of O₂/CH₄ ratio without presence of argon at constant tension, frequency, and flow rate equal to 10.8 kV, 3000 Hz, and 48 sccm respectively.

In **figure 3.10** is showed the behavior of the energy injected into the system as a function of the concentration of O₂/CH₄ ratio without presence of argon at constant value of tension, frequency, and flowrate. It is observed that the energy per period is almost constant and its value is reported around 5 E10⁻⁴ (J/period). This is because the semi-empirical breakdown voltage between the oxygen and methane is similar. Therefore, it could be indicated that the ionization process of O₂ and CH₄ is similar.

3.4. Characterization of discharge uniformity by ICCD measurements

3.4.1. ICCD measurements in pure gases

In **figure 3.11** are showed the ICCD images taken in the reactor channel at constant power of 3 Watts and 48 sccm as a flow rate in three different gases (methane, argon, and oxygen). In all ICCD experiments the gating of the camera was set equal to the time of a half period of frequency with an accumulation of 20 photos and a gate delay 0.31 μs. In **figure 3.11** the reported images were made a 3000 Hz and gating equal to 0.000167 seconds.

It can be observed that in the case of argon and oxygen, the discharge is rather

uniform, with micro-discharges evenly distributed in the channel. Some preferential paths (indicated by brighter points) can however be distinguished on the pictures. These preferential points are likely caused by the roughness of the glass (**figure 3.4**). On the contrary, the discharge is strongly not uniform in the case of methane, with dark and bright large areas. This behavior may be caused by the chemical reactions that can take place when CH_4 is introduced in the millireactor. It is likely that O_2 is present in trace in the milli-reactor, either because it is present in the CH_4 as an impurity, or because of micro-leaks in the experimental set-up. In the presence of both CH_4 and O_2 in the plasma discharge, exothermic reactions can take place (combustion-type reaction). These reactions could locally increase the temperature, thus increasing locally the electric field and increase the formation of preferential zones where the discharges are located thus the inhomogeneity of the discharge.

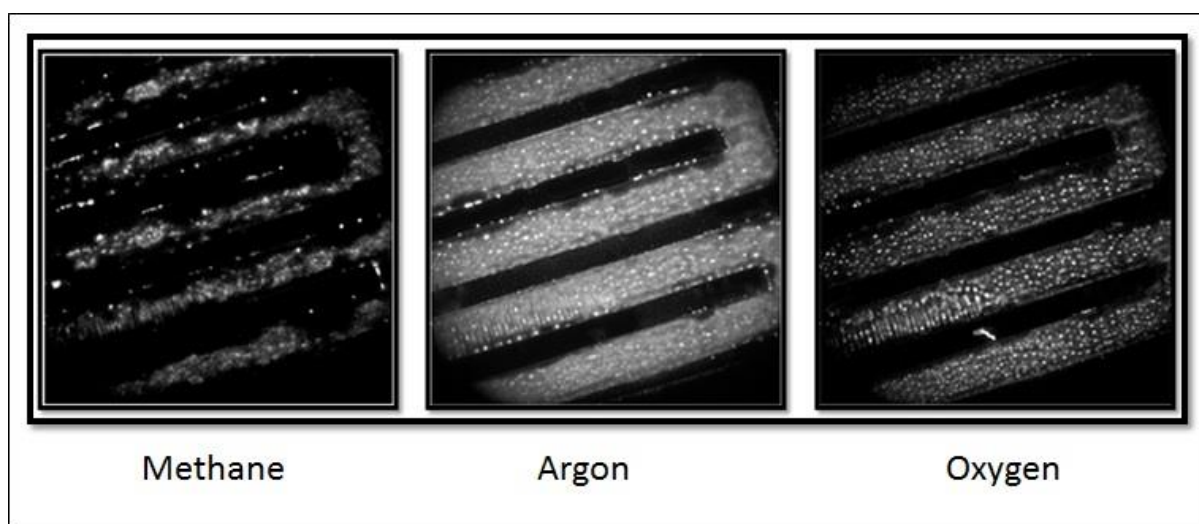


Figure 3.11. Images of the reactor channel taken with an Intensified Charge Coupled Device (ICCD) camera, they show the three different pure gases (methane, argon and oxygen) at constant power of 3 Watts and 48 sccm.

3.4.2. ICCD measurements $\text{CH}_4/\text{O}_2/\text{Ar}$ mixture

Figure 3.12 shows the the ICCD pictures taken in the reactor channel at a constant flow of 4.8 sccm, O_2/CH_4 ratio equal to 0.5 v/v and concentration of argon of 0.375 v/v at different powers. This flow rate is the minimum possible with the available flowmeters.

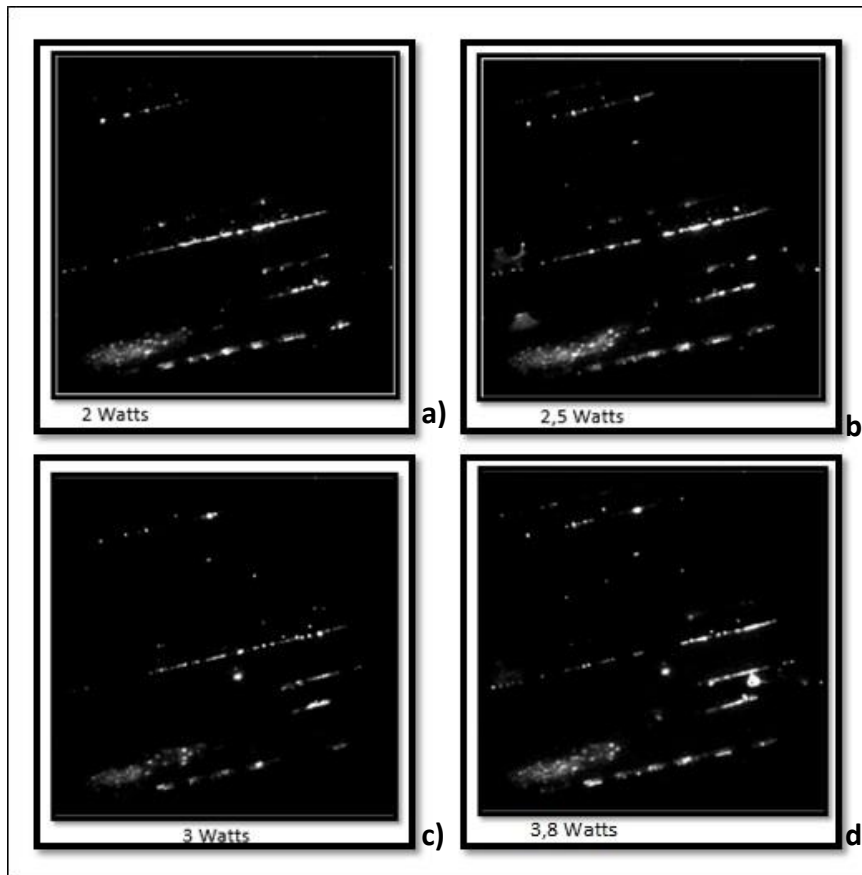


Figure 3.12. Images of the reactor channel taken with an Intensified Charge Coupled Device (ICCD) camera. Effect of the power (Watts) in the reactive mixture a) 2, b) 2.5, c) 3, d) 3.8 at a constant flow of 4.8 sccm.

The images indicate that the DBD discharge is highly non uniform, the discharge being localized at the gas inlet and near the reactor walls. As already showed (**figure 3.9**), the discharge was much less uniform in CH_4 compared to Argon and oxygen possibly due to exothermic reactions due to the presence of traces of oxygen. With the present mixture, the phenomenon of preferential paths for the discharge may be more pronounced due to the high concentration of oxygen in the medium. It is also observed that the discharge uniformity is almost independent of the power, the activated plasma zone being almost constant whatever the applied power.

In **figure 3.13** are presented the ICCD pictures showing the discharge in the millireactor when the mixture of CH_4 , O_2 and Ar (O_2/CH_4 ratio equal to 0.5 v/v and concentration of argon of 0.375 v/v) is introduced in the millireactor at a constant power

of 3 W, the gas flow varying between 4.8 and 48 sccm.

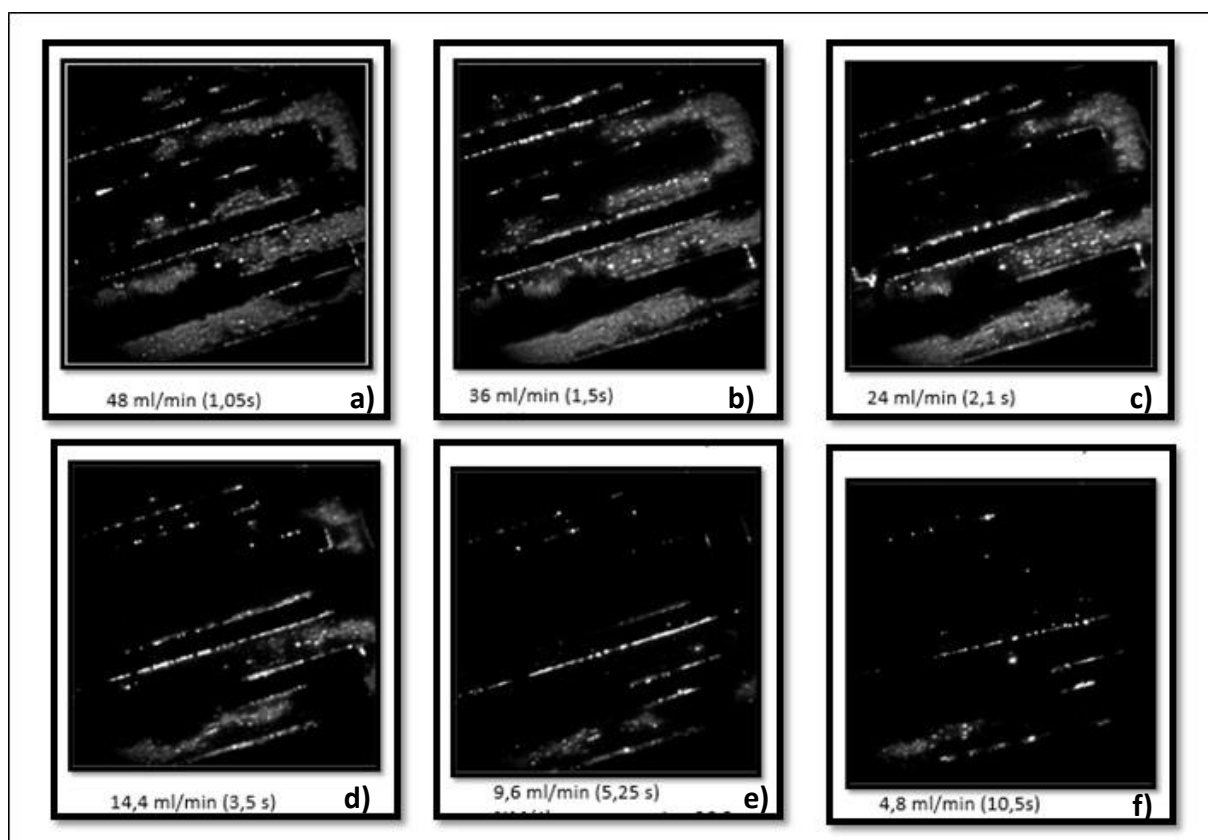


Figure 3.13. Images of the reactor channel taken with an Intensified Charge Coupled Device (ICCD) camera, to show the effect of the flow rate in the reactive mixture ($\text{ml}\cdot\text{min}^{-1}$) a) 48, b) 36, c) 24 d) 14.4, e) 9.6, f) 4.8 at a constant Power of 3W.

The results show that the homogeneity of the discharge depends on the gas flow in the milli-reactor. When the gas flow increases, the discharge becomes more uniform. It can be assumed that a high gas flow lessens the local increase of the temperature caused by exothermic reactions thanks to the removal of heat by convection.

3.5. Conclusion

In this chapter the fabrication of a plasma-millireactor was presented, with the purpose of using it to perform the partial oxidation of methane at atmospheric pressure and with support of possible temperature increases due to the nature of the reaction. The reactor was also designed to perform optical characterizations (ICCD), through the development of a transparent electrode made with an alloy of ITO / Au / ITO.

Its electrical performance for the different gases studied in this thesis (argon, methane and oxygen) also was showed. It was found that the frequency has a slight influence on the energy injected into the system compared to the tension. On the contrary a slight increase in the value of tension has a considerable impact on the energy injected into the system and this is independent of the type of gas studied.

The optical characterization of the discharge by ICCD was also carried. It was found that the volumetric flow has a great influence in the homogeneity of the discharge and therefore in the energy distribution in the millireactor. It is reported that higher volumetric flow values show improvements in discharge uniformity along the millireactor channel. The repercussions that this phenomenon presents in the POM are of great importance, since it could have an important effect on the selectivities of the products in the reaction.

In Chapter 4 are presented the different hypotheses and discussions about the influence of the variables and phenomena current during the Partial Oxidation Methane, as well as a characterization of the main products generated for the production of methanol.

Chapter 4 : **Performance of the plasma milli-reactor for the partial oxidation of methane (POM)**

4.1. General performance for partial oxidation of methane (POM)

By definition, specific input energy per mole of methane processed (SIEM) is the quantity of energy per mole of methane processed in the reactor. This definition has been utilized to have an easy way to compare efficiency and behavior in a variety of reactor configurations. SIEM is calculated using the following equation 4.1;

$$SIEM = \frac{\dot{w}}{\dot{n}_{\text{methane in}}} = \left[\frac{\text{J}}{\text{mol}} \right] \quad \text{Eq. 4.1}$$

In this equation, $\dot{w} = E_{\text{discharge}} \cdot f$ represents input power, where f is the operating frequency (s^{-1}); E is the discharge energy per cycle (J); $\dot{n}_{\text{methane in}}$ is the quantity of methane per second at the reactor inlet ($\text{mol} \cdot \text{s}^{-1}$). Percent of methane conversion as a function of SIEM are showed in **figure 4.1** at a constant oxygen/methane volume ratio and argon concentration ($\text{O}_2/\text{CH}_4=0.5$, $[\text{Ar}] =0.375$ v/v) and at different values of flow rate processed in the reactor. It is observed that is possible to reach until 31 percent of methane conversion at $3000 \text{ kJ/mol}_{\text{methane in}}$ as SIEM.

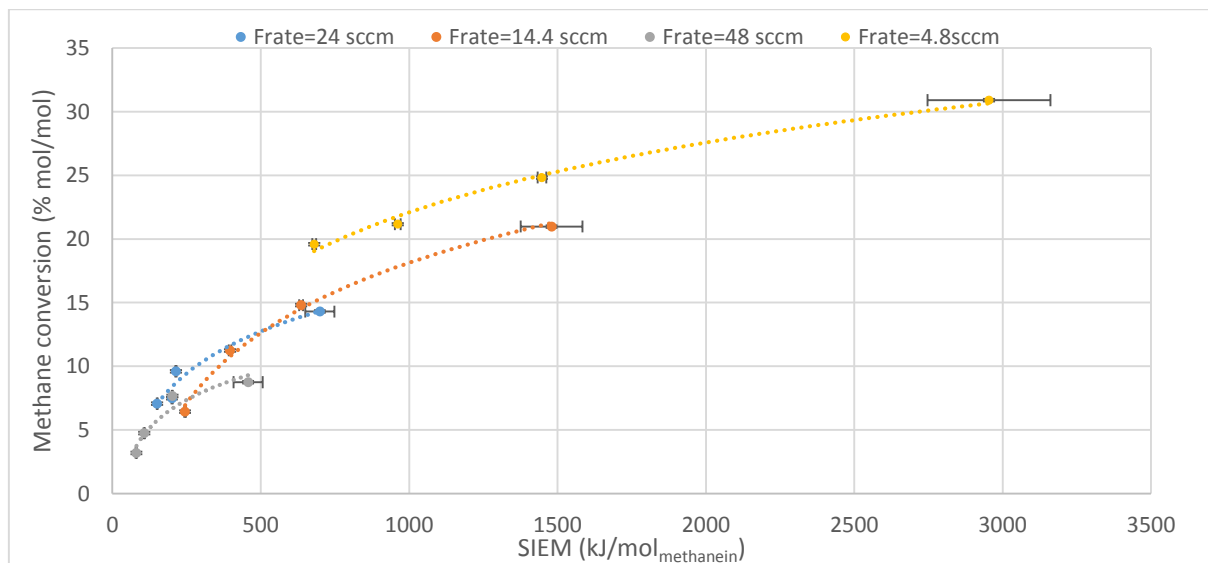


Figure 4.1. Methane conversion as a function of SIEM at different values of flow rate (4.8;14.4;24;48 sccm), constant value of O_2/CH_4 ratio (0.5 v/v) and concentration or argon (0.375 v/v).

It is logically observed that the methane conversion increases as the value of SIEM increases and this behavior is almost independent of the flow rate. However, at higher values of SIEM the increment in methane conversion is lower. This is likely due to the decrease of methane concentration and the increase of the intermediate oxidation

products, favoring competitive reactions. The reaching of a plateau for methane conversion at high SIEM can also be explained as follows: in **Figure 4.2**, are showed the methane and oxygen conversion as a function of SIEM. It is observed that the conversion of oxygen increases faster that the conversion of methane. At 1500 kJ/ mol_{methanein} the oxygen and methane conversions are respectively 45 % and 20 % and at 3000 kJ/ mol_{methanein} these values are 80 and 30%. Thus, a low concentration of oxygen from this value of SIEM may limit oxidation reactions in general and in particular the oxidation of methane.

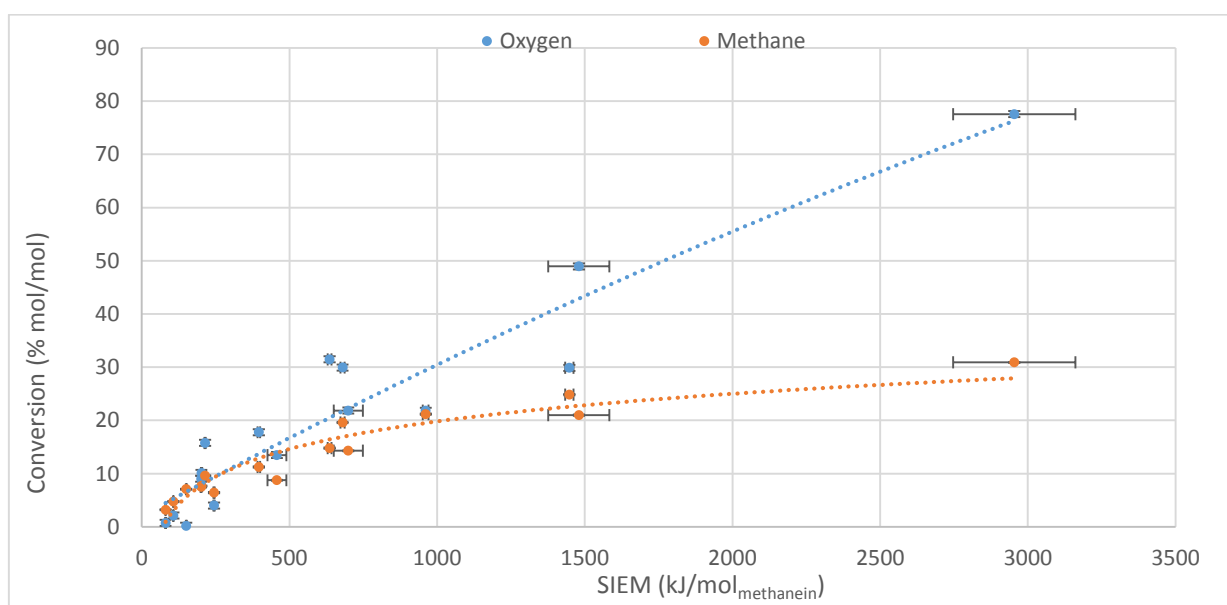


Figure 4.2. Methane and oxygen conversion as a function of SIEM at constant value of O₂/CH₄ ratio (0.5 v/v) and argon concentration (0.375 v/v).

A characterization and quantification of the main reaction products was also carried out. In the **figure 4.3**, the different compounds found are reported as a function of SIEM at constant O₂/CH₄ ratio equal to 0.5 v/v and argon concentration (0.375 v/v) for the different values of flow rate processed in the reactor.

The three principal compounds identified are carbon monoxide (CO), hydrogen (H₂) and carbon dioxide (CO₂), this last compound reaches a maximal value of selectivity equal to 30% at 40 % of methane conversion. In the other hand, the main hydrocarbon compounds identified are methanol, ethane, ethyne and propane reaching 6, 18, 4 and 16% as maximum selectivity values respectively.

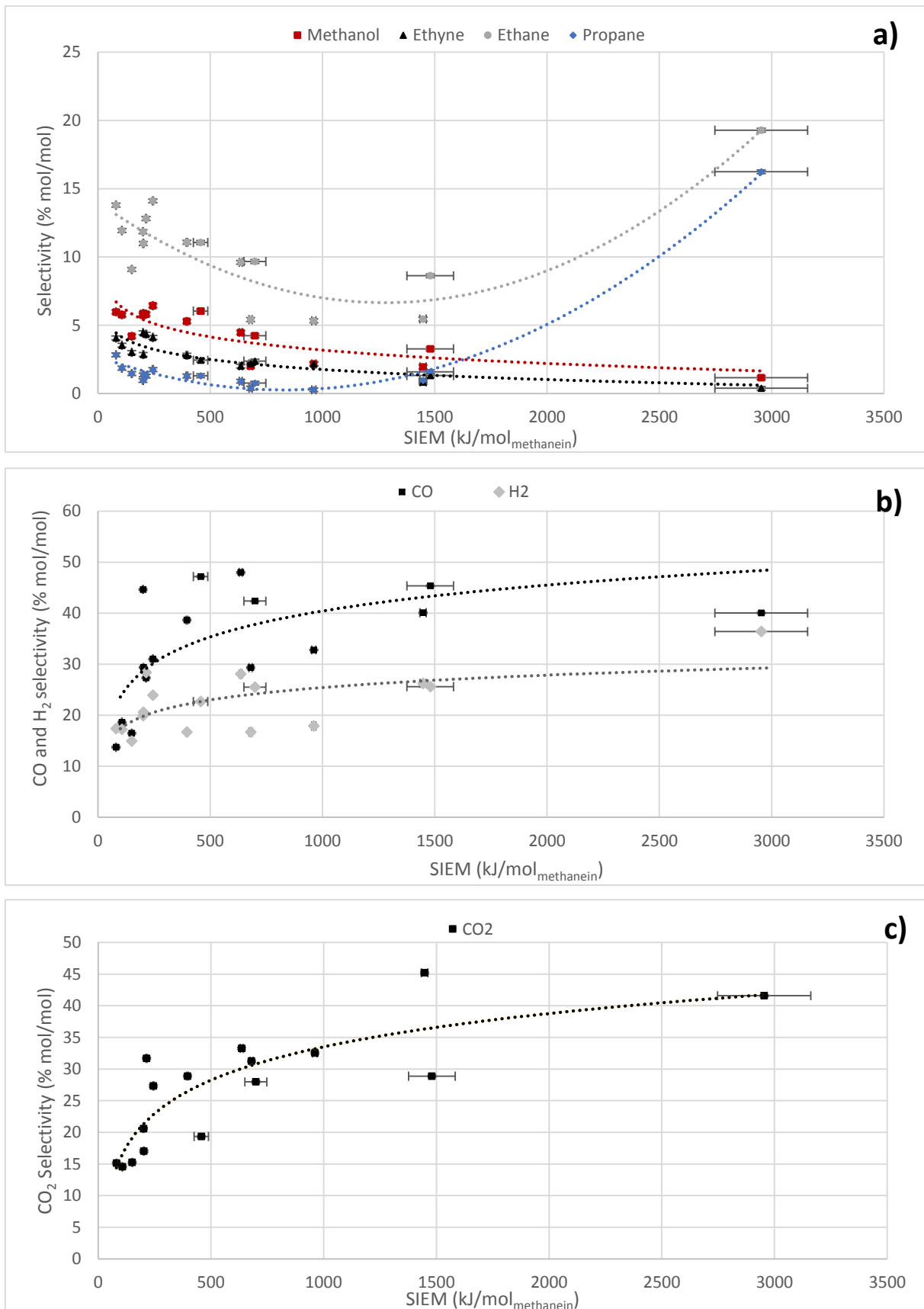


Figure 4.3. Selectivity of the POM's compounds (a) hydrocarbons (b) CO and H₂ (c) CO₂ as a function of SIEM at different values of flow rate (4.8; 14.4; 24; 48 sccm), constant value of O₂/CH₄ ratio (0.5 v/v) and concentration of argon (0.375 v/v).

Up to $1500 \text{ kJ/mol}_{\text{methane in}}$ the general trend is an increase of the selectivities of light compounds (H_2 , CO , CO_2) and a decrease of the selectivities of hydrocarbons when SIEM increases. This result indicates that hydrocarbon products can be considered as intermediate reaction products and can be easily destroyed at high SIEM values. From $1500 \text{ kJ/mol}_{\text{methane in}}$ it is observed (**figure 4.3 a**) that the selectivities of propane and ethane increase drastically. At the same time, there is also a slight decrease in CO and CO_2 selectivities from $1500 \text{ kJ/mol}_{\text{methane in}}$. These results can be explained by the fact that at high SIEM values there is almost no more O_2 in the reaction medium because O_2 , which is the limiting reagent (**figure 4.2**), has been almost totally consumed. As soon as there is no more O_2 , the reaction products coming from CH_4 dissociation become exclusively hydrocarbons (ethane and propane) and H_2 . In oxygen poor conditions at similar values of SIEM [63] it is reported that the main compounds produced in the reactor are ethane and propane which is coherent with the results reported in **figure 4.3 a**.

In **figure 4.4** is reported the carbon missing in the mass balance. It is observed that the percentage of missing carbon increases as the SIEM value increases. It is important to notice that on the walls of the reactor yellowish compounds are formed, especially at high values of SIEM which could indicate possible polymerizations in the reactor. In the literature is reported also that methane tends to polymerize in oxygen-poor conditions [45]. This is consistent with the results presented, since as previously discussed, at high energy values, the concentration of oxygen is low.

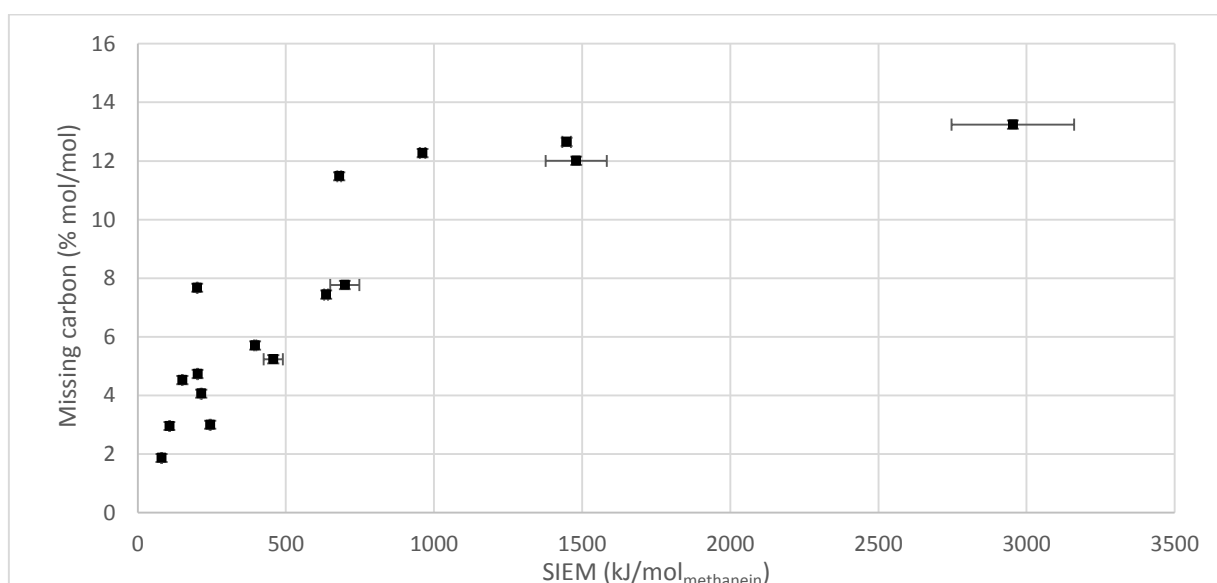


Figure 4.4. Percent of missing carbon as a function of SIEM at constant value of O_2/CH_4 ratio (0.5 v/v) and concentration of argon (0.375 v/v).

4.2. Methane to methanol in a plasma milli-reactor

The direct production of methanol from methane and oxygen being of particular interest, there is an interest to study its behavior in detail in order to optimize its production. In this part, the influences of flow rate, oxygen/methane ratio and argon concentration have been studied.

4.2.1. Influence of flow rate on methanol selectivity (ICCD)

In **figure 4.5** are showed the selectivity of methanol as a function of SIEM for different values of flow rate at constant O_2/CH_4 (0.5 v/v) ratio and argon concentration (0.375 v/v).

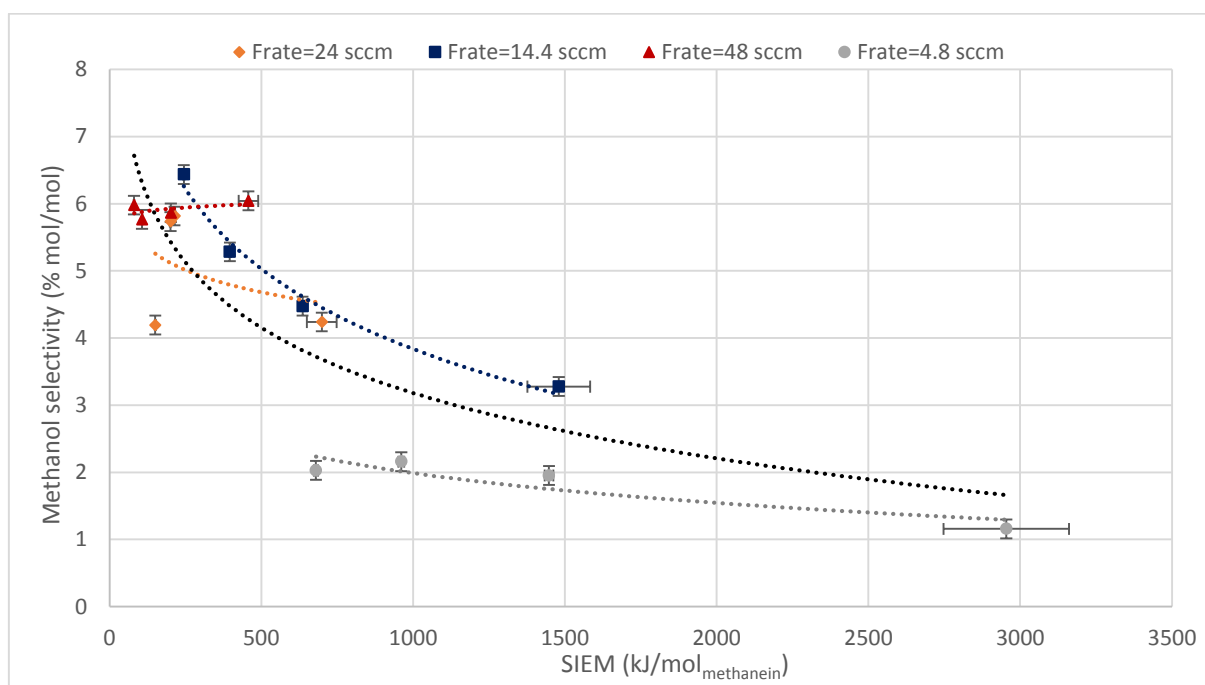


Figure 4.5. The methanol selectivity as a function of SIEM at different values of flow rate (4.8,14.4, 24, 48 sccm), constant value of O_2/CH_4 ratio (0.5 v/v) and concentration of argon (0.375 v/v).

It is observed that the selectivity of methanol decreases as the values of SIEM increase, the fastest decrease being observed at low values of SIEM. The results indicate also that at comparable SIEM values, higher values of selectivity are obtained with higher flow rate values (short residence times). For example, approximately at 1500 $kJ/mol_{methanein}$ the methanol selectivity increases from 2 to 3% when the flow rate increases from 4.8 to 14.4 mL/min.

In **figure 4.6a** is presented the H_2/CO ratio as a function of SIEM at different values of flow rate. It is observed that the H_2/CO ratio first decreases rapidly when the SIEM increases. There is no explanation for this behavior. At high values of SIEM ($> 500 \text{ kJ/mol}_{\text{methanein}}$), the ratio between H_2 selectivity and CO selectivity is almost constant at around 0.7. This is a typical value reported in the literature for syngas production [64], [65]. It is important to note that there is no significant influence of the flow rate on the H_2/CO ratio.

It is also reported the evolution of CO_2/CO ratio is also different according to the flow rate (see **figure 4.6b**). These differences were directly related with the differences in terms of discharge uniformity. It was proposed that the higher CO_2/CO ratios were obtained at the lowest gas flow rates because in these conditions, the discharge is highly non-uniform leading to an intense oxidation of methane. The differences observed in terms of methanol selectivity can be as well directly related with the differences in terms of discharge uniformity. Indeed, if the oxidation of methane is more intense in the portions of the gas receiving a lot of elementary micro-discharge, the selectivities of intermediate oxidation products such as methanol are logically lower. As a result, the non-uniformity of the discharge would be disadvantageous for the production of methanol. For this reason a flow of 48 sccm has been chosen for the next experiments.

In **figure 4.6b** the CO_2/CO ratio is presented as a function of SIEM at different values of flow rate. It is showed that the CO_2/CO ratio decreases when SIEM increases, and that this decrease is more rapid at high flow rate. This decrease is logical because CO is a primary oxidation product and is therefore produced before CO_2 could be formed by oxidation of CO. Also, it is observed that if the flow rate increases the CO_2/CO ratio decreases at comparable values of SIEM. In chapter 3, ICCD characterizations of the discharge indicated that the uniformity of discharge increased when the gas flow increased (**figure 3.13**).

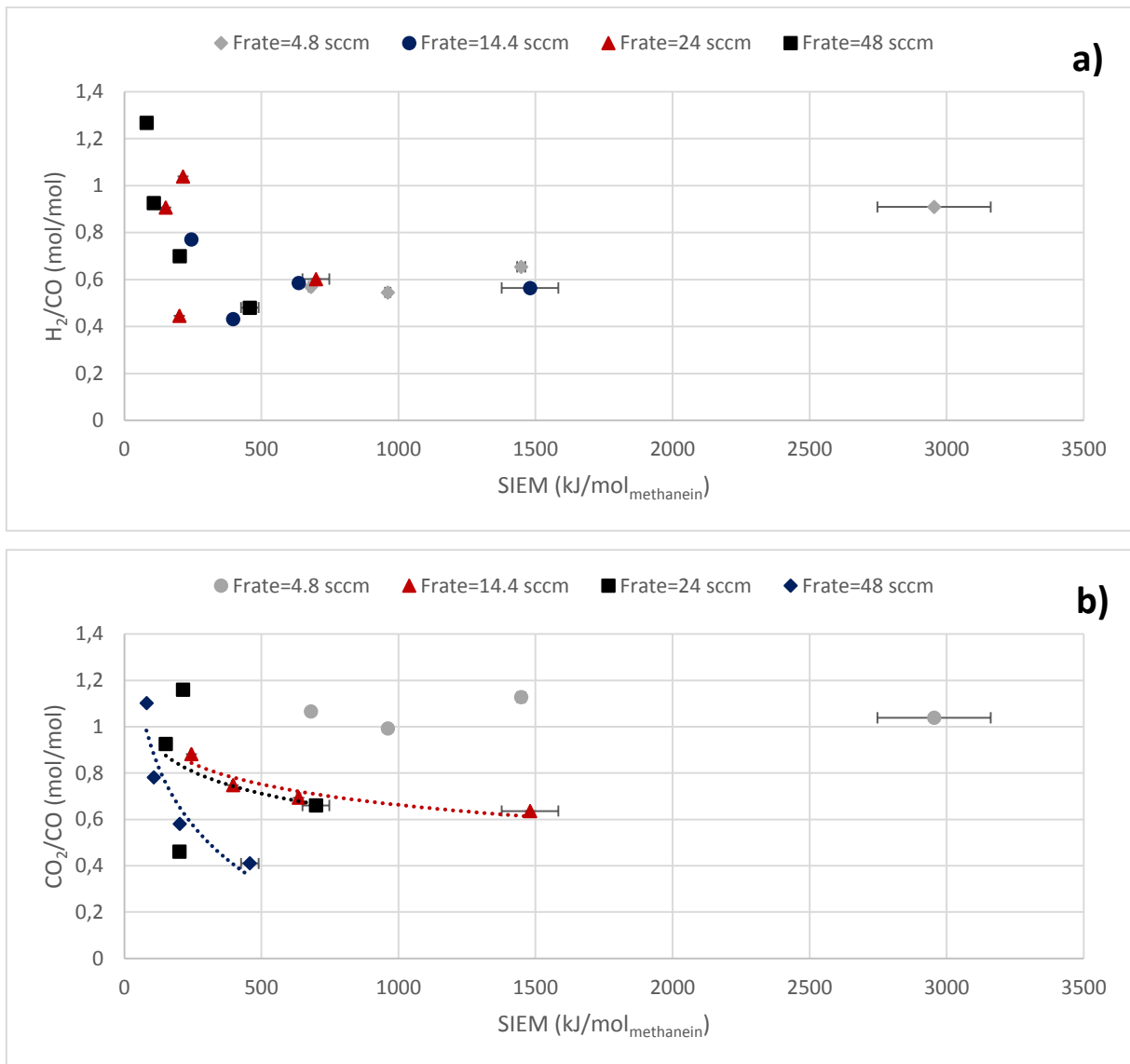


Figure 4.6. H₂/CO and CO₂/CO as a function of SIEM at different values of flow rate (4.8;14.4; 24; 48 sccm), constant value of O₂/CH₄ ratio (0.5 v/v) and concentration of argon (0.375 v/v).

On the other hand, a comparison between CO₂/CO and H₂/CO ratios as a function of methane conversion at low methane conversions (< 5%) using different experimental conditions is observed in **figure 4.7**.

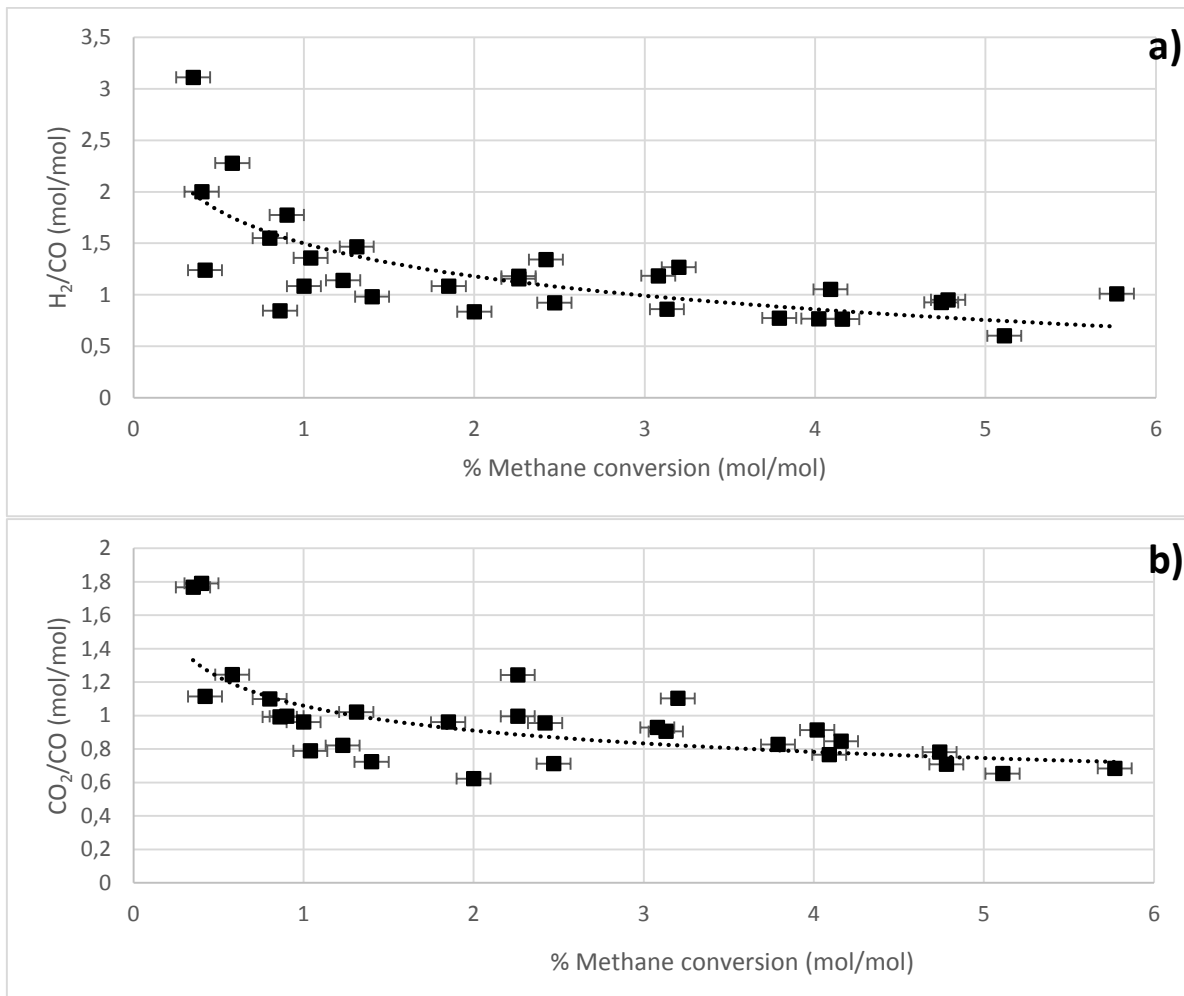


Figure 4.7. CO₂/CO ratio (a) and H₂/CO ratio (b) as a function of methane conversion at different conditions.

The **figure 4.7a** shows that the H₂/CO ratio decreases if methane conversion increases. It is also observed that in the first 2% of methane conversion the ratio decreases rapidly from 3.1 to 1 (n/n), at higher conversion values, the behavior of the ratio becomes almost constant around 1 (n/n), this behavior is typically reported in the literature at low methane conversion values [4], [65].

At the same time, we observed that the value of CO₂/CO ratio also decreases if the methane conversion increases (**figure 4.7 b**). In this case between 0 to 1 % of methane conversion the ratio decreases rapidly from 1.8 to 0.8 (n/n), at higher conversion values, and after the ratio becomes almost constant around 0.8 (n/n). This value is higher than we can find reported in the literature which oscillates around 0.15 (n/n) [46], [49], [65].

This variation in the CO₂/CO respect to the literature could be due to the hot spots

produced by the roughness of the reactor (details in chapter 3) studied in this thesis, which can present localized increments of temperature and favor combustion reactions, thus increasing the CO₂/CO ratio.

4.2.2. Influence of argon concentration on methanol selectivity

In recent investigations similar to ours, using inert gas (helium), sinusoidal signal for plasma activation and a millimeter-scale reactor design without catalyst, the team of [50] reported for a O₂/CH₄ ratio equal to 0.1 (v/v) a methanol selectivity equal to 27 % at a methane conversion of ≈6%. In the other hand the team of Nozaki et al. [45] reported methanol selectivities values up to 30% using a gaseous mixture without inert gas (composed only with O₂ and CH₄) with a ratio O₂/CH₄ equal to 0.5 (v/v) [45]. In general, the values of O₂/CH₄ used for the production of methanol reported in the literature oscillate between 0.1 and 0.5 for similar conditions to ours. To perform the study of the influence of argon an intermediate constant value of O₂/CH₄ ratio equal 0.3 (v/v) was therefore chosen.

[52] reported a maximum of methanol selectivity of 32% at argon concentration equal to 50:50 v/v (value respect to the source gas CH₄+O₂). The selectivity slightly increased from 25 to 32 % from 0 to 50:50 v/v of argon. Then the selectivity tends to decrease at higher concentration of argon.

Thus, the following experimental conditions of 0: 100, 50:50 and 60:40 v/v (values respect to the source gas) were chosen. These values correspond to an argon concentration of 0, 0.3, and 0.375 v/v respect to the total reactive gas mixture (CH₄+O₂+Ar).

In **figure 4.8** are presented the methane conversion (a) and methanol selectivity (b) as a function of SIEM and methanol selectivity (c) as a function of methane conversion at different values of argon concentrations (0, 0.3, 0.375 v/v), with constant O₂/CH₄ ratio (0.3 v/v) and flow rate (48 sccm).

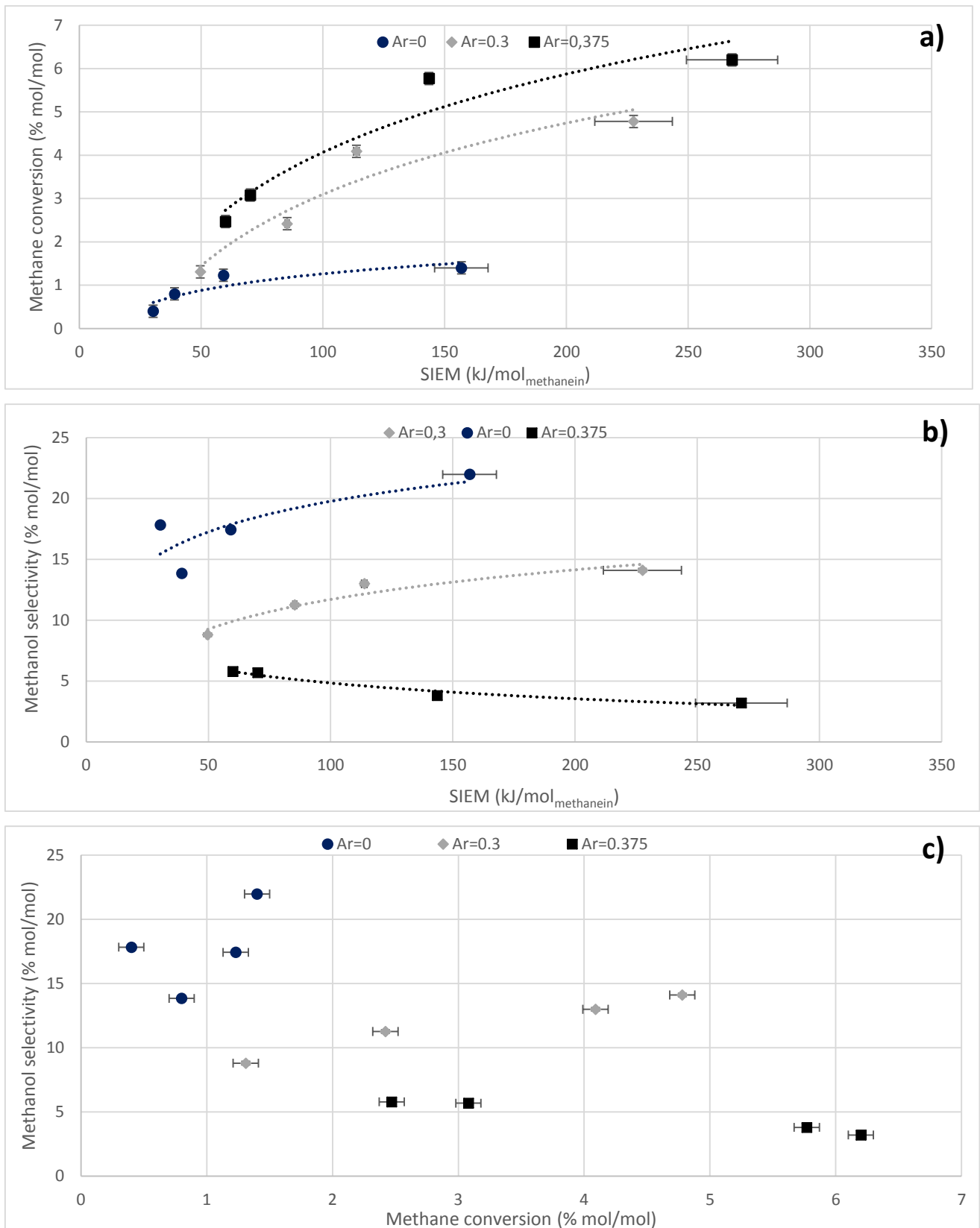


Figure 4.8. Percent of methane conversion (a) and methanol selectivity (b) as a function of SIEM and methanol selectivity in function of methane conversion (c) at different values of argon's concentration (0,0.3,0.375 v/v), constant value of flow rate (48 sccm) and O₂/CH₄ ratio (0.3 v/v).

It is observed, if we analyze the results of methane conversion as a function of argon concentration that the conversion increases if the argon concentration increases. For example, at 0.375 v/v of argon the methane conversion is equal to 5.8% at around 150 $\text{kJ/mol}_{\text{methane in}}$, which represents a delta of 4.3 units of methane conversion in comparison with the condition reported without argon (**figure 4.8a**).

To explain this result, it is noted that Ar gas molecules may function as an energy transferring medium in the discharge zone. Ar molecules are able to receive the plasma electric field energy easier than CH_4 molecules, leading to higher probability of collisions between Ar molecules and energetic electrons to transform Ar to its metastable state of Ar^* [52], [66]. As a consequence, more Ar gas molecules in the discharge zone bring about higher possibility of collisions between these activated Ar molecules (Ar^*) and CH_4 gas molecules, which causes higher CH_4 conversion.

In **figure 4.8b** it is also observed that methanol selectivity decreases if the concentration of argon increases at a constant value of SIEM. This may be caused by the increase in methane conversion when the argon concentration increases, as described before.

In order to better understand the argon's influence in methanol selectivity in **figure 4.8c** is showed the methanol selectivity in function of methane conversion at different values of argon concentration. Due to the low range of SIEM and low conversions associated, it is difficult to distinguish a clear behavior of methanol selectivity as a function of methane conversion at different conditions of argon concentrations.

Anyway, it is possible to observe that the highest values of methanol selectivity are associated to the lowest values of argon concentration: the methanol selectivity decreases from 17 to 5 % when the argon concentration increases from 0 to 0.375 v/v at 60 $\text{kJ/mol}_{\text{methane in}}$. Fast reactions between Ar^* and methanol leading to the destruction of methanol could maybe explain this result. This is however an opposite trend compared to the study of Okumoto et al. [46] who reported that the methanol selectivity increased from 25 to 32 % from 0 to 50:50 v/v of argon.

The different behaviors between the system studied in this thesis and the one reported by Okumoto may be due to the different nature of the electric applied voltages: pulsed

voltage in the case of Okumoto and sinusoidal voltage in this thesis. Indeed, this difference could lead to a change in the nature and concentration of the active species produced in the plasma.

4.2.3. Influence of the O₂/CH₄ ratio on methanol selectivity

In order to study the influence of O₂/CH₄ ratio in methane conversion and methanol selectivity, in **figure 4.9** is reported the behavior of methane conversion (**4.9a**) and methanol selectivity (**4.9b**) as a function of SIEM and methanol selectivity in function of methane conversion (**4.9c**) at different values of O₂/CH₄ ratio (0.14, 0.3, 0.5, 0.76, 1 v/v) without argon.

In figure **4.9a** is observed that methane conversion increases if O₂/CH₄ ratio increases at comparable values of SIEM. Possibly because with higher concentrations of oxygen, there is a larger production of highly reactive species (O*, O1D) as is described in Zhou et al. (1997) [47] which could promote methane degradation.



In **figure 4.9b** it is possible to observe that the selectivity of methanol presents a tendency to increase if we decrease the ratio O₂/CH₄. For example, at 60 kJ/mol_{methane} in the methanol selectivities are 5, 17 and 22% for O₂/CH₄ ratios of 1, 0.3 and 0.14 respectively. However, this trend may be due only to the decrease of methane conversion when the O₂/CH₄ ratio decreases. Indeed, in **figure 4.9c** it can be observed that experiments performed at low O₂/CH₄ ratios gave lower conversions. Nevertheless, it can be observed on the **figure 4.9c** that at comparable methane conversion the highest values of methanol selectivity are reported at low O₂/CH₄ values. For example, at 1% of methane conversion the methanol selectivity increases from 13 to 25% when the O₂/CH₄ ratio decreases from 0.5 to 0.14. And at an intermediate O₂/CH₄ ratio of 0.3 the methanol selectivity is between 13 and 25% with a value of 17%.

According to Bie et al. [4], the main reactions responsible of the formation of CH₃OH, in similar conditions of O₂/CH₄ ratio and SIEM than those used in this study, are:



Nozaki et al. [65] reported that the CH_3O radical is mainly formed by the recombination of CH_3O_2 radical:



O_2 is needed to produce CH_3O_2 by the reaction between CH_3 and O_2 . However, if the concentration of O_2 is too high, it will favor the further dehydrogenation of CH_3O by the following reaction:



To conclude, the analysis of the main pathways responsible for methanol formation shows that a too high concentration of O_2 is not favorable for the selectivity of methanol, in accordance with what is observed experimentally.

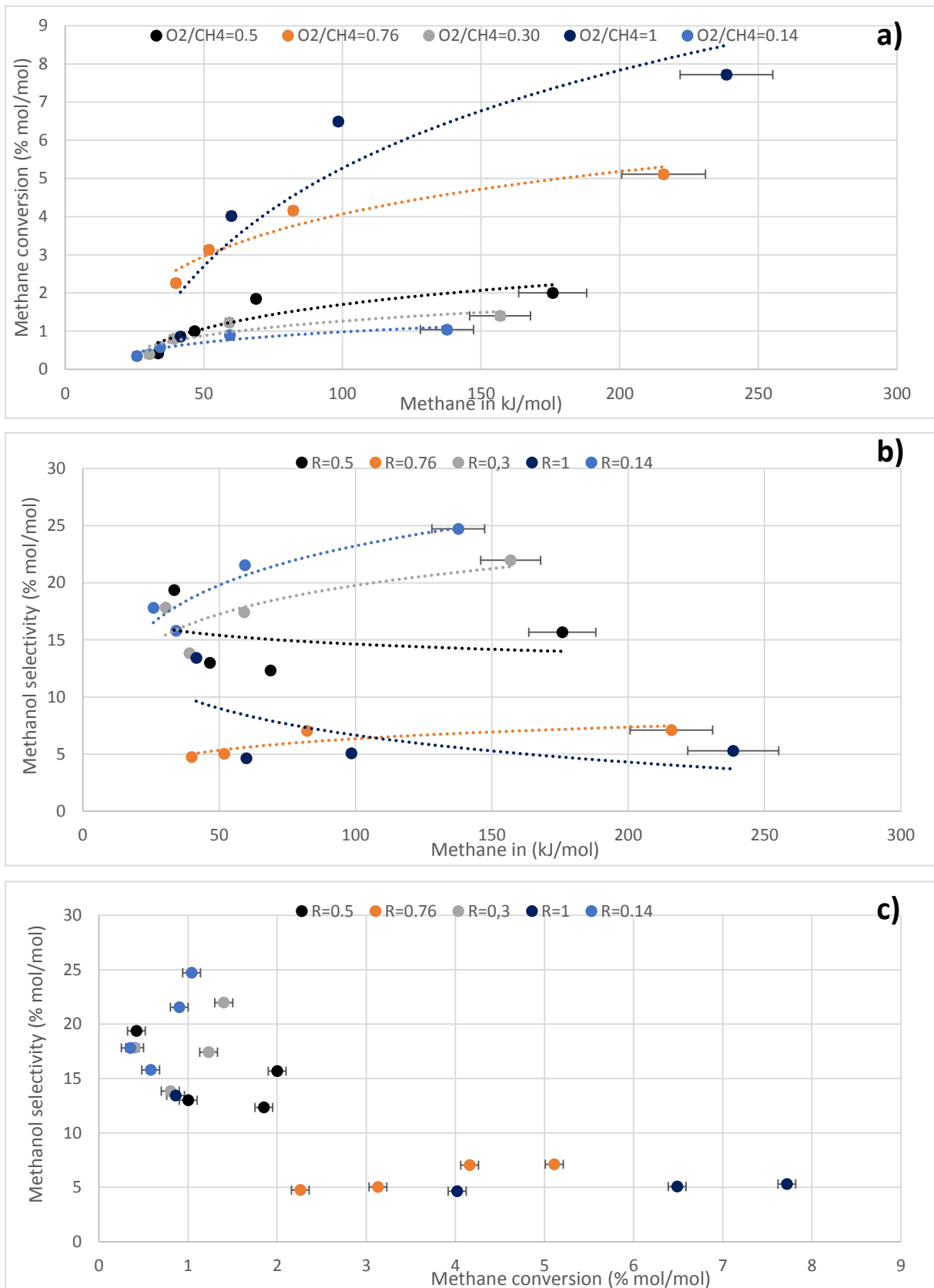


Figure 4.9. Methane conversion (a) and methanol selectivity (b) as a function of SIEM; methanol selectivity as a function of methane conversion (c) at different values of O₂/CH₄ ratio (0.14, 0.3, 0.5, 0.76, 1 v/v) and constant value of flow rate (48 sccm) without presence of argon.

4.3. Conclusion

In this chapter the general chemical behavior of the plasma millireactor is shown and discussed.

Methane conversions of up to 30% are obtained, obtaining as a main compounds of reaction syngas (CO and H₂), propane, ethylene, methanol and CO₂. It was found that the selectivity of methanol is favored at low values of energy injected in the system and in general its value increases if the volumetric flow increases possibly because the augmentation of the volumetric flow favors the uniformity of discharge and therefore the distribution of energy.

The increase of the argon concentration in the system was shown to have an unfavorable influence on the selectivity of methanol, possibly due to the increase in the concentration of intermediate species such as Ar * which could react directly with the methanol molecules.

On the other hand, with respect to the O₂/CH₄ ratio, the increase in the values of this ratio implies a decrease in methanol selectivity, possibly due to the fact that when oxygen is in too high concentration, the CH₃O radical which is a crucial intermediate species for methanol synthesis may be rapidly dehydrogenated.

The experimental study raises the need for a theoretical study that allows a better understanding of the influence of operating parameters on the production of methanol by partial oxidation of methane in a DBD plasma millireactor. This with the aim of increasing the selectivity of methanol.

For the accomplishment of this study we selected the simulation tool COMSOL Multiphysics 5.1. The presentation and discussion of these results are presented in chapter 5 of this thesis.

Chapter 5 : Simulation of a DBD plasma milli-reactor for POM

5.1. Introduction to the simulation of a DBD plasma milli-reactor

The objective of the simulation is to understand the different chemical and physical processes taking place in the plasma millireactor and determine the conditions required to increase the selectivity of methanol. The simulations were achieved with the use of COMSOL Multiphysics 5.1.

5.2. Description of the filamentary aspect of DBD plasma

As the polarity of the electrodes is rapidly changing, the microdischarges are reformed at the point where the breakdown voltage is reached in the next half cycle of the AC voltage sine wave. This results in the continuous formation of nanosecond microdischarges at a frequency which is twice that of the applied frequency [34]. The microdischarges appear as “spikes” on the current waveform. In appearance, the microdischarges are randomly distributed over the surface of the dielectric. In reality, the position of the microdischarge formation is dependent on the residual charge distribution on the dielectric surface [1], [41] .

In these microdischarges a large fraction of the electron energy is used for excitation, dissociation, and ionization of the molecules and therefore to initiate the chemical reactions. At the point where the breakdown voltage is reached, the current flow will increase sharply due to an intensive avalanche of electrons in the discharge gap between the electrodes. These high-energy electrons will collide with gas molecules leading to the formation of new “active” plasma species including excited molecules and atoms and their relevant degrees of freedom, radicals, ions and new stable gas molecules as showed in **table 1.3** in chapter 1.

This is the reason why modelling these microdischarges is of prime importance for a realistic description of the reaction chemistry. Therefore, an extensive study of the reaction chemistry considering above reactions and a detailed radical scheme is carried out while mimicking the filamentary discharge regime. More specifically, the plasma chemistry in one microdischarge pulse, in a time scale of 1-10 ns and its afterglow is investigated, which corresponds to one filament in a DBD [29].

5.3. The DBD plasma modelling

In recent years, computer modeling has and will continue to benefit the investigation of DBD plasmas, particularly in areas such as plasma reactor optimization [67]. To investigate the DBD plasmas and the use of DBD plasmas in technological devices, three basic approaches are usually employed: fluid-hydrodynamic model, kinetic model or particle-in-cell/Monte Carlo collision (PIC/MCC) model and hybrid models [67]–[69].

Fluid models have been developed both for low and high pressure discharges. Natalia *et al.* [68] reported a multi-fluid hydrodynamics simulation to investigate the ion energy and angular distributions incident on dielectric flat surfaces resulting from the intersection of DBD filaments sustained in atmospheric pressure air. The Fluid approximation describes the plasma in terms of macroscopic quantities by taking velocity moments of the Boltzmann equation. This results in a set of coupled partial differential equations that can be solved using the finite element method. The commercial product Comsol Multiphysics Plasma Module uses the fluid approximation. Advantages of the fluid approximation are that it is efficient to solve the resulting equations and straightforward to define arbitrarily complex plasma chemistries. It is also easy to couple the electron dynamics to the electromagnetic fields, which are also computed using the finite element method.

The method particle in cell and Monte Carlo collision (PIC/MCC) provides the most detailed information on the properties e.g., velocity distributions of the electrons, ions and atoms [70]. The Kinetic approach solves for the distribution function for the ions and electrons in a plasma by solving either the Boltzmann equation or an approximation, like the Fokker-Planck equation. The distribution function can also be computed using a Lagrangian approach, where ordinary differential equations are solved for the electron position and velocity, as is the case of a particle in cell (PIC) codes. The advantage of this approach is that it allows for the electron energy distribution function to take an arbitrary shape in energy space and can also show effects that are not captured by fluid models. Drawbacks include difficulties associated with implementing arbitrary plasma chemistries and high computational cost.

Hybrid methods treat some of the components of a plasma as a fluid and others kinetically. Usually, the electrons are treated kinetically by solving the Fokker-Planck equation or using a Monte Carlo method, and the ions and other radical species are computed using a fluid model. In this sense, hybrid methods offer a compromise between the fidelity of kinetic models and the speed and convenience of fluid models. Hybrid models have been developed to do practical simulations without losing non-equilibrium properties such as ionization and dissociation rates. Kushner [67] proposed a hybrid model to address different physical processes or address the same physical processes using different techniques.

5.3.1. Governing equations

Electrons are energy providers for many plasma-chemical processes. The rates of such processes depend on the number of electrons having sufficient energy to do the job. This can be described by means of the electron energy distribution function (EEDF), which is the probability density for an electron to have the energy " ϵ ". Quite often this distribution function strongly depends on the electric field and gas composition, and can vary far from equilibrium. The evolution of the electron energy distribution function is considered as an approach to describe the electron diffusion and drift in the space of electron energy.

As a consequence, free electrons and heavy species transport equations, plasma chemistry including volumetric and surface reactions are simultaneously solved with Poisson's equation. The proposed model makes it possible to study the structure of the homogeneous barrier discharges in detail. In particular, the spatial-temporal distributions of electric field and densities of charged particles are obtained. Such analyses help us to better understand processes enabling a discharge (or streamer) generation and propagation in a DBD system.

5.3.2. Electron transport equations

In general, electron transport can be described by the Boltzmann equation. This kinetic equation describes the statistical behavior of a thermodynamic system that is not in thermodynamic equilibrium. This equation can also be used to determine how physical quantities change, such as heat and momentum energy. The Boltzmann equation is an extremely complicated integral-differential equation and solving it in an efficient

manner is not currently possible.

The plasma produced in a DBD is characterized by high pressure and non-equilibrium conditions. These conditions allow the system modeler to adopt two approximations which will further simplify the problem of solving the moment equations. Solutions based on these approximations have been validated against the solutions obtained from the exact solution of the moments of the Boltzmann equation system [67], [68]. These approximations are:

1. A single-moment (fluid model) description using the continuity equations for the various particle densities is satisfactory at atmospheric pressures. At such high pressures, the momentum and energy of the different particles reach equilibrium in relatively short times compared to the variations in the electric field due to space charge buildup [1], [71].

2. Local field approximations are assumed (which is a direct consequence of the above assumption), i.e. gas properties such as drift velocities and the collisional ionization coefficient α are functions only of E/n .

This reduces the governing equations to a three-dimensional, time-dependent problem. The fluid equations describe the electron number density, the mean electron momentum and the mean electron energy as a function of configuration space and time. The rate of change of the free electron density in the gap is described by the “continuity equation” which is given by [72]

$$\frac{\partial n_e}{\partial t} + \nabla \cdot (-\mu_e E n_e - \nabla(D_e n_e)) = S_e \quad \text{Eq. 5.1}$$

where n_e (m^{-3}) is the electrons number density, μ_e ($\text{m}^2 \cdot \text{V}^{-1} \cdot \text{s}^{-1}$) and D_e ($\text{m}^2 \cdot \text{s}^{-1}$) are the mobility and diffusion coefficient, E ($\text{V} \cdot \text{m}^{-1}$) is the electric field and S_e ($\text{m}^{-3} \cdot \text{s}^{-1}$) is the net electron source term. A detailed expression of S_e is given in chemical kinetics and source term treatment subsection later.

Similar to the continuity equation, the energy conservation equation is given by [72]

$$\frac{\partial n_\epsilon}{\partial t} + \nabla \cdot (-\mu_\epsilon E n_\epsilon - \nabla(D_\epsilon n_\epsilon)) + E \cdot (-\mu_e E n_e - \nabla(D_e n_e)) = S_\epsilon \quad \text{Eq. 5.2}$$

where n_ϵ ($\text{V} \cdot \text{m}^{-3}$) is the energy density, μ_ϵ ($\text{m}^2 \cdot \text{V}^{-1} \cdot \text{s}^{-1}$) and D_ϵ ($\text{m}^2 \cdot \text{s}^{-1}$) are the energy

mobility and diffusion coefficient and S_ε ($\text{V}\cdot\text{m}^{-3}\cdot\text{s}^{-1}$) is the total energy transfer due to collisions.

The electron diffusivity, energy mobility and energy diffusivity are calculated using Einstein's relation for a Maxwellian EEDF:

$$D_e = \mu_e T_e ; \mu_\varepsilon = \frac{5}{3} \mu_e ; D_\varepsilon = \mu_\varepsilon T_e \quad \text{Eq. 5.3}$$

where T_e (V) denotes electron temperature.

5.3.3. Diffusive transport equations for heavy species

Ground state atoms, excited species and ions, named here heavy species, in plasma require a suitable transport equation. Assume a reacting flow consists of $k = 1, \dots, K$ species and $j = 1, \dots, Q$ reactions. The equation for the first $K - 1$ species is given by [73]

$$\rho \frac{\partial Y_k}{\partial t} + \rho (\mathbf{V} \cdot \nabla) Y_k = \nabla \cdot \mathbf{j}_k + R_k \quad \text{Eq. 5.4}$$

where \mathbf{j}_k is the multicomponent species flux, R_k is the rate expression for species, \mathbf{V} is the mass averaged fluid velocity vector, ρ represents the density of the mixture and Y_k is the mass fraction of species k . The mass average velocity \mathbf{V} is defined as:

$$\mathbf{V} = \frac{1}{\rho} \sum_{k=1}^K \rho_k \tilde{\mathbf{V}}_k = \sum_{k=1}^K Y_k \tilde{\mathbf{V}}_k \quad \text{Eq. 5.5}$$

$\tilde{\mathbf{V}}_k$ is the average velocity of species k at a given location in the fluid relative to the fixed laboratory frame of reference. This is not the velocity of individual species k but the average value over all species k atoms at this location in the fluid, ρ_k is the mass density of species k , and the mass fraction of species k is $Y_k = \rho_k / \rho$.

The diffusive flux vector, \mathbf{j}_k , is defined as:

$$\mathbf{j}_k = \rho_k (\tilde{\mathbf{V}}_k - \mathbf{V}) = \rho Y_k \mathbf{V}_k \quad \text{Eq. 5.6}$$

\mathbf{V}_k denotes the multicomponent diffusion velocity for species k and is given by [73], [74]:

$$\mathbf{V}_k = \sum_{j=1}^Q \tilde{\mathbf{D}}_{kj} \mathbf{d}_k - \frac{D_k^T}{\rho Y_k} \nabla \ln T \quad \text{Eq. 5.7}$$

$\tilde{\mathbf{D}}_{kj}$ are the Multicomponent Maxwell-Stefan diffusivities, T is the gas temperature, D_k^T ($\text{kg}\cdot\text{m}^{-1}\cdot\text{s}^{-1}$) is the thermal diffusion coefficient and \mathbf{d}_k is the diffusion driving force which, for a low-density ideal gas, is given by [73], [74]:

$$\mathbf{d}_k = \frac{1}{cRT} \left[\nabla p_k - Y_k \nabla p - \rho_k \mathbf{g}_k + Y_k \sum_{j=1}^Q \rho_j \mathbf{g}_j \right] \quad \text{Eq. 5.8}$$

where c is the molar concentration, R is the universal gas constant, p is the total pressure, p_k is the partial pressure of species k , and \mathbf{g}_k is an external force per unit mass acting on species k . When this force is due to electric field, it is written as:

$$\mathbf{g}_k = \frac{Z_k F}{M_k} \mathbf{E} \quad \text{Eq. 5.9}$$

Z_k is the charge number of species k , F is Faraday's constant, M_k is the molecular weight of species k and E is the electric field. Using the ideal gas law, $p = cRT$ and the fact that $p_k = x_k p$ where x_k is the mole fraction of species k and can be expressed with the equation: $x_k = Y_k M/M_k$ where M is the mole averaged molecular weight. Then, the diffusion driving force \mathbf{d}_k can be re-written by the equation:

$$\mathbf{d}_k = \nabla x_k + \frac{1}{p} \left[(x_k - Y_k) \nabla p - \rho_k \mathbf{g}_k + Y_k \sum_{j=1}^Q \rho_j \mathbf{g}_j \right] \quad \text{Eq. 5.10}$$

Simulation study here considers isothermal and isobaric conditions in the gap (i.e. $\nabla T = \nabla p = 0$). This leads to remove the second term on the right side of equation (Eq.5.7) and in Equation (Eq.5.10). Thus, the multicomponent diffusion velocity for species k , \mathbf{V}_k , is expressed as a function of the dominant terms: the gradient of the mole fraction, ∇x_k , and the migration force \mathbf{g}_k applied on ionic species in the electric field E .

5.3.4. Poisson's equations and surfaces boundary conditions for DBD plasma

Since the model is applied to DBD, the effect of the dielectrics covering the electrodes needs to be taken into account. The electric fields across the gap, dielectric coatings and barrier are calculated using Poisson's equation [73]:

$$-\nabla \cdot \epsilon_0 \epsilon_r \nabla V = \rho_v \quad \text{Eq. 5.11}$$

ρ_v is the space charge density and is defined by the equation:

$$\rho_v = q \left(\sum_{k=1}^N Z_k n_k - n_e \right) \quad \text{Eq. 5.12}$$

where q is the elementary charge and n_k is the ion number density for the species k . whereas ϵ_0 (F/m) is the permittivity of free space and ϵ_r is the relative permittivity (dimensionless).

The constitutive relation that describes the macroscopic properties of the dielectric coatings and barrier medium (relating the electric displacement, D , with the electric field, E) and the applicable material properties is given as:

$$\mathbf{D} = \epsilon_0 \epsilon_r \mathbf{E} \quad \text{Eq. 5.13}$$

With this definition, the influence of charge accumulation on the dielectric materials, which is described by Gauss's law, can be written as:

$$\mathbf{n}_{s1} \cdot (\mathbf{D}_1 - \mathbf{D}_2) = \rho_s \quad \text{Eq. 5.14}$$

Where 1 and 2 refer to the two sides of the boundary, \mathbf{n}_{s1} is the unit normal vector pointing outward medium 1 (adjacent to the gap) and ρ_s is the surface charge density. As on dielectric surfaces, charge accumulates due to the difference in fluxes between the electrons and ions, ρ_s is defined as the solution of the following distributed-ODE on the boundary:

$$\frac{d\rho_s}{dt} = \mathbf{n}_s \cdot \mathbf{J}_i + \mathbf{n}_s \cdot \mathbf{j}_e \quad \text{Eq. 5.15}$$

where \mathbf{J}_i and \mathbf{j}_e are the total ion current density and the total electron current density respectively on the wall and \mathbf{n}_s is the unit normal vector to the wall.

In DBD model, electrons are lost to the wall due to random motion within a few mean free paths of the wall and gained due to secondary emission effects, this is vital in sustaining discharges. This is introduced in the boundary conditions by describing the secondary emission flux for electrons with the following equation:

$$\mathbf{n}_s \cdot \Gamma_{e,s} = \sum_{k=1}^N \gamma_k (\Gamma_k \cdot \mathbf{n}_s) \quad \text{Eq. 5.16}$$

where γ_k the secondary electron emission coefficient for ionic species colliding with the surface (reported in annex 2).

Additionally, the secondary emission energy flux requires that the mean energy of the secondary electrons should be specified:

$$\mathbf{n}_s \cdot \Gamma_{\epsilon,s} = \sum_{k=1}^N \gamma_k \bar{\epsilon}_k (\Gamma_k \cdot \mathbf{n}_s) \quad \text{Eq. 5.17}$$

The mean electron energy of the emitted electrons, $\bar{\epsilon}_k$ is typically a function of the ionization energy of the impinging ion and the work function of the surface:

$$\bar{\epsilon}_k = \Delta\epsilon_k - 2W_s \quad \text{Eq. 5.18}$$

These equations are then solved iteratively by the so-called modified strongly implicit method in time and in space until convergence is reached. A later section will illustrate 1D model building procedure using DC discharge plasma module of COMSOL Multiphysics (5.1) in order to simulate Ar/CH₄/O₂ mixture time-based evolution present

in “filament geometry”. This is done by considering all above phenomena and presented equations. The choice of initial values will be also described.

5.3.5. Chemical kinetics and source term treatment

The developed model here is for a dielectric barrier discharge (DBD) in one-sided planar reactor, used for the conversion of CH₄ into value-added chemicals, by the partial oxidation with O₂ in the presence of argon. To describe the chemistry of Ar/CH₄/O₂ mixture as the gas filled in the gap, 56 different species (including molecules, radicals, ions, and electrons) are considered in the model, as outlined in **table (5.1)**:

Table 5.1. List of species included in the model for the Ar/CH₄/O₂ gas mixture.

Molecules	Radicals	Charged Species	Excited species
CH ₄ C ₂ H ₆ , C ₂ H ₄ , C ₂ H ₂ C ₃ H ₈ , C	CH ₃ , CH ₂ , CH, C ₂ H ₅ , C ₂ H ₃ ,	CH ₄ ⁺ , CH ₃ ⁺ , CH ₂ ⁺ , CH ₂ ⁻ , CH ⁺ , C ₂ H ₆ ⁺ , C ₂ H ₆ ⁻ , C ₂ H ₄ ⁺	CH ₄ [*] , C ₂ H ₆ [*] , C ₂ H ₄ [*] C ₃ H ₈ [*]
H ₂ H ₂ O, H ₂ O ₂	H, OH, HO ₂	H ₂ ⁺ , H ⁺ , H ⁻ , H ₂ O ⁺ , OH ⁻ ,	
O ₂	O	O ₂ ⁺ , O ⁻	O ₂ a1d, O ₂ b1s, O1d
CO, CO ₂		CO ₂ ⁺ , CO ⁺	CO ₂ [*] , CO [*]
CH ₃ OH, CH ₂ O	CH ₃ O ₂ , CH ₃ O, HCO,		
Ar	Ar	Ar ⁺	Ar [*]

The source term S_e (m⁻³.s⁻¹) present in equation 5.1, is calculated by considering the different reaction mechanisms describing the kinetic processes in the plasma. Reactions mechanisms and related data describing energies of collisions and cross-sections of different electron-neutral collisions, electron-ion reactions are taken mainly from Bolsig+ database LXcat.

Suppose that there are M reactions which contribute to the growth or decay of electron density and P inelastic electron-neutral collisions (in general $P \gg M$). In the case of *rate coefficients*, the electron source term is given by:

$$S_e = \sum_{j=1}^M x_j k_j N_n n_e \quad \text{Eq. 5.19}$$

where x_j is the mole fraction of the target species for reaction j , k_j is the rate coefficient for reaction j (SI unit: m^3/s) and N_n is the total neutral number density (SI unit: $1/\text{m}^3$). n_e is the electron energy density (SI unit: V/m^3).

Knowing the cross-section values of electron-neutral collision process j , σ_j (m^2) as a function of electron energy value ε (eV), then rate coefficient of the reaction j k_j can be expressed using cross section data as a highly nonlinear function of the mean electron energy and can be calculated by the equation:

$$k_j = \gamma \int_0^{\infty} \varepsilon \sigma_j(\varepsilon) f(\varepsilon) d\varepsilon \quad \text{Eq. 5.20}$$

$f(\varepsilon)$: ($\text{eV}^{-3/2}$): Is the electron distribution function, and can be approximated to the zeroth-order term $f_0 \cdot \gamma$ ($\text{C}^{1/2}\text{kg}^{-1/2}$): Constant coefficient = $(2e/m_e)^{1/2}$

In a similar way, electron mobility, energy loss, ionization frequency are defined as parameters dependent on the electron energy. These dependencies are integrated in Comsol Multiphysics Plasma Module.

5.4. Introduction to numerical simulation (plasma module COMSOL Multiphysics 5.1) and description of the different modeling approaches

The software Comsol Multiphysics 5.1 was chosen because it is an intuitive management software based on the finite element method. In addition to the incorporation of the Plasma module which contains the set of equations described in section 5.2 for the prediction of DBD plasmas. The Plasma module incorporates a database referring to the values of input variables such as cross section for different gases as an example.

The logical criterion of Comsol to solve a given model as a function of time is divided into 5 main steps:

- Geometry description
- Declaration of values borders
- Declaration of domain values
- Mesh type and fineness
- Temporal scale of solution

The criteria used in the previous steps are very important for the determination of the simulation time of the model.

In **Figure 5.1** it is possible to observe the general scheme used to perform the simulation of the DBD plasma milli-reactor. The plasma discharge was considered spatially uniform in x and y directions, what is an important approximation of the reality because as already said, a DBD operating in a Ar/CH₄/O₂ mixture is not spatially homogeneous (**Figure 5.1a**). However, the actual simulation tools are not powerful enough to predict the spatial distribution of micro-discharges in a DBD discharge. However, the discharge was not supposed uniform in the axe z, as a 1D geometry described in **figure 5.1 b** was used in the model.

Finally, the flow of the gas in the plasma millireactor was supposed to be “plug-flow like” meaning that the gas flows as elementary slices which do not mix (no mass transfer between them). As a result, time-dependent simulations are carried out to predict the temporal evolution of species in a given slice of gas.

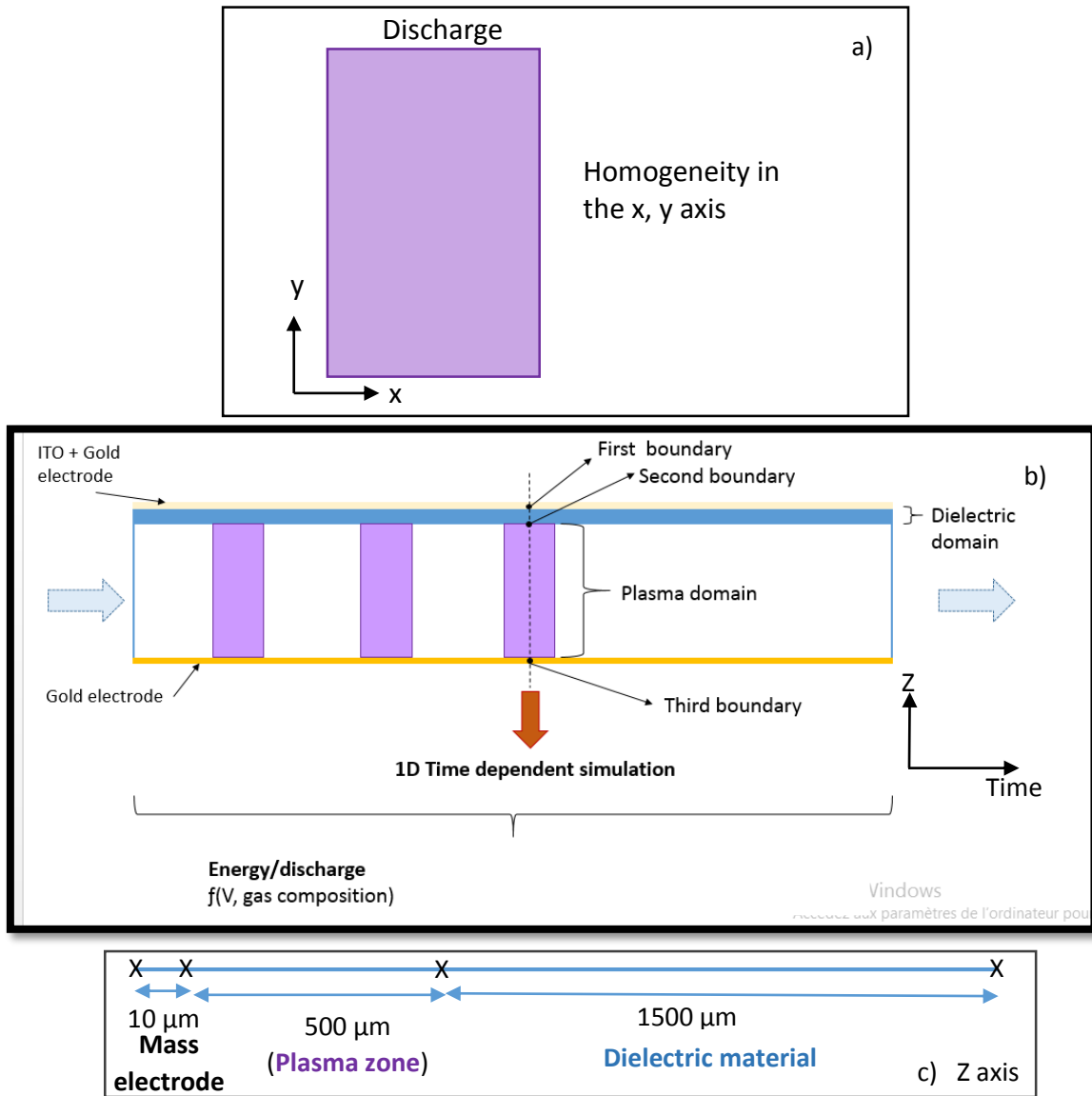


Figure 5.1. Graphical description of 1D DBD plasma model.

5.4.1. Sinusoidal model

In the case of the sinusoidal DBD numerical simulation, COMSOL Multiphysics 5.1 Plasma module solving simultaneously the electron impact reactions set and an optimized radical reactions scheme was employed. The voltage applied in the DBD model was the real sinusoidal one. Voltage was defined as a $V(t) = V_{\max} \cdot \sin(2\pi \cdot \text{freq} \cdot t)$, where "freq" is the signal frequency.

This mode of calculations allowed to mimic the successive formation of filamentary discharges and to characterize the plasma chemistry evolution for a given starting mixture of Ar/CH₄/O₂ when a sinusoidal electrical regime is applied to the studied

reactor. Indeed, the model is able to describe the successive formation and propagation of streamers during several periods (1 ms – 100 ms) as a function of applied voltage amplitude (10 – 18 kV pp) and its frequency (3 – 6 kHz). Results permit the evaluation of electron energy spatially and temporally and to evaluate its impact on the gas chemistry when electron impact and radical mechanisms are combined. In this model, the transport of neutral species in the slice of gas is done only by diffusion.

5.4.2. Multi-time scale model

In the case of the multi-timescale model, another approach was used. Two models were used: using the plasma module, a DBD model was first used to determine the concentrations of radicals produced by a single microdischarge. Then a simple 0D model solving the conservation equations for neutral species was used to calculate the time evolution of the neutral species. In this 0D model, the periodic production of radical species due to the periodic occurrence of micro-discharges in the reactor was defined basing on the results of a one micro-discharge DBD model supposing that a micro-discharge occurs every 0.17 ms (corresponding to a half period of the true applied sinusoidal voltage) and that the micro-discharge lasted 0.16 ns (**figure 5.2**). As a result the requirements of equipment and time are expected to be greatly diminished compared to the sinusoidal DBD model. It is important to notice that the real number of micro-discharge per period and the real voltage at which the micro-discharge occurs are not known.

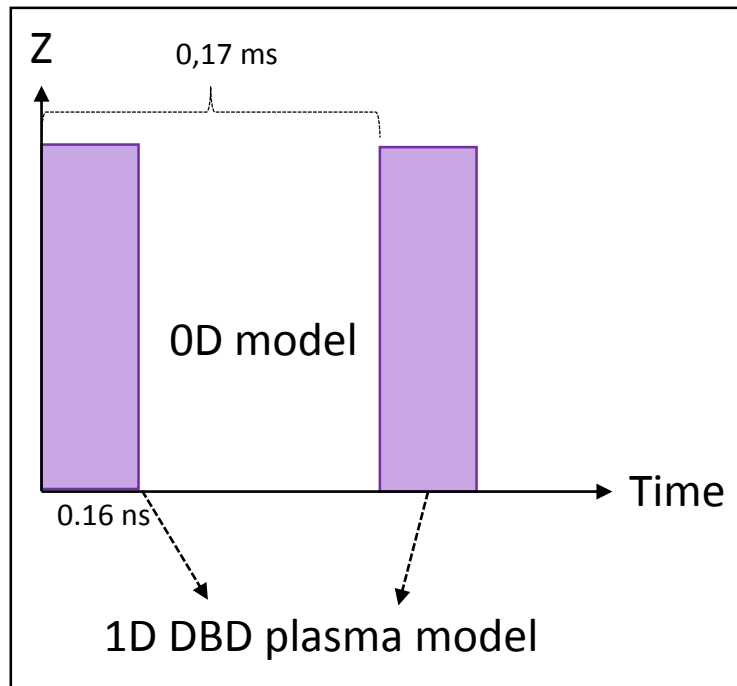


Figure 5.2. Graphical description of 0D and 1D DBD plasma model.

It has to be noted that in our simplified multi-timescale approach, the DBD model is used only once with the initial concentrations of species (concentrations at the inlet of the reactor). A more rigorous methodology would have consisted in calculating the production of radical species produced by one microdischarge at different residence times to take into account the evolution of the composition of the gaseous mixture. Such a rigorous methodology for POM plasma simulation was already reported by Goujard et al. [75]

5.4.2.1. DBD model for the simulation of one microdischarge

The single micro-discharge was first simulated using the 1D DBD plasma model by applying a constant voltage. The constant voltage value was fixed at 10.8 and 15 kV pp because the experimental data was reported for those tensions. The duration of the temporal simulation was 2 nanoseconds (**figure 5.3a**) because the micro-discharge could be considered terminated after 0.16 ns (negligible concentration of electrons, negligible instantaneous power and stabilized concentrations of radicals). The **figure 5.3** shows the evolution of the instantaneous power (a) and the concentrations of the main radical species (b) during 2 nanoseconds of the simulation at constant tension

equal to 10.8 (kV pp), O₂/CH₄ ratio of 0.3 (v/v) and argon concentration equal to 0.375 (v/v).

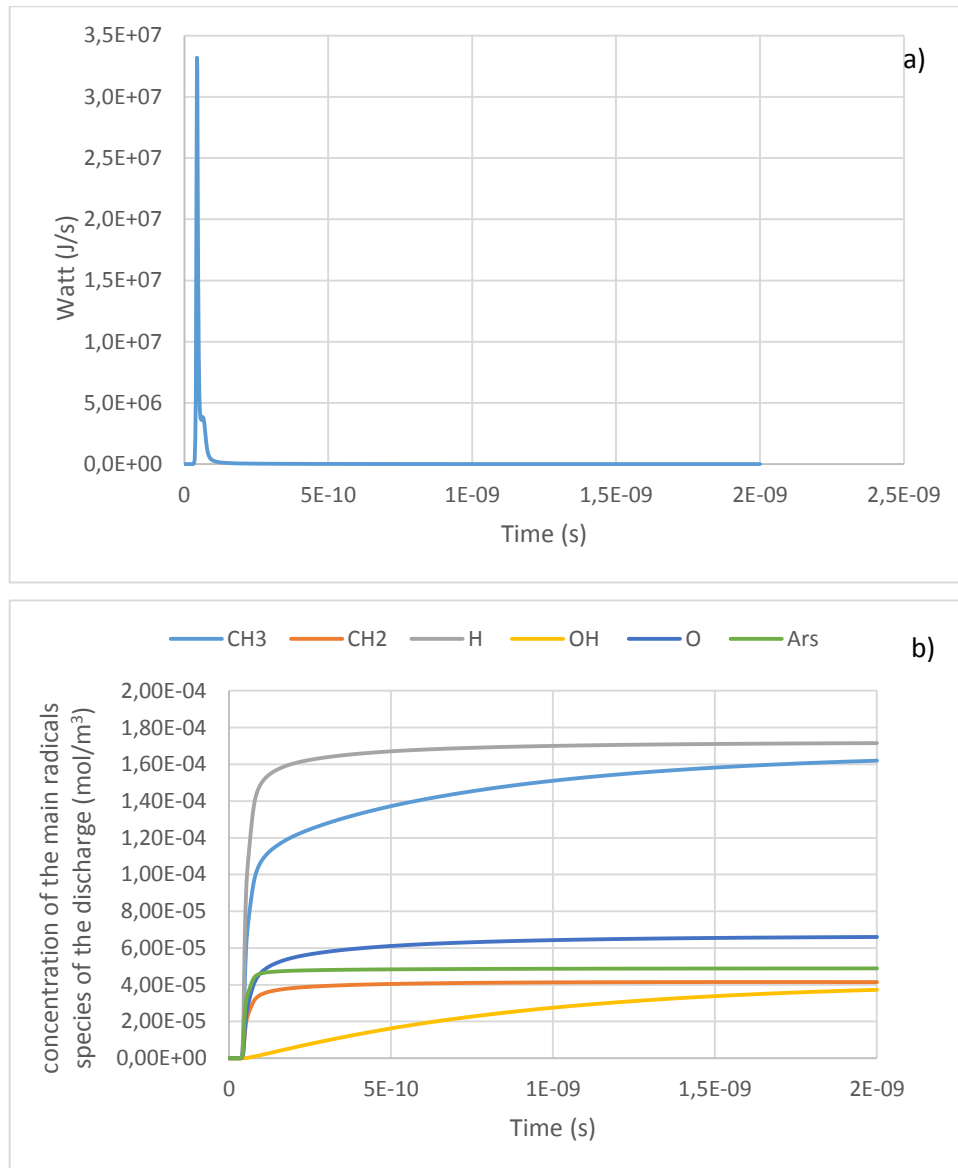


Figure 5.3. Evolution of the instantaneous power (a) and the concentrations of the main radical species (b) during 2 nanoseconds of the simulation at constant tension equal to 10.8 (kV pp), O₂/CH₄ ratio of 0.3 (v/v) and argon concentration equal to 0.375 (v/v).

The energy per micro-discharge (E_{dis}) was obtained by the integration of the curve $Watt f(t)$. Basing on the assumption that a single microdischarge occurred once each half-period, E_{dis} was multiplied by two (considering two discharges per period) times the frequency (f) value to obtain the simulated power W_{sim} .

5.4.2.2. 0D model for time evolution of chemical species

The COMSOL “chemical engineering module” was used to calculate the evolution of the different chemical species (radical and neutral species) during a time corresponding to the residence time of the gas reaction mixture in the plasma-millireactor. The chemical engineering module is a 0D model solving the conservation equations for neutral species:

$$\frac{dc_i}{dt} = v_i r_j + S_i \quad \text{Eq. 5.21}$$

The rate equation for a chemical reaction, considering forward and reversible rate constant (k^f and k^r), is calculated as:

$$r_j = k_j^f \prod_{i=1}^{Q_r} C_i^{-v_{ij}} - k_j^r \prod_{i=1}^{Q_p} C_i^{v_{ij}} \quad \text{Eq. 5.22}$$

The kinetic constants were calculated under Arrhenius law consideration as follows:

$$k^f = A^f e^{\frac{-E^f}{R_g T}} \quad \text{Eq. 5.23}$$

$$k^r = A^r e^{\frac{-E^r}{R_g T}} \quad \text{Eq. 5.24}$$

Where E is the activation energy for the reaction (J/mol), R is the universal gas constant (J/mol.K), T is the temperature of the reaction (K) and A is the pre-exponential factor.

In this model, the periodic production of radical species due to the periodic occurrence of micro-discharges in the reactor was represented by source terms in the equation Eq.5.25. During the time the micro-discharge was supposed to take place, the source terms S_i in the equations 5.21 were not zero. Their values in $\text{mol.m}^{-3}.\text{s}^{-1}$ were calculated using the concentration of the radicals after 10 ns calculated with the DBD model. The following equation was used:

$$S_{i \text{ source}} = \frac{C_i}{t_{dis}} \left[\frac{\text{mol}}{\text{m}^3 \text{s}} \right] \quad \text{Eq. 5.25}$$

Where C_i is the concentration of the intermediate species, and t_{dis} the micro-discharge duration equal to 10 ns.

In the 0D model, the standard set of equations and parameters for the kinetic model of

the compression/ignition template, available in the COMSOL library, was used. 215 complementary reactions were declared to predict the behavior of missing species (propane) in the compression/ignition template model. The complete kinetic model used in this study is described in annex 3.

5.5. Simulation results

5.5.1. Results obtained with the sinusoidal model

As a first result of this study, it was possible to visualise the filamentary discharge behaviour and streamers formation when adequate voltage and frequency are applied. In **figure 5.4**, the total current at the grounded electrode is plotted versus time.

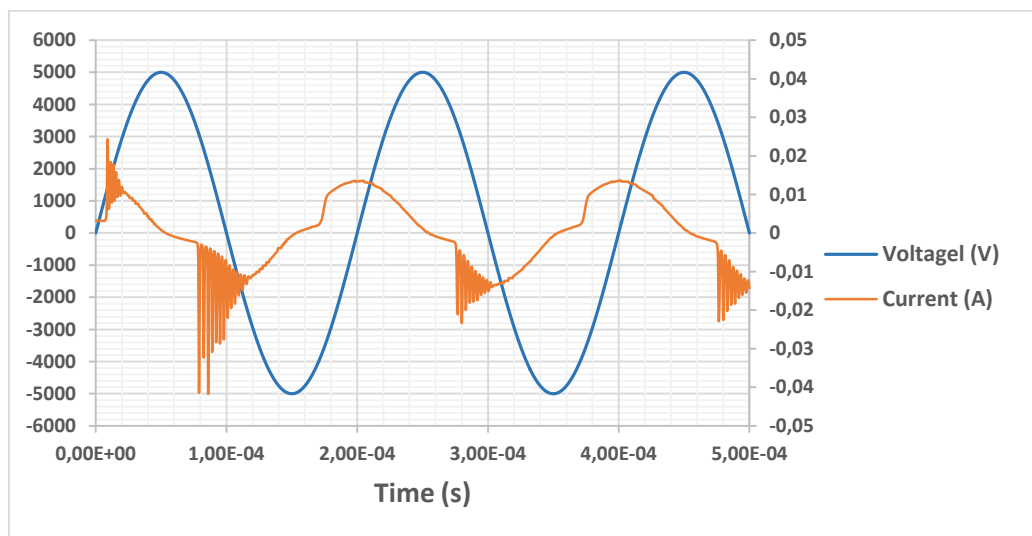


Figure 5.4. Calculated current evolution during sinusoidal discharge. Applied voltage: 10 kV pp; frequency: 4 kHz. Initial mixture: Ar = 0,4 / CH₄ = 0,4 / O₂ = 0,2.

In the absence of the plasma, the current would be a perfect cosine wave. However, the presence of the plasma and flow of charged particles leads to a non-uniform sinusoidal current waveform. The many tiny current breakdown phenomena that appear in **Figure 5.4** characteristic behavior of the formation of microdischarges or filaments that extend across the discharge gap.

The instantaneously total capacitive power in the plasma can also be plotted as seen in **Figure 5.5**. Power absorption differs from one half cycle to another because the reactor has one dielectric side, thus secondary electron emission is not symmetric.

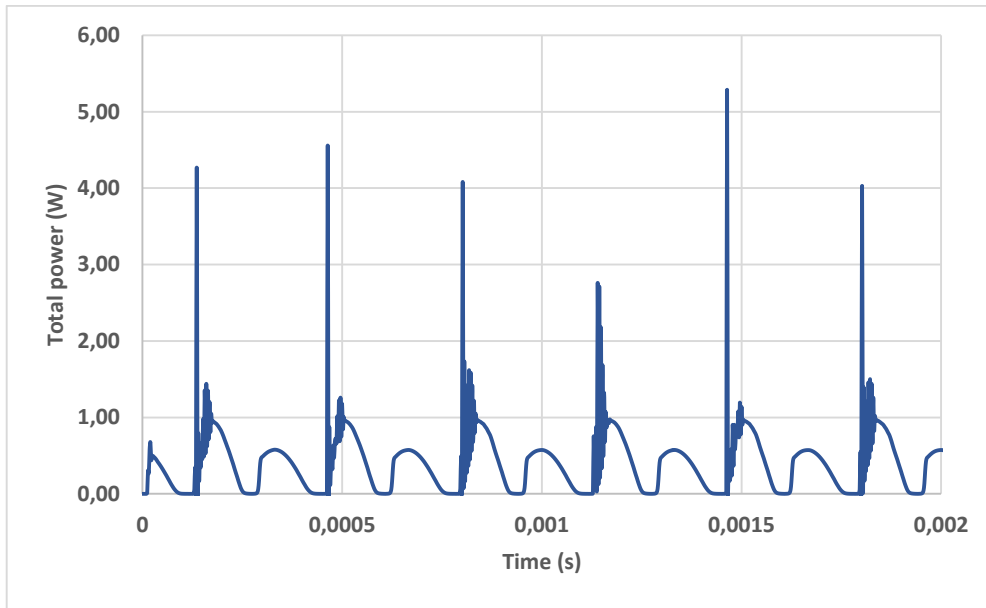


Figure 5.5. Simulation results of total capacitive absorbed power during sinusoidal discharge. Applied voltage: 10 kV pp; frequency: 3 kHz. Initial mixture: Ar = 0,4 / CH₄ = 0,4 / O₂ = 0,2.

Time averaging of this curve allows the calculation of the mean value of absorbed power as function of applied voltage, frequency and initial gas mixture composition. Simulation results give mean power values approximately twice as high as those obtained experimentally by Lissajous method. In addition, calculated values consider only low conversion mixtures whereas the experimental value on **figure 5.4** was obtained at a methane conversion of 0.38 %.

According to the model, the mean injected power values increase almost linearly with applied voltage amplitude. **Figure 5.6** shows that power was increased by more than two folds when voltage is increased from 10 to 17 kV pp at a frequency of 3 kHz. It is also reported an underestimation of the simulation results with respect to the experimental data of approximately 2 Watts.

This difference may be explained by the approximations used in the model such as the gas mixture homogeneity. Indeed, the presence of preferential paths for the micro-discharges or “hot-spots” has been shown in chapter 4. However, these phenomena could eventually increase the energy demand in the system because of local heating.

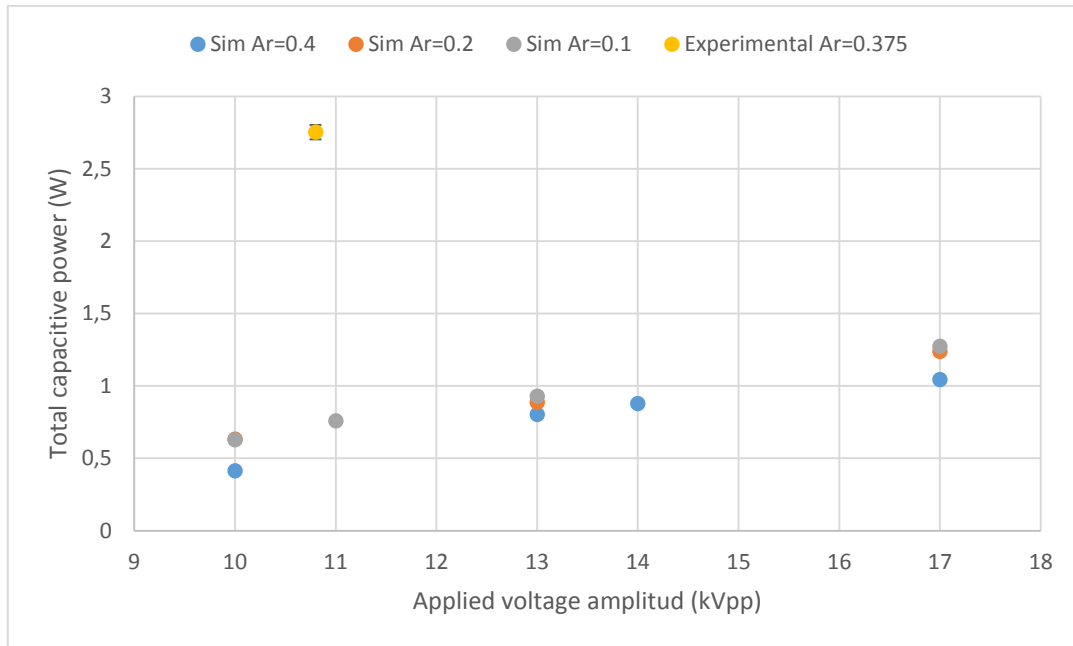
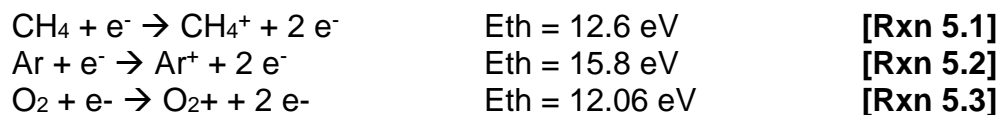


Figure 5.6. Mean total capacitive power values (simulated and experimental data) as a function of applied voltage amplitude and Argon molar fraction. Calculations for frequency at 3 kHz and $O_2/CH_4=0.5$.

On the other hand, the simulation results indicate that total capacitive power decreases by around 25% when argon initial molar fraction is increased from 0.1 to 0.4. This delta in the power variation can be explained by the comparison of threshold energies values of the following ionization reactions:



To be ionized, the argon molecule needs more energetic electrons compared to oxygen or methane. As a result, for a given voltage, there is less electrons and therefore less energy dissipated when the gas mixture contains Argon.

In addition to the prediction of energetic behavior, simulation of sinusoidal regime permitted the monitoring of the spatially averaged densities of the electrons, ions and radicals as a function of time within several periods.

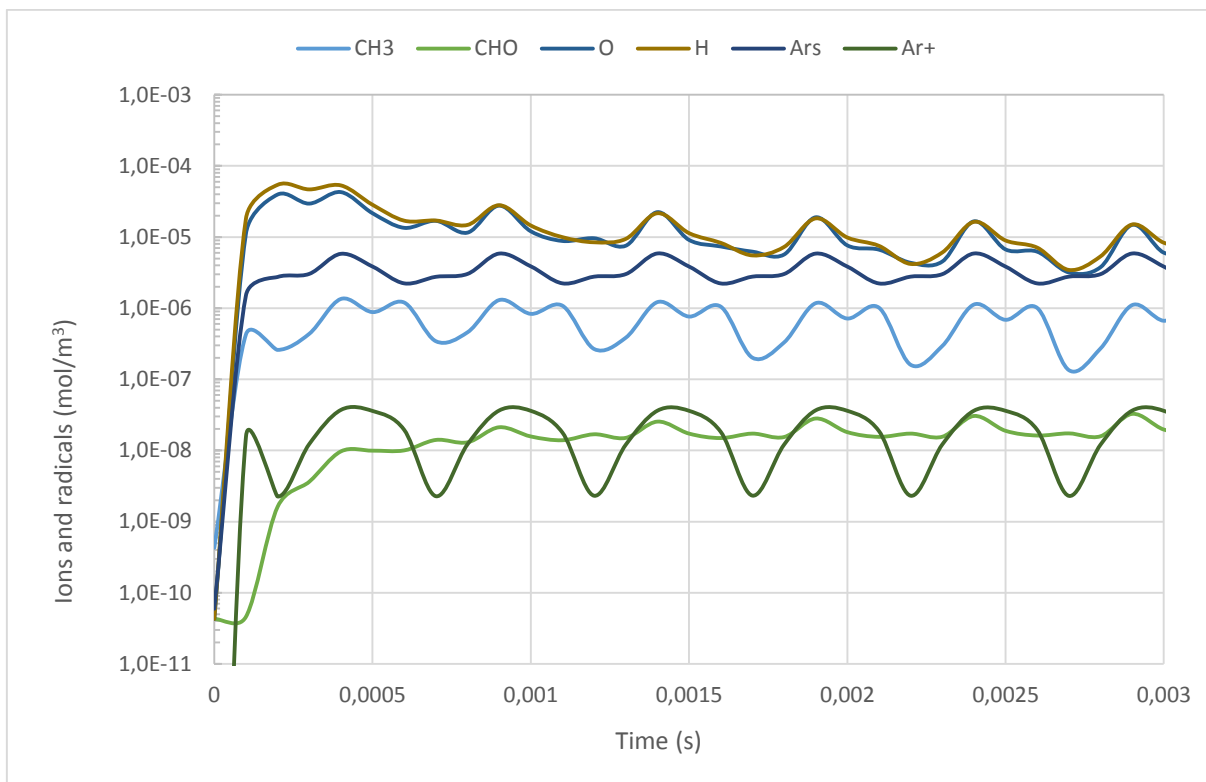


Figure 5.7. Calculated evolution of ions and radicals as a function of time within 1 ms. Applied voltage= 6500V; frequency= 4kHz. Initial mixture molar fractions Ar=0.4/CH₄=0.4/O₂=0.2.

A periodic behavior is found for ions and some radical species (**Figure 5.7**), although the effect is more pronounced for some species (e.g., Ar⁺, Ars, O and CH₃) than for others, such as CHO, HO₂, CH₃O and OH as illustrated in **Figure 5.8**. This difference is related to the different production and loss processes for the species, e.g., species directly produced by electron impact reactions will thus show more oscillating behavior than other species produced by heavy particle collisions.

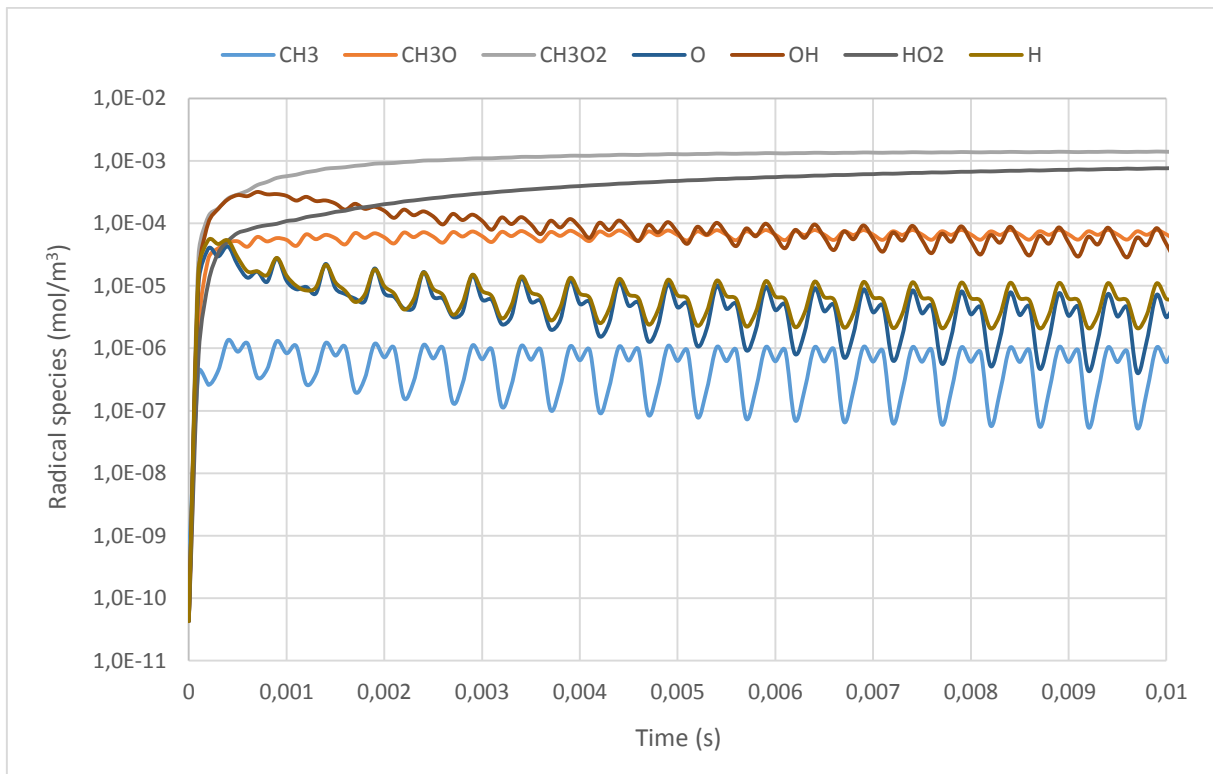


Figure 5.8. Calculated evolution of main radicals as a function of time within 0.017 s. Applied voltage= 6500V; frequency= 4kHz. Initial mixture molar fractions Ar=0.4/CH₄=0.4/O₂=0.2.

The molar fractions of the different stable molecules formed in the reactor can also be plotted as a function of “residence” time. It is noticed in **Figure 5.9** that only some of molecules (like C₂H₆ and H₂) show a very weak periodicity behavior like for some radicals. These species are the results of direct recombination of radicals produced by electron impact reactions.

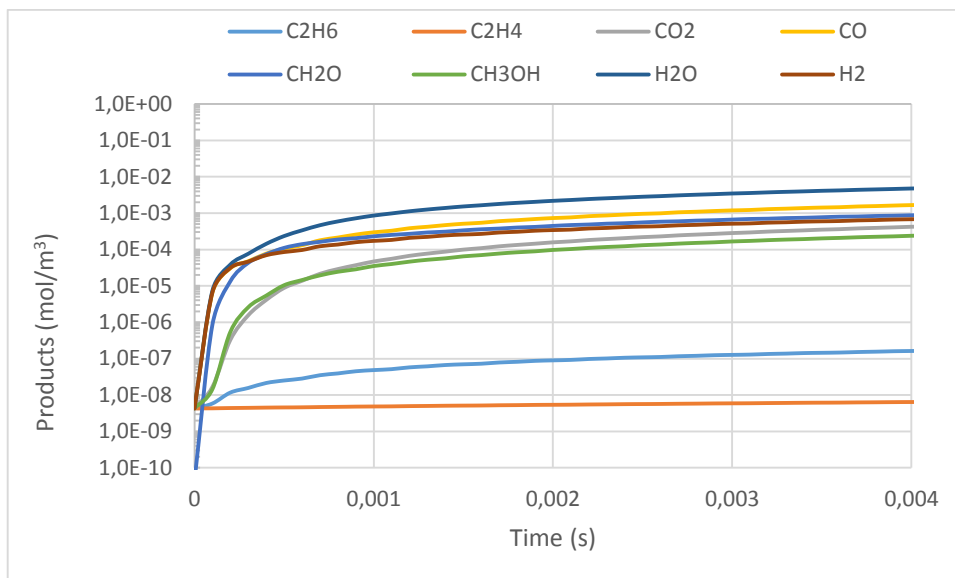


Figure 5.9. Products evolution during sinusoidal discharge. Applied voltage: 5kV; frequency: 4kHz; Initial mixture: Ar=0,4/ CH₄=0,4/O₂=0,2.

Due to long time calculations and high memory volume of files, it was not possible to make calculations for residence times more than 0.08 s. **Figure 5.10** presents an overall evolution of main products under a sinusoidal voltage amplitude of 5 kV and a frequency of 4 kHz applied to a mixture containing 0.2 mole fraction of argon and CH₄/O₂= 2 in linear scale **figure 5.10 a** and logarithmic scale **figure 5.10 b**.

The results show that while the molar fractions of some molecules steadily rise as a function of time (CO₂), the molar fractions of other molecules go over a maximum (CH₂O), or show a plateau (C₂H₄) after some time. This is important to realize that a careful selection of the residence time can entail a higher production of some targeted molecules.

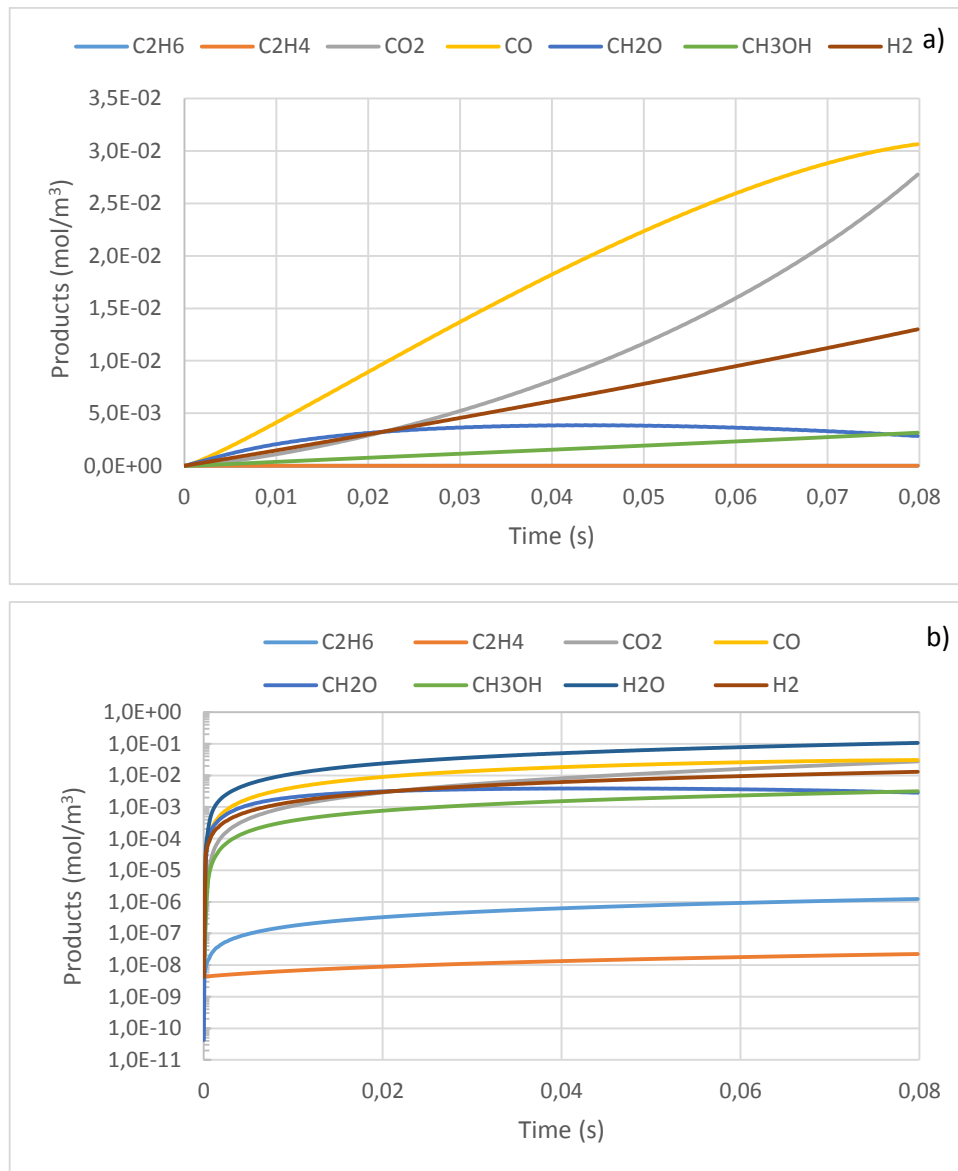


Figure 5.10. Products evolution during sinusoidal discharge a) linear scale et b) logarithmic scale. Applied voltage: 5kV; frequency: 4kHz; Initial mixture: Ar=0,2 / CH₄=0,53/O₂=0,27.

Basing on the results of the sinusoidal DBD model, the main reaction pathways in the DBD plasma millireactor for a mixture containing argon (0,1 – 0,4 of molar fraction) and CH₄/O₂ (ratio 1-4) can be described, allowing a better understanding of the reaction mechanism of partial oxidation of methane in a DBD plasma reactor for the considered geometry.

Description of the main reaction pathways: The evolution of species with time can be plainly described in two scales of time: up to 10⁻⁵ s, where reactions with “primary” radicals are important, and from 10⁻⁵ s, where stable compounds are mainly formed.

Main reactions up to 10^{-5} s: CH_3 and H , formed by plasma-induced CH_4 dissociation (Rxn 5.4 – Rxn 5.7), are quickly consumed by O_2 to form essentially CH_3O_2 and HO_2 (reactions (Rxn 5.8, Rxn 5.9). These reactions are favoured by a free activation energy barrier and high O_2 concentration.

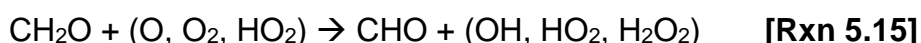
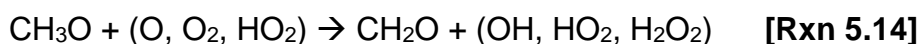


The formation of H_2 and C_xH_y by recombination of primary radicals, CH_x and $\cdot\text{H}$, occurs in a very short time, but remains limited due to the faster $\text{CH}_3\text{O}_2\cdot$ and HO_2 radicals formation. The main $\cdot\text{O}$ consumption comes from the reaction with $\text{HO}_2\cdot$ and with CH_3O_2 to form OH and $\text{CH}_3\text{O}\cdot$, respectively.



Main reactions after 10^{-5} s:

Stable compounds are mainly formed after 10^{-5} s via reactions involving the radical species previously mentioned. CH_3O_2 appears to be the key compound, leading to the formation of several other compounds, such as CH_3OH . Under considered conditions, the main part of CH_3O_2 is involved in reactions producing CH_3O . By dehydrogenation driven by various species, CH_3O promptly produces CH_2O . Analogous dehydrogenation of CH_2O leads to CO and CO_2 formation, by intermediate formation of CHO .



As a summary, after 1 ms of residence time, main stable products are CO , CO_2 , H_2 . CH_2O appears as a major product in the studied time range but later, it undergoes consumption reactions. CH_3OH is produced under studied conditions but remains a

minor product (5-15% of CO). It is likely that longer residence time would promote methanol decomposition reactions. This is however not observed on the simulation results, maybe due to the fact that some reactions are missing in the reduced kinetic model.

The 1D sinusoidal model is therefore a very interesting tool to understand the main reactions involved during the partial oxidation of methane under plasma conditions. However, it is not possible with this tool to perform simulations at the scale of the second, corresponding to the residence time in the milli-reactor, because it would need too high machine and time requirements. For example, to simulate the time evolution of the concentrations during 80 ms, the calculation time is around 12 hours. Using the multi-timescale model the calculation time for the same conditions is reduced to 2 hours. The results obtained with the multi-timescale model, are developed here after.

5.5.2. Results obtained with the multi-time scale model

The results described in the following section were obtained by simulating a single discharge in the time range of 0-2 ns with the 1D DBD model implemented on the COMSOL Plasma module. The main purpose of this section is to understand and identify the behavior of the principal variables occurring in a time range of 0-2 ns. The simulation time was approximately 5 min.

5.5.2.1. Energetic aspects

In the following results, the objective was to see if one DBD microdischarge medialization can simulate accurately the influences of Ar percentage and O₂/CH₄ ratio on the energy per period by comparing theoretical and experimental evolutions of E_{dis}. The theoretical and experimental values of E_{dis} will not be directly compared because as said previously in section 5.3.2, the real number of micro-discharges per period and the real voltage at which the micro-discharges occurs are not known, making an energy comparison impossible.

The **Figure 5.11** shows the comparison between the experimental and simulated results showing the behavior of the energy dissipated during one period as a function of the concentration of argon at constant O₂/CH₄ ratio of 0.3 (v/v). It is observed that the values obtained by simulation are almost stable when the concentration of argon

increases. The same trend was observed previously with the sinusoidal model. This evolution is opposite to the one observed experimentally: indeed the measured energy per period increased from $5 \cdot 10^{-4}$ to $7,3 \cdot 10^{-4}$ J when the argon concentration increased from 0 to 0.375 (v/v).

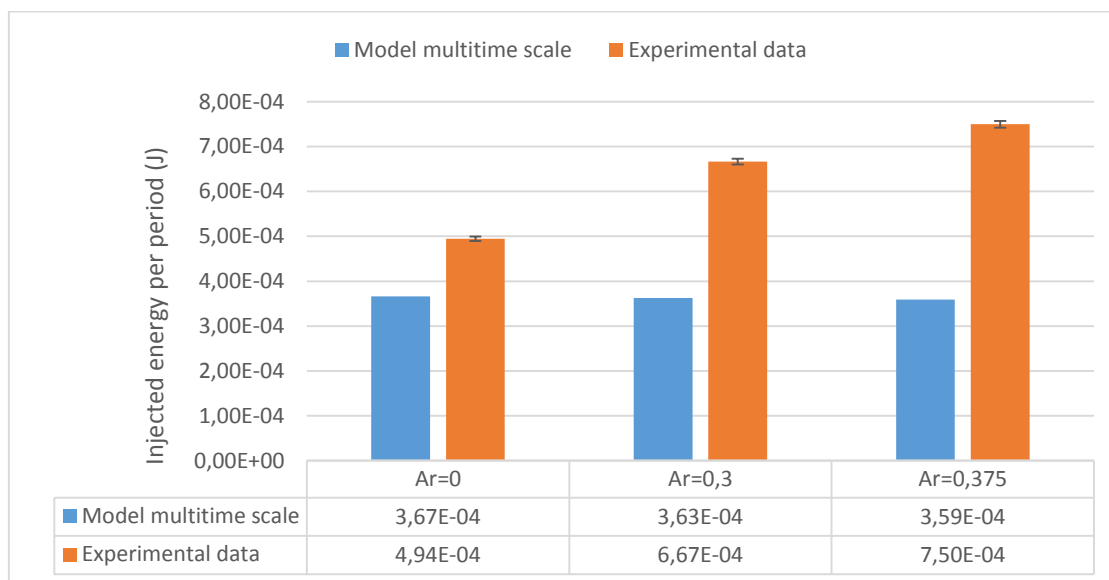


Figure 5.11. Comparison between the experimental and simulated behavior of the energy dissipated during one period as a function of the concentration of argon at constant O_2/CH_4 ratio of 0.3 (v/v).

This difference between the experimental and simulation results is probably due to the fact that energy transfer reactions (Penning effect) were not taken into account in the model. In any case, a future research work is needed to clarify this behavior.

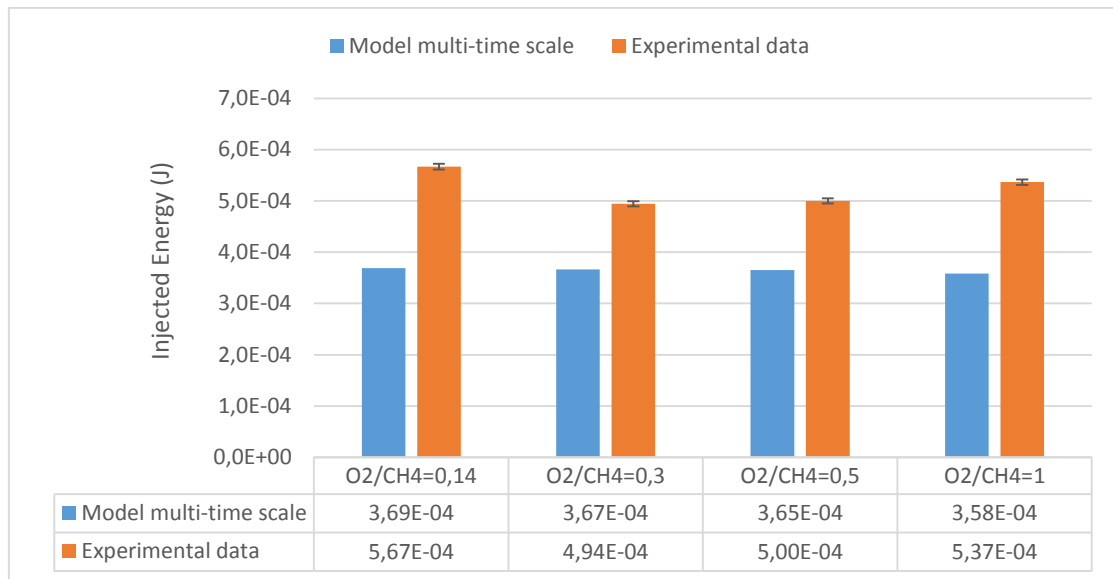


Figure 5.12. Experimental and simulated comparison of the energy applied as a function of the O₂/CH₄ ratio without presence of argon.

The **Figure 5.12** shows the comparison between the experimental and simulated results showing the behavior of the energy applied as a function of the O₂/CH₄ ratio without presence of argon. It is reported again no difference in the energy values as a function of O₂/CH₄ ratio. However, this time this is coherent with the experimental results which indicate also almost no difference between E_{dis} values at the different O₂/CH₄ ratio.

5.5.2.2. Production of primary radicals

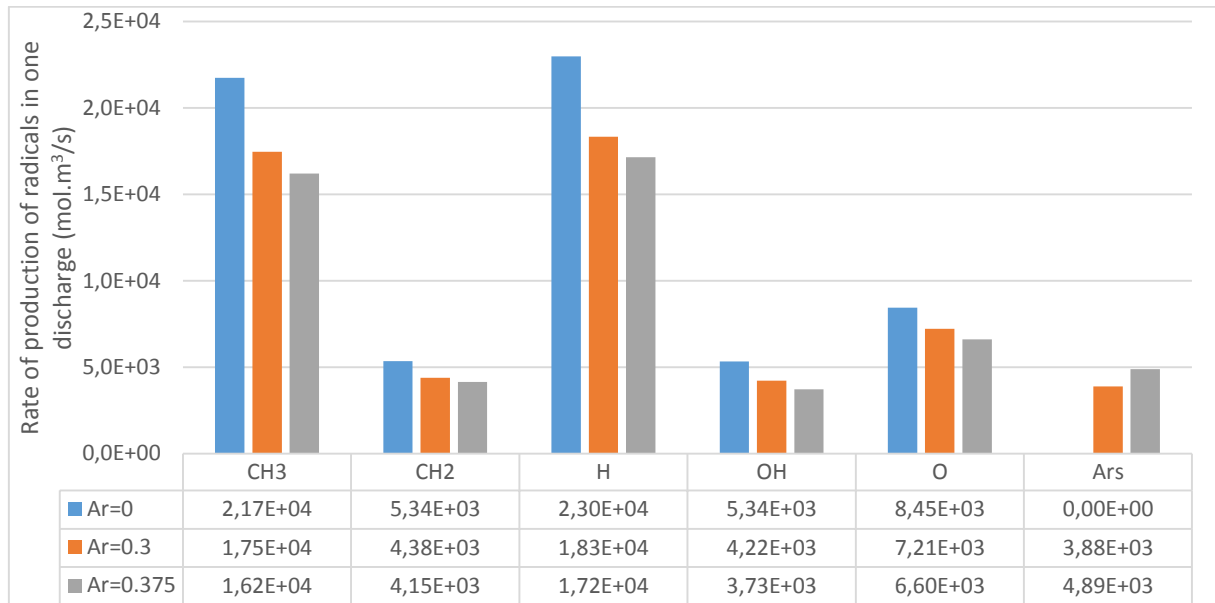


Figure 5.13. Rate of production of radicals in a single discharge with different concentrations of argon at constant value of tension equal to 10.8 kV and ratio O_2/CH_4 equal to 0.3.

In **figure 5.13** is presented the average rate of production of radicals during the first 0.6 nanoseconds in a single discharge with different concentrations of argon at constant value of tension equal to 10.8 kV and ratio O_2/CH_4 equal to 0.3. There is observed that the main radicals produced in the discharge are CH_3 , CH_2 , H, OH and O.

It can be noticed that if the concentration of argon increases, the radical production rate decreases, in particular the production rate of CH_3 and H. This can be directly related to the decrease of CH_4 concentration, what reduces the probability of collisions between the CH_4 molecules and the electrons.

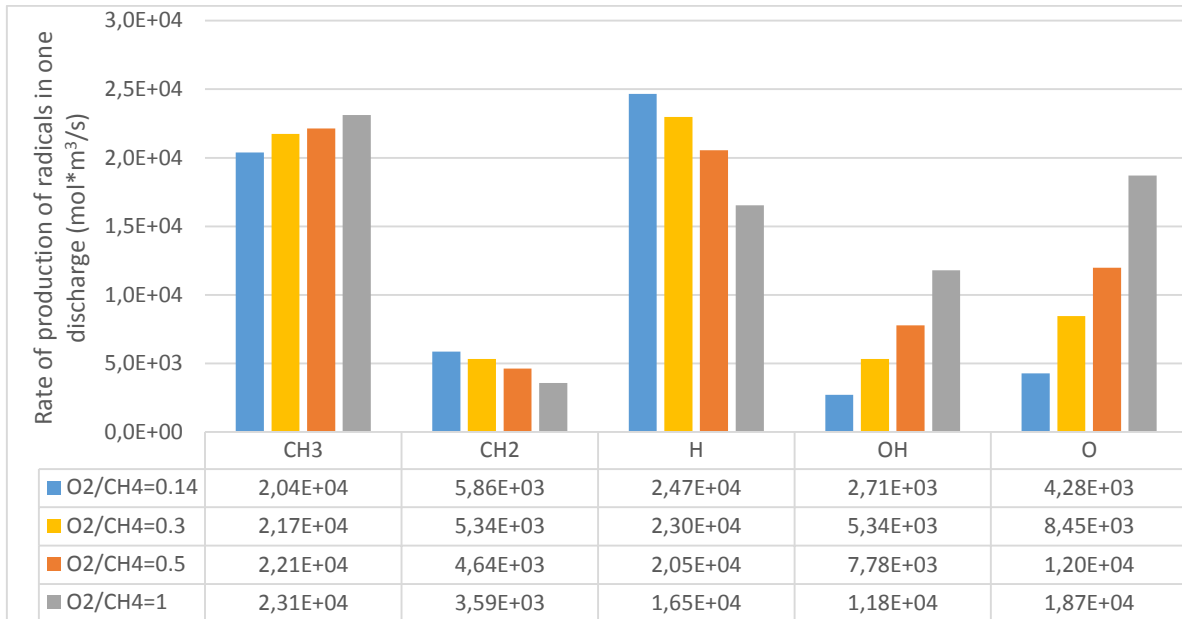


Figure 5.14. The rate of production of radicals in a single discharge at different ratios of O₂/CH₄ without argon and constant value of tension equal to 10.8 kV.

In **figure 5.14** is presented the rate of production of radicals in a single discharge at different ratios of O₂/CH₄ without argon and constant value of tension equal to 10.8 kV. Again the main radicals produced in the discharge are CH₃, CH₂, H, OH and O.

It can be noticed if the ratio of O₂/CH₄ increases, the radicals CH₂ and H decrease. On the contrary, the oxygen radicals OH and O increase notably along with a slight increase in the production of CH₃ if the ratio O₂/CH₄ increases. This behavior was expected since the increment of the concentration of oxygen implies a greater quantity of O₂ molecules available for the production of oxygen radicals.

5.5.3. Comparison of sinusoidal model and multi-time scale model

5.5.3.1. Energetic aspects

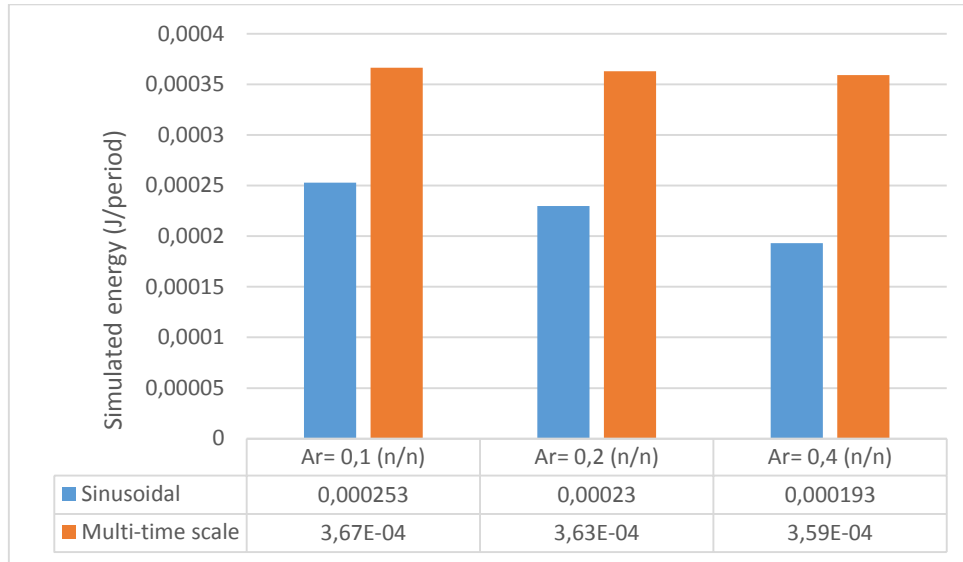


Figure 5.15. The simulated energy (J/period) requirement in both models (sinusoidal and multi-scale time) at constant O₂/CH₄ ratio equal to 0.5 (n/n)

In **figure 5.15** is showed the simulated energy (J/period) requirement in both models (sinusoidal and multi-timescale) at constant O₂/CH₄ ratio equal to 0.5 (n/n). In both models it is observed that the value of the energy per period increases if the concentration of argon decreases. This behavior is not consistent with the experimental behavior reported in chapter 3 of this thesis. Possibly due to the omission of reactions of the Penning effect type which could favor the production of metastable argon (Ars) which then reacts with stable gas molecules (Penning effect) changing to a reactive medium with higher energy demand.

However, only a slight decrease in the energy value is reported in the case of the multi-time scale model. On the other hand, in the sinusoidal model, a notable increase in energy value per period is reported if the argon concentration decreases. This may due to the continuous temporal evolution that characterizes this model. Indeed in the sinusoidal model the applied voltage is the real sinusoidal one whereas the multi-time scale model supposes that a voltage of 10.8 kV pp is applied during 2 ns every 0.16 ms.

5.5.3.2. Production of stable species at low constant SIEM

In **figure 5.16** are reported the methane conversion (a) and the main products formed (b) for the two different models (sinusoidal and discharge-postdischarge) when the partial oxidation of methane is performed in the DBD millireactor studied using a peak to peak voltage of 10 kV, a frequency equal to 4kHz, a SIEM equal to 70 kJ/mol_{methane in} and the following composition for the inlet mixture: Ar=0,2 CH₄=0,53, O₂=0,27 (molar fraction).

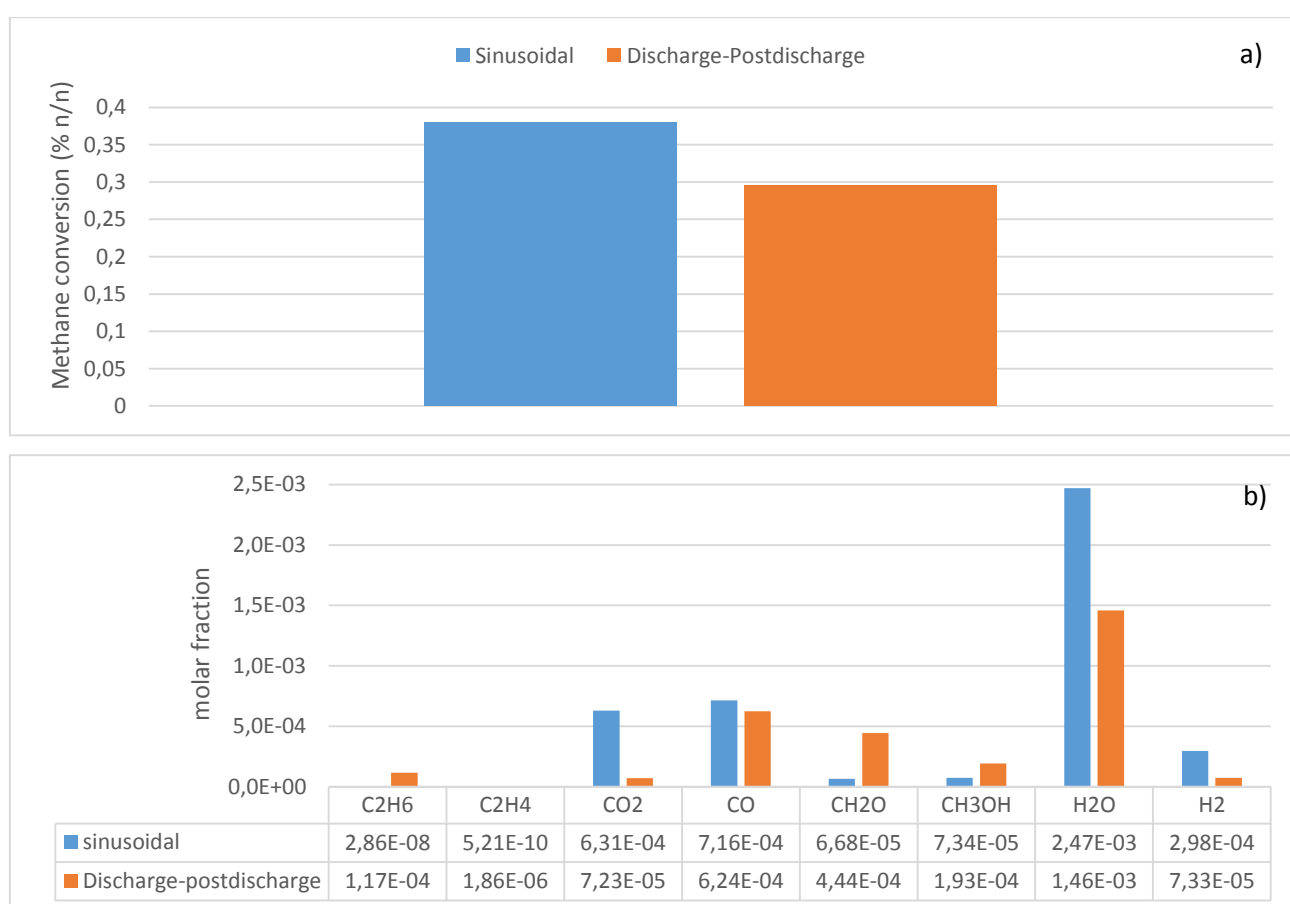


Figure 5.16. Methane conversion (a) and the main products formed (b) for the two different models (sinusoidal and discharge-postdischarge) at SIEM = 70 kJ/mol_{methane in}.

It is observed that the methane conversion (figure a) is similar in both models, showing a slightly higher value in the case of the sinusoidal model. The CO molar fractions are similar in both models, 7.1 and 6.2 E10⁻⁴ in the sinusoidal and multi-timescale models respectively. In the case of the other products (C₂H₆, C₂H₄, CO₂, CH₂O, CH₃OH, H₂O and H₂) a significant difference between models is reported. In the sinusoidal model,

the molar concentrations of CO₂ and H₂ are markedly higher than in the multi-timescale model (8.7 and 4 times higher respectively). On the contrary in the multi-timescale model the concentrations of CH₃OH and CH₂O are higher than in the sinusoidal model (2.6 and 6.6 times higher respectively). Finally, there is reported almost no production of C₂H₆ in the sinusoidal model whereas a concentration of C₂H₆ equal to 1.17 E10⁻⁴ is reported in the discharge-postdischarge model.

The variation presented in the distribution of products in both models could be due to the fact that sinusoidal model consists of a reduced POM model of 44 reactions, whereas the discharge-postdischarge model incorporates 252 reactions.

To verify which model is the more accurate to predict the products formation, in **table 5.2**, the H₂/CO and CO₂/CO ratios calculated from the results presented in **figure 5.16** are compared with the values obtained by the team of Nozaki et, al. [65]. The experimental H₂/CO and CO₂/CO ratios obtained in this study (see **figure 4.7**) were not used for this comparison because as said previously they may be affected by the presence of “hot spots” in the plasma millireactor.

Table 5.2. Experimental and simulated results in sinusoidal and multi-time scale

	Sinusoidal	Multi-time scale	Experimental data (Figure 4.7)	Nozaki et, al. [65]
H ₂ /CO (mol/mol)	0,416	0,117	≅ 1	≅ 1
CO ₂ /CO (mol/mol)	0,881	0,115	≅ 0.8	≅ 0.1

It is important to notice that the CO₂/CO ratio obtained with the multi-timescale model is close to the one reported in the literature which oscillates around 0.15 (n/n). On the contrary the CO₂/CO ratio given by the sinusoidal model is higher (around 0.9).

On the other hand both models reported an underestimation of the H₂/CO ratio respect to the experimental and theoretical results (which oscillate ≅ 1 n/n). However the sinusoidal model is the one that presented a better approximation with a value of 0.41 (n/n).

In which concern to the reported results for the CO₂/CO ratio, there is a discrepancy between the experimental results and those found in the literature possibly due to the influence of factors such as non-uniformity of discharge and presence of “hot spots”. The multi-time scale model reported a better approximation to the results found in the

literature which could suggest a better general prediction capacity, in systems with homogeneous phenomena which could eventually increase the production of CO₂.

To conclude this sinusoidal model is able to mimic the successive formation of filamentary discharges and to characterize the plasma chemistry evolution for a given starting mixture at constant tension and frequency. It permits the evaluation of electron energy spatially and temporally and to evaluate its impact on the gas chemistry when electron impact and radical mechanisms are combined. However, this type of model presents high requirements in hardware and prolonged simulation times. Moreover, the kinetic radical model is a simplified one (127 reactions) and some important reactions may be missing.

On the other hand, the multi-time scale model is presented as an interesting and audacious solution to this problem. It was declared the periodic production of radical species supposing a micro-discharge periodicity with a constant lifetime (as mentioned before). As a result the requirements of equipment and time are greatly diminished compared to the sinusoidal DBD model, even if a more complete radical kinetic model was used (252 reactions).

In the next section, due to limitations in hardware, simulation at higher residence times were proposed the multi-timescale model.

5.6. Comparison of multi-time scale model results and experimental results

One of the objectives of the simulation is to observe and understand the favorable conditions to increase methanol selectivity, in this case, the 6% of methane conversion simulated is enough since the higher values of methanol selectivity are obtained at the lower values of methane conversion.

5.6.1. Methane conversion

In **figure 5.17** is showed the experimental and simulated methane conversion in function of SIEM at different values of O₂/CH₄ ratio in the absence of argon. It can be observed that the theoretical values of methane conversion are lower than the experimental ones for a given SIEM, especially for high O₂/CH₄ ratios. This is likely

due to the numerous approximations in the multi-timescale model. For example, as already said, the model does not predict the non-uniformity of the injected power in the system described in section 4.1. However, the presence of highly energy-charged areas eventually could increase the global methane conversion.

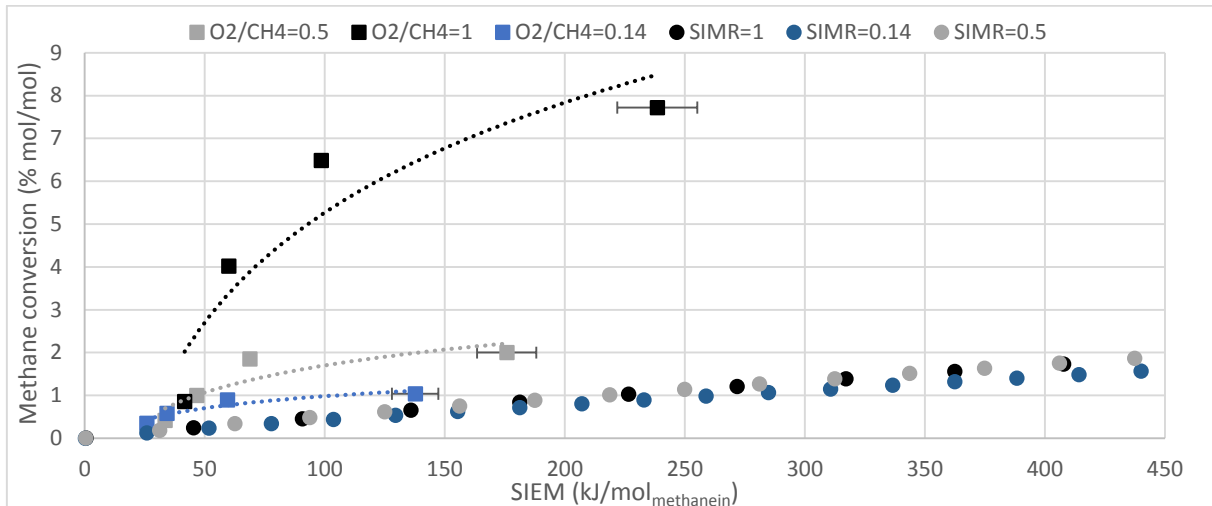


Figure 5.17. Experimental and simulated methane conversion in function of SIEM at different values of O₂/CH₄ ratio in the absence of argon.

Concerning the influence of the O₂/CH₄ ratio on the results obtained from the simulation, it is only possible to perceive a slight decrease of the conversion if the O₂/CH₄ ratio decreases at a constant SIEM value. Therefore, even if in the model the increase of O₂/CH₄ was shown to lead to a significant increase (+ 400% for O° radicals) of the oxygenated radicals generated by the discharge (**figure 5.14**), this phenomenon does not cause a significant increase of the methane conversion. The theoretical results then do not confirm that the significant increase of methane conversion observed experimentally would be due to the increase of oxygenated radicals. The assumption made previously in chapter 4 (section 4.2.3 second paragraph) is then not confirmed. Again the influence of the O₂/CH₄ ratio on the discharge uniformity could explain the significant increase of methane conversion observed experimentally.

In **figure 5.18** is showed the methane conversion in function of SIEM at different values of argon concentration, as a comparison between the experimental and simulated results. Again the theoretical conversions are lower than the experimental ones.

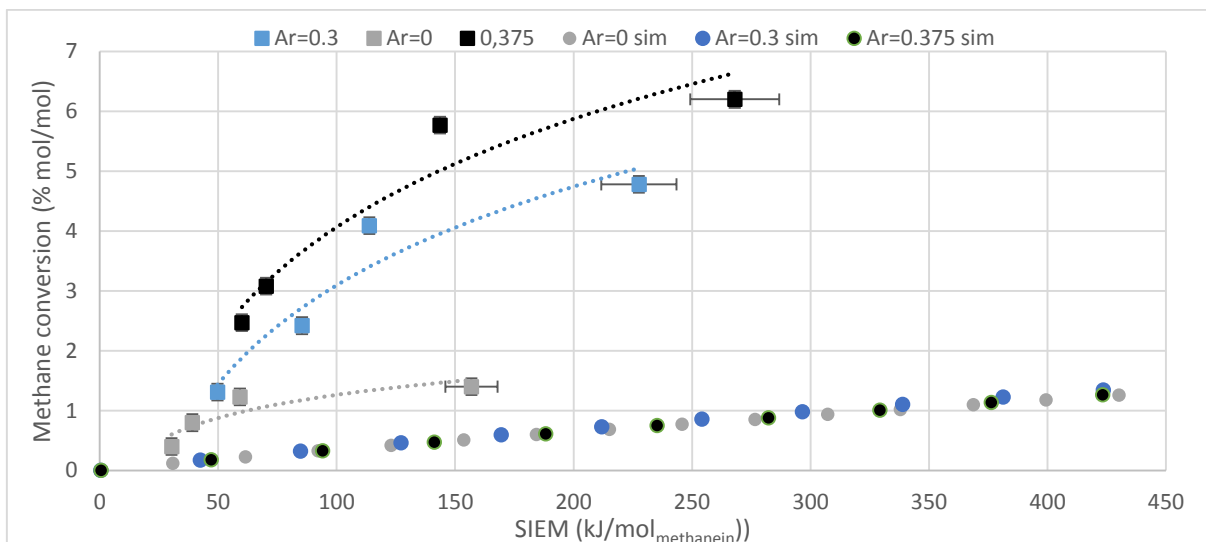


Figure 5.18. Experimental and simulated methane conversion in function of SIEM at different values of argon concentration.

According to the results obtained from the simulation, there is no significant change of the conversion of methane at constant SIEM at percentages of argon from 0 to 0.375 v/v. Again the model is not able to predict the influence of the argon observed in the experiments. At 150 kJ/mol_{methane} for example, the addition of 0.3 and 0.375 v/v of argon lead to increment of methane conversion of around 300%. This is possibly due to the fact that energy transfer reactions (Penning effect) were not taken into account in the model as mentioned before and the model is not able to predict correctly the fate of the activated Ar molecules (Ar*) which may eventually react with the methane molecules, causing higher CH₄ conversion. Indeed the kinetic model does not contain the reaction between Ar* and CH₄.

5.6.2. Influence of Argon percentage on methanol selectivity

In **figure 5.19** is presented the methanol selectivity in function of the methane conversion at different values of argon concentration as a comparison between the experimental and simulated results. In the case of the simulated data is possible observe that the methanol selectivity rapidly increases and then decreases, showing a maximum in methanol selectivity, at methane conversion value lower than 1 %.

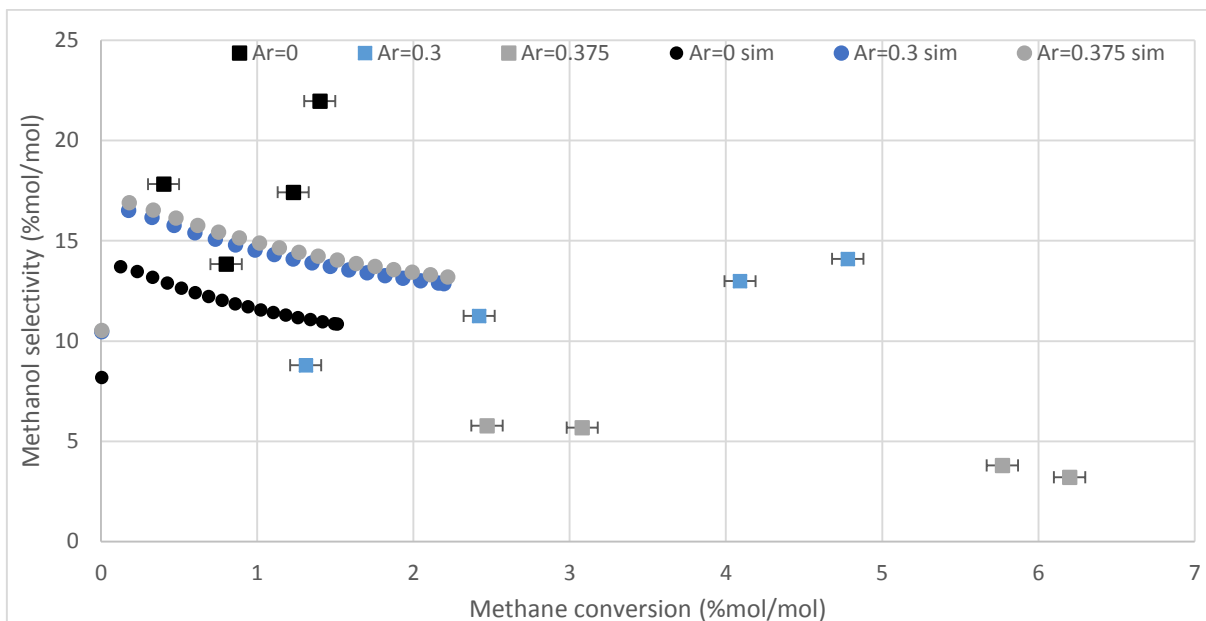


Figure 5.19. Methanol selectivity as a function of methane conversion, as a comparison between experimental and simulated data at different values of argon's concentration (0, 0.3, 0.375 v/v), constant value of flow rate (48 sccm) and O_2/CH_4 ratio (0.3 v/v).

The selectivity of methanol increases if we increase the concentration of argon in the system from 0 to 0.3 at constant methane conversion. On the other hand, if the concentration of argon increases from 0.3 to 0.375, there is almost no change in the selectivity of methanol at constant methane conversion.

This behavior is contradictory with respect to the experimental results. Indeed the experimental results (section 4.2.2 seventh paragraph) indicated that the methanol selectivity seemed to be better at low argon percentage. The discrepancy between experimental and theoretical results could be explained by the fact that the model does not consider the fast reactions between Ar^* and methanol leading to the destruction of methanol. Indeed, it has been shown in another simulation study that these reactions could considerably reduce the concentration of methanol [76]. Despite the above, the experimental and simulated results reported in **figure 5.19** present a fairly good approximation between them.

5.6.3. Influence of O_2/CH_4 ratio on methanol selectivity

In **figure 5.20** is presented the methanol selectivity in function of the methane conversion at different values of O_2/CH_4 ratio as a comparison between the experimental and simulated results. In both cases (experimental and simulated data)

it is observed that the highest values of methanol selectivity are presented at low methane conversion values and that if the value of the O_2/CH_4 ratio increases, the selectivity of methanol decreases at comparable methane conversion values. The simulated results indicate that the increase in methanol selectivity is more visible at low O_2 / CH_4 ratios. Indeed, there is a high decrement in methanol selectivity (7 units) if we increase the O_2/CH_4 ratio from 0.14 to 0.5 at 1% of methane conversion, but if the ratio increases from 0.5 to 1 the methanol selectivity decreases only 2 units at same value of methane conversion.

Concerning the role of O_2/CH_4 , experimental and theoretical results are then in agreement, confirming that a low O_2/CH_4 favours the methanol selectivity.

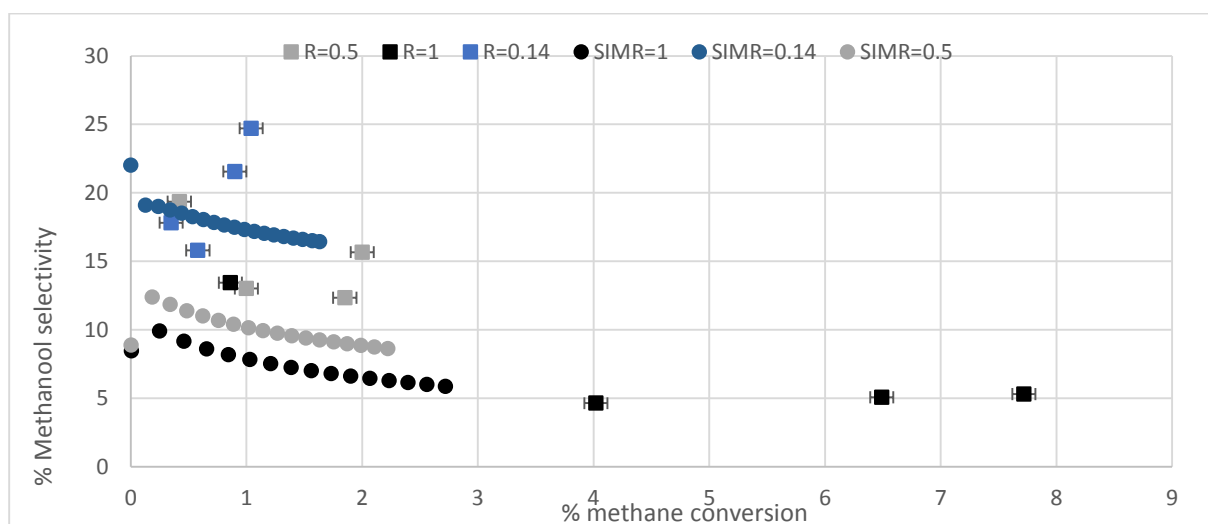


Figure 5.20. Methanol selectivity as a function of methane conversion, as a comparison between experimental and simulated data at different values of O_2/CH_4 ratio (0.14, 0.5, 1 v/v) and constant value of flow rate (48 sccm) without presence of argon.

5.7. Conclusion

In this chapter were presented the different chemical and physical processes taking place in the DBD plasma millireactor using the simulation tool COMSOL Multiphysics 5.1 as a first study to lay the foundation to understand and identify the different phenomena that have a significant influence on the selectivity of methanol and thus evaluate its possible increase. The electron transport and diffusion equations were solved simultaneously in time under the proposal of two models: sinusoidal model and multi-time scale model.

The sinusoidal 1D model was allowed to mimic the successive formation of filamentary discharges and to characterize the plasma chemistry evolution for a given starting mixture of gas when a sinusoidal electrical regime is applied to the studied reactor. Indeed, the model is able to describe the successive formation and propagation of streamers during several periods as a function of applied voltage amplitude and its frequency. However this model presents great requirements in hardware and simulation time, making it tedious and difficult to study the system a different operating conditions. A creative solution to this problem is proposed in multi-time scale model.

In the case of the multi-timescale model two models were used: using the plasma module, a DBD model was first used and then a simple 0D model. As a result the requirements of equipment and time are expected to be greatly diminished compared to the sinusoidal DBD model. However this approximation is acceptable as long as the methane conversion remains low.

An energetic comparison of both models (sinusoidal and multi-time scale) was showed. The behavior simulated were not consistent with the experimental data. This was explained by the omission in the model of the reactions describing the Penning effect. Nevertheless, the simulated results confirm that the increase in the O_2/CH_4 ratio favors the production of highly oxidizing compounds such as OH and O.

The methane conversion was similar in both models. On the contrary, important differences were observed for the concentration of reaction products.

In the study carried out to understand the influence of the argon variation in the methanol selectivity, the model presented a contradictory tendency with respect to the experimental results. This was explained by the omission of reactions of the Penning effect type. Despite the above, the experimental and simulated results reported present a good approximation between them.

Regarding the study of the influence of variation of the O_2/CH_4 ratio on methanol selectivity, the experimental and simulated data were in good approximation. However, a model was developed that laid the basis for the understanding of POM for the production of methanol, which opens the door to opportunities for improvement in selectivity of methanol and future studies of research.

General conclusions and outlooks

In the present thesis, a DBD plasma millireactor dedicated to the partial oxidation of methane POM has been conceived.

The topics of conversion and utilization of methane are important issues to tackle global warming. Controlled partial oxidation of methane to methanol through the catalytic reactions has been studied for a very long time as an alternative to methane disposal in the environment. Unfortunately, frequently replacement of spent catalysts and high energy consumption due to the high values of temperature and pressure typical in this process, add to the overall running costs of methane reforming.

Non-thermal plasma as a versatile source of reactive species performed in a millireactor proved to be a good candidate to replace traditional catalysts and avoid procedures like catalyst regeneration or the catalyst separation working at atmospheric pressure and low temperature. This thesis gives us fundamental insights on the feasibility of the application of non-thermal plasma/milli-technology in the partial oxidation of methane to produce methanol.

Firstly, great efforts have been made to establish the reactor's design and methods which allow to characterize and lead to the general understanding of the system during the reaction. Finally, a chemical quantification and qualification of the reaction was achieved in semi-continuous configuration, as well as the implementation of optical characterizations through the use of a camera ICCD (intensified charge-coupled device).

A transparent plasma DBD reactor was developed for the application of optical characterization of POM, by the development of a transparent electrode made with an alloy of ITO / Au / ITO which could support eventual temperature increases due to the nature of the reaction.

It was found that the frequency has a slight influence on the energy injected into the system compared to the tension. A slight increase in the value of tension has a considerable impact on the energy injected into the system and this is independent of the type of gas studied.

The optical characterization of the discharge by ICCD also was carried. It was found that the volumetric flow has a great influence in the homogeneity of the discharge and therefore in the energy distribution in the millireactor. It is reported improvements in

discharge uniformity along the millireactor channel at higher volumetric flow values, probably due to a better heat removal by convection what diminishes the phenomenon of “hot points” or “preferential paths”.

Methane conversions of up to 30% were obtained and the main compounds of reaction were syngas (CO and H₂), propane, ethylene, methanol and CO₂. It was found that the selectivity of methanol is favored at low values of energy injected in the system and in general its value increases if the volumetric flow increases possibly because the augmentation of the volumetric flow favors the uniformity of discharge and therefore allows a spatially homogeneous distribution of the energy. The influence of the composition of the reactive mixture also was studied.

The increase of the argon concentration in the system showed to have an unfavorable influence on the selectivity of methanol, possibly due to the increase in the concentration of intermediate species such as Ar * which can react directly with the methanol molecules leading to their destruction.

On the other hand, with respect to the O₂/CH₄ ratio, the increase in the values of this ratio implied a decrease in methanol selectivity, possibly due to the high production of oxidant species which react with the methanol molecules and decrease their selectivity.

A study that allows the identification of intermediary species as well as their temporal distribution for a better understanding of the POM was then made by using the COMSOL Multiphysics 5.1 simulation tool

Two model were proposed: the Sinusoidal model and the multi-time scale model. The sinusoidal 1D model was allowed to mimic the successive formation of filamentary discharges and to characterize the plasma chemistry evolution for a given starting mixture of Ar/CH₄/O₂ when a sinusoidal electrical regime is applied to the studied reactor. Results permitted the evaluation of electron energy spatially and temporally and to evaluate its impact on the gas chemistry when electron impact and radical mechanisms are combined. However this model needed great requirements in hardware and simulation time. A creative solution to this problem was proposed in multi-time scale model. For this reason, the multi-timescale model was proposed.

In the case of the multi-timescale model two models were used: using the plasma module, a DBD model was first used to determine the concentrations of radicals produced by a single microdischarge. Then a simple 0D model solving the conservation equations for neutral species was used to calculate the time evolution of the neutral species. As a result the requirements of equipment and time are greatly diminished compared to the sinusoidal DBD model.

The simulated results reported in this thesis were presented with the different chemical and physical processes taking place in the DBD plasma millireactor using the simulation tool COMSOL Multiphysics 5.1 as a preliminary study to lay the foundation to understand and identify the different phenomena that have a significant influence on the selectivity of methanol and thus evaluate its possible increase.

The electron transport and diffusion equations were solved simultaneously in time under the proposal of two models: sinusoidal model and multi-time scale model.

An energetic comparison of both models (sinusoidal and multi-time scale) was showed. The behavior simulated were not consistent with the experimental data. This was explained by the omission in the model of the reactions describing the penning effect. Nevertheless, the simulated results confirm that the increase in the O_2/CH_4 ratio favors the production of highly oxidizing compounds such as OH and O.

The methane conversion was similar in both models. On the contrary, important differences were observed for the concentration of reaction products.

In the study carried out to understand the influence of the argon variation in the methanol selectivity, the model presented a contradictory tendency with respect to the experimental results. This was explained by the omission of reactions of the penning effect type. Despite the above, the experimental and simulated results reported present a good approximation between them.

Regarding the study of the influence of variation of the O_2/CH_4 ratio on methanol selectivity, the experimental and simulated data were in good approximation.

However, a model was developed that laid the basis for the understanding of POM for the production of methanol, which opens the door to opportunities for improvement in selectivity of methanol and future studies of research.

Outlooks

The work described in this thesis lays the basis for the conception of the future milli-structured plasma reactors to be used for partial oxidation of methane into methanol.

Modeling tools have proved to constitute an interesting tool to understand the different phenomena taking place in the plasma millireactor and the influence of the main parameters. However It is advisable to perform a more in-depth study of the influence of energy transfer reactions (Penning type). The incorporation of this kind of reactions into the DBD plasma model is required for the improvement of the predictive capacity of the model.

Considering the fragility of methanol and the necessity to maintain a low O_2/CH_4 ratio, milli-structured plasma millireactors could be of great interest if they are conceived in order to (i) extract continuously the produced methanol to avoid its destruction in the plasma reactive medium and (ii) distribute evenly the oxygen along the millireactor. Because the plasma millireactor works at ambient pressure and temperature, absorption in a liquid phase or adsorption in a solid phase are possible technologies to extract the produced methanol. Gas-liquid microreactors developed in the PhD thesis of M.Zhang [61] could be for example used with this objective. As a result, the development of a reactor that possesses high control of the mass and energy transfer phenomena as well as the incorporation of in situ methanol capture technologies could considerably increase the yield per pass of methanol compared to other processes for partial oxidation of methane.

This work has however pointed out that the geometry and the operating conditions of such a plasma millireactor have to be carefully chosen to avoid the generation of non-uniform DBD discharge. The results obtained have indeed indicated that the presence of preferential paths or “hot spots” have a negative impact on the process performance.

References

- [1] B. Eliasson, W. Egli, and U. Kogelschatz, "Modelling of dielectric barrier discharge chemistry," *Pure Appl. Chem.*, vol. 66, no. 6, pp. 1275–1286, 2009.
- [2] S.-S. Kim, J. Kim, H. Lee, B.-K. Na, and H. K. Song, "Methane conversion over nanostructured Pt/ γ -Al₂O₃ catalysts in dielectric-barrier discharge," *Korean J. Chem. Eng.*, vol. 22, no. 4, pp. 585–590, Jul. 2005.
- [3] M. R. Rahimpour, A. Jahanmiri, P. Rostami, H. Taghvaei, and B. C. Gates, "Upgrading of Anisole in a Catalytic Pulsed Dielectric Barrier Discharge Plasma Reactor," *Energy Fuels*, vol. 27, no. 12, pp. 7424–7431, décembre 2013.
- [4] C. D. Bie *et al.*, "Dielectric barrier discharges used for the conversion of greenhouse gases: modeling the plasma chemistry by fluid simulations," *Plasma Sources Sci. Technol.*, vol. 20, no. 2, p. 024008, 2011.
- [5] a. hA. H. Younger, "Introduction. En Natural gas processing principles and technology," University of Calgary, Calgary, 2004.
- [6] "Statistical Review of World Energy | Energy economics | BP Global," *bp.com*, 2015. [Online]. Available: <http://www.bp.com/en/global/corporate/energy-economics/statistical-review-of-world-energy.html>. [Accessed: 30-Nov-2016].
- [7] K. E. Trenberth, J. T. Fasullo, and J. Kiehl, "Earth's Global Energy Budget," *Bull. Am. Meteorol. Soc.*, vol. 90, no. 3, pp. 311–323, Mar. 2009.
- [8] Environmental Defense Fund, "Methane: The other important greenhouse gas," *Environmental Defense Fund*, 2016. [Online]. Available: <https://www.edf.org/methane-other-important-greenhouse-gas>. [Accessed: 26-Jan-2017].
- [9] Global Carbon Project of Future Earth, "Une hausse inexpiquée du taux de méthane dans l'atmosphère," 2012. [Online]. Available: <http://www.futura-sciences.com/planete/actualites/terre-hausse-inexpliquee-taux-methane-atmosphere-2805/>. [Accessed: 26-Jan-2017].
- [10] M. Coffey, "Energy and power generation: Maximising biogas yields from sludge," *Filtr. Sep.*, vol. 46, no. 1, pp. 12–15, Jan. 2009.
- [11] H. J. Gallon, "Dry reforming of methane using non-thermal plasma-catalysis," The University of Manchester, 2010.
- [12] European Biomass Association, "A_Biogas_Roadmap_for_Europe.pdf," 2009. [Online]. Available: http://www.seai.ie/Renewables/AD_In_Ireland_22nd_October/A_Biogas_Roadmap_for_Europe.pdf. [Accessed: 26-Jan-2017].
- [13] S. Rasi, "Biogas composition and upgrading to biomethane," *Jyvask. Stud. Biol. Environ. Sci.-9701 202*, 2009.
- [14] G. Mann, M. Schlegel, R. Schumann, A. Sakalauskas, and others, "Biogas-conditioning with microalgae," *Agron Res*, vol. 7, no. 1, pp. 33–8, 2009.
- [15] T. Fleisch, R. Sills, and M. Briscoe, "A review of global GTL developments," *J. Nat. Gas Chem.*, vol. 11, pp. 1–14, 2002.
- [16] M. Kraus, B. Eliasson, U. Kogelschatz, and A. Wokaun, "CO₂ reforming of methane by the combination of dielectric-barrier discharges and catalysis," *Phys. Chem. Chem. Phys.*, vol. 3, no. 3, pp. 294–300, Jan. 2001.
- [17] G. P. V. D. LAAN and A. C. M. BEENACKERS, "Kinetics and Selectivity of the Fischer–Tropsch Synthesis: A Literature Review," *Catal. Rev.*, vol. 41, no. 3–4, pp. 255–318, Jan. 1999.
- [18] G. P. van der Laan, "Kinetics, selectivity and scale up of the Fischer-Tropsch synthesis," s.n.], S.I., 1999.
- [19] D. J. Wilhelm, D. R. Simbeck, A. D. Karp, and R. L. Dickenson, "Syngas production for gas-to-liquids applications: technologies, issues and outlook," *Fuel Process. Technol.*, vol. 71, no. 1–3, pp. 139–148, juin 2001.

- [20] G. N. Choi, S. J. Kramer, S. S. Tam, and F. JM III, "Design and economics of a Fischer-Tropsch plant for converting natural gas to liquid transportation fuels," in *Fuel and Energy Abstracts*, 1997, vol. 38, pp. 222–222.
- [21] s Strelzoff, "Symposium Serie," *Chemical Engineering Journal*, 1970.
- [22] J. M. Fox, "The Different Catalytic Routes for Methane Valorization: An Assessment of Processes for Liquid Fuels," *Catal. Rev.*, vol. 35, no. 2, pp. 169–212, juin 1993.
- [23] K. Krawczyk, M. Młotek, B. Ulejczyk, and K. Schmidt-Szałowski, "Methane conversion with carbon dioxide in plasma-catalytic system," *Fuel*, vol. 117, pp. 608–617, Jan. 2014.
- [24] A. Indarto, "Methanol synthesis from methane and oxygen with [Ga Cr]/Cu–Zn–Al catalyst in a dielectric barrier discharge," *Ionics*, vol. 20, no. 3, pp. 445–449, Mar. 2014.
- [25] A. Indarto, "Partial oxidation of methane to methanol with nitrogen dioxide in dielectric barrier discharge plasma: experimental and molecular modeling," *Plasma Sources Sci. Technol.*, vol. 25, no. 2, p. 025002, Apr. 2016.
- [26] A. Indarto, "A review of direct methane conversion to methanol by dielectric barrier discharge," *IEEE Trans. Dielectr. Electr. Insul.*, vol. 15, no. 4, pp. 1038–1043, 2008.
- [27] E. G. Derouane, V. Parmon, F. Lemos, and F. R. Ribeiro, *Sustainable Strategies for the Upgrading of Natural Gas: Fundamentals, Challenges, and Opportunities*. Springer Science & Business Media, 2006.
- [28] G. A. Olah, "Beyond Oil and Gas: The Methanol Economy," *Angew. Chem. Int. Ed.*, vol. 44, no. 18, pp. 2636–2639, avril 2005.
- [29] A. Fridman, *Plasma Chemistry*. Cambridge University Press, 2008.
- [30] B. Graham, "Technological plasmas," *Phys. World*, vol. 14, no. 3, p. 31, 2001.
- [31] B. Eliasson and U. Kogelschatz, "Nonequilibrium volume plasma chemical processing," *IEEE Trans. Plasma Sci.*, vol. 19, no. 6, pp. 1063–1077, décembre 1991.
- [32] L. Tonks, "The Birth of 'Plasma,'" *Am. J. Phys.*, vol. 35, no. 9, pp. 857–858, Sep. 1967.
- [33] H. Rauscher, ssimo Perucca, and G. Buyle, Eds., "Front Matter," in *Plasma Technology for Hyperfunctional Surfaces*, Wiley-VCH Verlag GmbH & Co. KGaA, 2010, pp. I–XXV.
- [34] U. Kogelschatz, B. Eliasson, and W. Egli, "From ozone generators to flat television screens: history and future potential of dielectric-barrier discharges," *Pure Appl. Chem.*, vol. 71, no. 10, pp. 1819–1828, 2009.
- [35] U. Kogelschatz, "Filamentary, patterned, and diffuse barrier discharges," *IEEE Trans. Plasma Sci.*, vol. 30, no. 4, pp. 1400–1408, 2002.
- [36] A. Fridman and L. A. Kennedy, *Plasma Physics and Engineering*. CRC Press, 2004.
- [37] R. Hippler, S. Pfau, M. Schmidt, and K. H. Schoenbach, *Low Temperature Plasma Physics: Fundamental Aspects and Applications*. 2001.
- [38] H. Conrads and M. Schmidt, "Plasma generation and plasma sources," *Plasma Sources Sci. Technol.*, vol. 9, no. 4, p. 441, 2000.
- [39] J. S. Chang, P. A. Lawless, and T. Yamamoto, "Corona discharge processes," *IEEE Trans. Plasma Sci.*, vol. 19, no. 6, pp. 1152–1166, décembre 1991.
- [40] U. Kogelschatz, "Filamentary, patterned, and diffuse barrier discharges," *IEEE Trans. Plasma Sci.*, vol. 30, no. 4, pp. 1400–1408, août 2002.
- [41] T. C. Manley, "The Electric Characteristics of the Ozonator Discharge," *Trans. Electrochem. Soc.*, vol. 84, no. 1, pp. 83–96, Oct. 1943.
- [42] K. Takaki, K. Nawa, S. Mukaigawa, T. Fujiwara, and T. Aizawa, "Self-organization of microgap dielectric-barrier discharge in gas flow," *IEEE Trans. Plasma Sci.*, vol. 36, no. 4, p. 1260, 2008.
- [43] Y. Yang, Y. I. Cho, G. Friedman, A. Fridman, and G. Fridman, "Self-Organization and Migration of Dielectric Barrier Discharge Filaments in Argon Gas Flow," *IEEE Trans. Plasma Sci. IEEE Nucl. Plasma Sci. Soc.*, vol. 39, no. 11, pp. 2060–2061, May 2011.
- [44] A. Ağiral, T. Nozaki, M. Nakase, S. Yuzawa, K. Okazaki, and J. G. E. (Han) Gardeniers, "Gas-to-liquids process using multi-phase flow, non-thermal plasma microreactor," *Chem. Eng. J.*, vol. 167, no. 2–3, pp. 560–566, Mar. 2011.
- [45] T. Nozaki, A. Hattori, and K. Okazaki, "Partial oxidation of methane using a microscale non-

- equilibrium plasma reactor," *Catal. Today*, vol. 98, no. 4, pp. 607–616, décembre 2004.
- [46] M. Okumoto and A. Mizuno, "Conversion of methane for higher hydrocarbon fuel synthesis using pulsed discharge plasma method," *Catal. Today*, vol. 71, no. 1–2, pp. 211–217, Nov. 2001.
- [47] L. M. Zhou, B. Xue, U. Kogelschatz, and B. Eliasson, "Partial Oxidation of Methane to Methanol with Oxygen or Air in a Nonequilibrium Discharge Plasma," *Plasma Chem. Plasma Process.*, vol. 18, no. 3, pp. 375–393, Dec. 1997.
- [48] D. W. Larkin, L. L. Lobban, and R. G. Mallinson, "The direct partial oxidation of methane to organic oxygenates using a dielectric barrier discharge reactor as a catalytic reactor analog," *Catal. Today*, vol. 71, no. 1–2, pp. 199–210, Nov. 2001.
- [49] M. Okumoto, Z. Su, S. Katsura, and A. Mizuno, "Dilution effect with inert gas in direct methanol synthesis from methane using nonthermal plasma," in *Conference Record of the 1997 IEEE Industry Applications Conference, 1997. Thirty-Second IAS Annual Meeting, IAS '97, 1997*, vol. 3, pp. 2027–2031 vol.3.
- [50] F. M. Aghamir, N. S. Matin, A. H. Jalili, M. H. Esfarayeni, M. A. Khodagholi, and R. Ahmadi, "Conversion of methane to methanol in an ac dielectric barrier discharge," *Plasma Sources Sci. Technol.*, vol. 13, no. 4, p. 707, 2004.
- [51] R. Mooday, "Methanol production by direct oxidation of methane in a plasma reactor," Aug. 1998.
- [52] M. Okumoto, H. H. Kim, K. Takashima, S. Katsura, and A. Mizuno, "Reactivity of methane in nonthermal plasma in the presence of oxygen and inert gases at atmospheric pressure," *IEEE Trans. Ind. Appl.*, vol. 37, no. 6, pp. 1618–1624, Nov. 2001.
- [53] A. Indarto, J.-W. Choi, H. Lee, and H. K. Song, "Methane Conversion Using Dielectric Barrier Discharge: Comparison with Thermal Process and Catalyst Effects," *J. Nat. Gas Chem.*, vol. 15, pp. 87–92, 2006.
- [54] O. Guaitella, "Nature de la synergie plasma-photocatalyseur pour la destruction d'un composé organique volatil type - Thesis," ECOLE POLYTECHNIQUE, 2010.
- [55] Princeton Instruments, "ICCD: The Ultimate in Scientific ICCD Technology," 2013. [Online]. Available: <http://www.princetoninstruments.com/products/PI-MAX4-emICCD>. [Accessed: 30-Dec-2016].
- [56] S. Jones, "Understanding Gas Chromatography- Whats is really going on inside the box," 11-Feb-2009. [Online]. Available: <http://www.agilent.com/en-us/library/literature?Ntt=gas%20chromatography&redirect=0>. [Accessed: 30-Dec-2016].
- [57] P. J. Baugh, *Gas chromatography: a practical approach*. IRL Press at Oxford University Press, 1993.
- [58] D. K. Maurya, A. Sardarinejad, and K. Alameh, "Recent Developments in R.F. Magnetron Sputtered Thin Films for pH Sensing Applications—An Overview," *Coatings*, vol. 4, no. 4, pp. 756–771, Dec. 2014.
- [59] "what_is_sputtering magnetron." Micromagnetics, 2012.
- [60] T. Schmidtová, P. Souček, P. Vašina, and J. Schäfer, "Study of hybrid PVD–PECVD process of Ti sputtering in argon and acetylene," *Surf. Coat. Technol.*, vol. 205, Supplement 2, pp. S299–S302, juillet 2011.
- [61] M. Zhang, "Développement d'un microreacteur plasma pour la synthèse chimique," Université Pierre et Marie Curie, 2016.
- [62] R. Hackam, "Total secondary ionization coefficients and breakdown potentials of hydrogen, methane, ethylene, carbon monoxide, nitrogen, oxygen and carbon dioxide between mild steel coaxial cylinders," *J. Phys. B At. Mol. Phys.*, vol. 2, no. 2, p. 216, 1969.
- [63] B. Wang, W. Yan, W. Ge, and X. Duan, "Methane conversion into higher hydrocarbons with dielectric barrier discharge micro-plasma reactor," *J. Energy Chem.*, vol. 22, no. 6, pp. 876–882, Nov. 2013.
- [64] A. A. Khassin, B. L. Pietruszka, M. Heintze, and V. N. Parmon, "Methane oxidation in a dielectric barrier discharge. the impact of discharge power and discharge gap filling," *React. Kinet. Catal. Lett.*, vol. 82, no. 1, pp. 111–119.

- [65] T. Nozaki, A. Ağiral, S. Yuzawa, J. G. E. Han Gardeniers, and K. Okazaki, "A single step methane conversion into synthetic fuels using microplasma reactor," *Chem. Eng. J.*, vol. 166, no. 1, pp. 288–293, Jan. 2011.
- [66] N. Rueangjitt, T. Sreethawong, S. Chavadej, and H. Sekiguchi, "Non-Oxidative Reforming of Methane in a Mini-Gliding Arc Discharge Reactor: Effects of Feed Methane Concentration, Feed Flow Rate, Electrode Gap Distance, Residence Time, and Catalyst Distance," *Plasma Chem. Plasma Process.*, vol. 31, no. 4, pp. 517–534, Apr. 2011.
- [67] M. J. Kushner, "Hybrid modelling of low temperature plasmas for fundamental investigations and equipment design," *J. Phys. Appl. Phys.*, vol. 42, no. 19, p. 194013, Oct. 2009.
- [68] N. Y. Babaeva and M. J. Kushner, "Ion energy and angular distributions onto polymer surfaces delivered by dielectric barrier discharge filaments in air: I. Flat surfaces," *Plasma Sources Sci. Technol.*, vol. 20, no. 3, p. 035017, Jun. 2011.
- [69] Y. Zhuang, G. Chen, and M. Rotaru, "Numerical modelling of needle-grid electrodes for negative surface corona charging system," *J. Phys. Conf. Ser.*, vol. 310, p. 012011, Aug. 2011.
- [70] C. J. Umeozor, "Computer simulation of the methane plasma enhanced deposition of carbon film," University of Missouri–Columbia, 2013.
- [71] K. Nagayama, B. Farouk, and Y. H. Lee, "Neutral and charged particle simulation of a RF argon plasma," *Plasma Sources Sci. Technol.*, vol. 5, no. 4, p. 685, 1996.
- [72] G. J. M. Hagelaar and L. C. Pitchford, "Solving the Boltzmann equation to obtain electron transport coefficients and rate coefficients for fluid models," *Plasma Sources Sci. Technol.*, vol. 14, no. 4, p. 722, 2005.
- [73] COMSOL Multiphysics, "Dielectric Barrier Discharge, Plasma Module." 2010.
- [74] R. J. Kee, M. E. Coltrin, and P. Glarborg, *Chemically Reacting Flow: Theory and Practice*. John Wiley & Sons, 2005.
- [75] V. Goujard, T. Nozaki, S. Yuzawa, A. Ağiral, and K. Okazaki, "Plasma-assisted partial oxidation of methane at low temperatures: numerical analysis of gas-phase chemical mechanism," *J. Phys. Appl. Phys.*, vol. 44, no. 27, p. 274011, 2011.
- [76] S. Jo, D. Hoon Lee, and Y.-H. Song, "Product analysis of methane activation using noble gases in a non-thermal plasma," *Chem. Eng. Sci.*, vol. 130, pp. 101–108, Jul. 2015.

Annex I: Electrical characterization of the electrodes

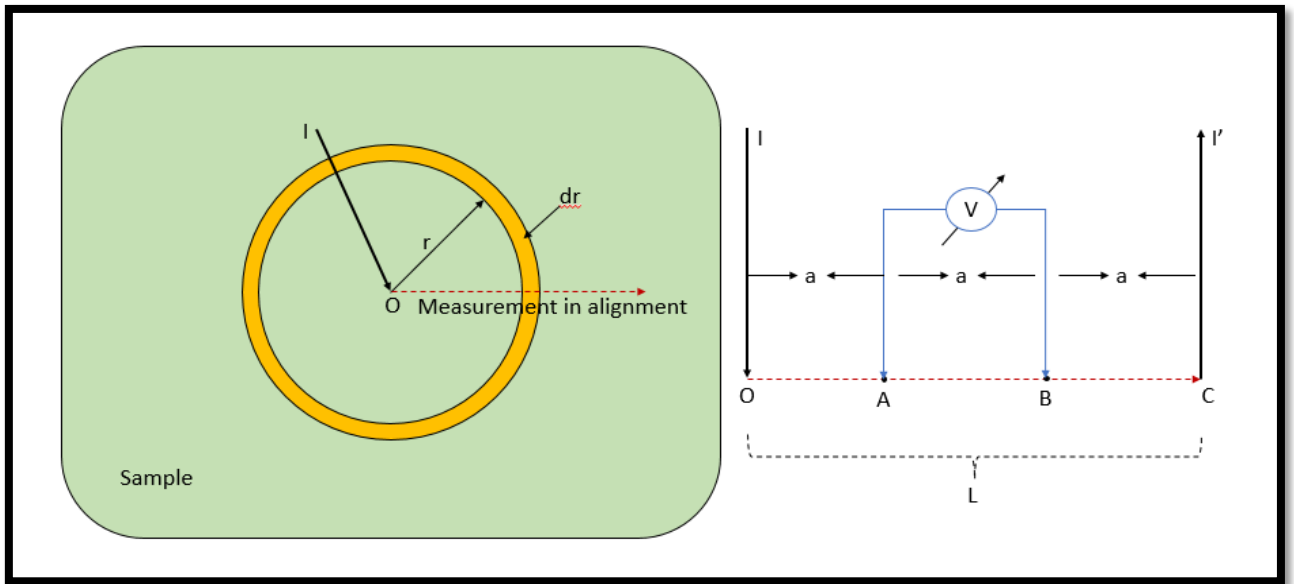


Figure A1.1. Scheme of the methodology for the determination of resistivity in a flat surface material.

A flat conductive sample of infinite extent is assumed, the thickness is E and its resistivity is ρ , as shown in figure A1.1. It is assumed that a current I is injected at one point in the sample. It is considered that by symmetry the current is evenly distributed in all directions of the sample. Thus, the potential difference between two points separated by a distance r from the injection point will be defined by the equation 3.1:

$$dV = I dR \quad \text{Eq. 3.1}$$

R is a measure of the difficulty to pass an electric current through that conductor. It is defined in equation 3.2, where ρ is the resistivity that is an intrinsic property that quantifies how strongly a given material opposes to the flow of electric current, L is the length of the piece material and A is the cross-sectional area of the sample.

$$R = \rho \frac{L}{A} \quad \text{Eq. 3.2}$$

For the case presented in figure A1.1 L and A are defined as equation 3.3 and 3.4 report;

$$L = r \quad \text{Eq. 3.3}$$

$$A = 2\pi r E \quad \text{Eq. 3.4}$$

The differential equation which predicts the voltage behavior is described below :

$$dV = I \frac{\rho}{E2\pi} \frac{dr}{r} \quad \text{Eq. 3.5}$$

The integration of equation 3.5 limited by the points A and B is described as follows:

$$(V_A - V_B)' = I \frac{\rho}{E2\pi} \text{Ln} \left(\frac{b}{a} \right) \quad \text{Eq. 3.6}$$

The equation 3.6 describes the difference of voltage between the point A and B which have a distance a and b from the current injection point O. In the other hand, if there is the same current extraction in the point C which correspond to a distance L from O, the difference in voltage between the points A and B will be the equation 3.7;

$$(V_A - V_B)'' = I \frac{\rho}{E2\pi} \text{Ln} \left(\frac{L-b}{L-a} \right) \quad \text{Eq. 3.7}$$

If the injection and extraction of the current are at the same time (Equilibrium condition) the tension between the points A and B is described in Equation 3.8.

$$(V_A - V_B) = I \frac{\rho}{E2\pi} \text{Ln} \left(\frac{b(L-a)}{a(L-b)} \right) \quad \text{Eq.3.8}$$

The points O, A, B, C are equidistant therefore;

$$A = a$$

$$B = 2a$$

$$C = 3a$$

Equation 3.8 is reduced to:

$$(V_A - V_B) = I \frac{\rho}{E\pi} \text{Ln}(2) \quad ; \quad \rho = \frac{\Delta V}{I} \frac{E\pi}{\text{Ln}(2)} \quad \text{Eq. 3.9}$$

Therefore, in a flat geometry and with electrodes equidistant and separated by a distance $a \gg E$, as shown in Figure 3.6, the resistivity of the sample can be extracted from the measurement of the injection current I and the measurement of the potential difference ΔV , as indicated by equation 3.9.

A current of 0.8 amperes was passed through the sample and the tension was measured at equidistant points as shown in Figure A1.1. The thickness was measured by optical profilometer technique. The results for the materials deposited for the reactor

are shown in Table A1.1.

Table A1.1 Resistivity and Thickness values for the materials used for the manufacture of the electrodes.

Material	Resistivity (S)	Thickness (nm)
ITO+GOLD	2.52e6	150
GOLD	4.3e7	300

Annex II DBD plasma model parameters

In table A2.1 are reported the reactions and variables used for the simulation of the DBD plasma model in COMSOL Multiphysics 5.1. It is important to note that the cross-section values were calculated with the software bolsig +.

Table A2.1.- Reactions and variables used for the simulation of the DBD plasma model

#	Reaction	Type of reaction	Variable
1	Ar + e => Ar + e	Elastic	$m_r = 0.136E-4$
2	Ar + e => Ar ^s + e	Excitation	$\Delta\epsilon = 11.5 \text{ eV}$
3	Ar ^s + e => Ar + e	Excitation	$\Delta\epsilon = -11.5 \text{ eV}$
4	Ar + e => Ar ⁺ + 2e	Ionization	$\Delta\epsilon = 15.8 \text{ eV}$
5	Ar + e => Ar ⁺ + 2e	Ionization	$\Delta\epsilon = 4.427 \text{ eV}$
6	O ₂ + e => e + O ₂	Elastic	$m_r = 1.71E-5$
7	O ₂ + e => O + O ⁻	Attachment	-----
8	e + O ₂ => e + O ₂	Excitation	$\Delta\epsilon = 0.02 \text{ eV}$
9	e + O ₂ => e + O ₂	Excitation	$\Delta\epsilon = 0.19 \text{ eV}$
10	e + O ₂ => e + O ₂	Excitation	$\Delta\epsilon = 0.19 \text{ eV}$
11	e + O ₂ => e + O ₂	Excitation	$\Delta\epsilon = 0.38 \text{ eV}$
12	e + O ₂ => e + O ₂	Excitation	$\Delta\epsilon = 0.38 \text{ eV}$
13	e + O ₂ => e + O ₂	Excitation	$\Delta\epsilon = 0.57 \text{ eV}$
14	e + O ₂ => e + O ₂	Excitation	$\Delta\epsilon = 0.75 \text{ eV}$
15	e + O ₂ => e + O ₂ a1d	Excitation	$\Delta\epsilon = 0.977 \text{ eV}$
16	e + O ₂ a1d => e + O ₂	Excitation	$\Delta\epsilon = -0.977 \text{ eV}$
17	e + O ₂ => e + O ₂ b1s	Excitation	$\Delta\epsilon = 1.627 \text{ eV}$
18	e + O ₂ b1s => e + O ₂	Excitation	$\Delta\epsilon = -1.627 \text{ eV}$
19	e + O ₂ => e + O + O	Excitation	$\Delta\epsilon = 6 \text{ eV}$
20	e + O ₂ => e + O + O1d	Excitation	$\Delta\epsilon = 8.4 \text{ eV}$
21	e + O ₂ => 2e + O ₂ ⁺	Ionization	$\Delta\epsilon = 12.06 \text{ eV}$
22	e + CH ₄ => CH ₃ + H ⁻	Attachment	-----
23	e + CH ₄ => H ₂ + CH ₂ ⁻	Attachment	-----
24	e + CH ₄ => e + CH ₄	Elastic	$m_r = 3.424 \text{ E-5}$
25	e + CH ₄ => e + CH ₄ s	Excitation	$\Delta\epsilon = 9 \text{ eV}$
26	e + CH ₄ => e + CH ₄ s	Excitation	$\Delta\epsilon = 10 \text{ eV}$
27	e + CH ₄ => e + CH ₄ s	Excitation	$\Delta\epsilon = 11 \text{ eV}$
28	e + CH ₄ => e + CH ₄ s	Excitation	$\Delta\epsilon = 12 \text{ eV}$
29	e + CH ₄ => 2e + CH ₄ ⁺	Ionization	$\Delta\epsilon = 12.6 \text{ eV}$
30	e + CH ₄ => 2e + H + CH ₃ ⁺	Ionization	$\Delta\epsilon = 14.3 \text{ eV}$
31	e + H ₂ => e + H ₂	Elastic	$m_r = 2.72E-4$
32	e + CH ₄ => e + H + CH ₃	Excitation	$\Delta\epsilon = 7 \text{ eV}$
33	e + CH ₄ => CH ₂ + H ₂ + e	Excitation	$\Delta\epsilon = 7 \text{ eV}$
34	e + C ₂ H ₆ => C ₂ H ₆ ⁻	Attachment	-----
35	e + C ₂ H ₆ => e + C ₂ H ₆	Elastic	$m_r = 1.823E-5$
36	e + C ₂ H ₆ => 2e + C ₂ H ₆ ⁺	Ionization	$\Delta\epsilon = 12.7 \text{ eV}$
37	e + CH ₂ => 2e + H + CH ⁺	Ionization	$\Delta\epsilon = 16 \text{ eV}$
38	e + CO => e + CO	Elastic	$m_r = 1.957E-5$
39	e + CO => e + C + O	Excitation	$\Delta\epsilon = 13.5 \text{ eV}$
40	e + CO => 2e + CO ⁺	Ionization	$\Delta\epsilon = 14.01 \text{ eV}$
41	e + CO ₂ => CO + O ⁻	Attachment	-----
42	e + CO ₂ => e + CO ₂	Elastic	$m_r = 1.24E-5$
43	e + CO ₂ => 2e + CO ₂ ⁺	Ionization	$\Delta\epsilon = 13.3 \text{ eV}$
44	e + H => e + H	Elastic	$m_r = 5.48193 \text{ E-4}$
45	e + H => 2e + H ⁺	Ionization	$\Delta\epsilon = 13.6 \text{ eV}$

46	$e + H_2 \Rightarrow 2e + H_2^+$	Ionization	$\Delta\epsilon = 15.4 \text{ eV}$
47	$e + H_2O \Rightarrow H_2^+ + O^-$	Attachment	-----
48	$e + H_2O \Rightarrow H^- + OH$	Attachment	-----
49	$e + H_2O \Rightarrow OH^- + H$	Attachment	-----
50	$e + H_2O \Rightarrow e + H_2O$	Elastic	$m_r = 3.043 \text{ E-5}$
51	$e + H_2O \Rightarrow e + H + OH$	Excitation	$\Delta\epsilon = 7 \text{ eV}$
52	$Ars + Ars \Rightarrow e + Ar + Ar^+$	Arrhenius	$k^f = 3.3734 \text{ E8}$ $m^3/(s^*mol)$
53	$Ars + Ar \Rightarrow Ar + Ar$	Arrhenius	$k^f = 1807 \text{ E8 } m^3/(s^*mol)$
54	$O + O \Rightarrow O_2$	Arrhenius	$k^f = 1 \text{ E4 } m^3/(s^*mol)$
55	$H + H \Rightarrow H_2$	Arrhenius	$k^f = 3 \text{ E4 } m^3/(s^*mol)$
56	$CH_3 + CH_3 \Rightarrow C_2H_6$	Arrhenius	$k^f = 5 \text{ E7 } m^3/(s^*mol)$
57	$CH_3 + CH_2 \Rightarrow C_2H_4 + H$	Arrhenius	$k^f = 3 \text{ E7 } m^3/(s^*mol)$
58	$CH_4 + O_1d \Rightarrow CH_3 + OH$	Arrhenius	$k^f = 8.4 \text{ E7 } m^3/(s^*mol)$
59	$CH_4 + O \Rightarrow CH_3 + OH$	Arrhenius	$k^f = 500 \text{ } m^3/(s^*mol)$
60	$CH_4 + OH \Rightarrow CH_3 + H_2O$	Arrhenius	$k^f = 100 \text{ } m^3/(s^*mol)$
61	$CH_3 + O_2 \Rightarrow CH_3O_2$	Arrhenius	$k^f = 240000 \text{ } m^3/(s^*mol)$
62	$CH_3 + O \Rightarrow CH_2O + H$	Arrhenius	$k^f = 8 \text{ E7 } m^3/(s^*mol)$
63	$CH_3 + O \Rightarrow CHO + H_2$	Arrhenius	$k^f = 6 \text{ E7 } m^3/(s^*mol)$
64	$CH_3 + CH_3O_2 \Rightarrow CH_3O + CH_3O$	Arrhenius	$k^f = 2 \text{ E7 } m^3/(s^*mol)$
65	$CH_3O_2 + H \Rightarrow CH_3O + OH$	Arrhenius	$k^f = 7 \text{ E7 } m^3/(s^*mol)$
66	$CH_3O_2 + O \Rightarrow CH_3O + O_2$	Arrhenius	$k^f = 2.4 \text{ E7 } m^3/(s^*mol)$
67	$CH_3O_2 + OH \Rightarrow CH_3OH + O_2$	Arrhenius	$k^f = 5 \text{ E4 } m^3/(s^*mol)$
68	$CH_3O_2 + CH_3O_2 \Rightarrow 2CH_3O + O_2$	Arrhenius	$k^f = 1 \text{ E5 } m^3/(s^*mol)$
69	$CH_3O + O_2 \Rightarrow CH_2O + HO_2$	Arrhenius	$k^f = 1.5 \text{ E3 } m^3/(s^*mol)$
70	$CH_3O + H \Rightarrow CH_2O + H_2$	Arrhenius	$k^f = 2 \text{ E7 } m^3/(s^*mol)$
71	$CH_3O + O \Rightarrow CH_2O + OH$	Arrhenius	$k^f = 3 \text{ E6 } m^3/(s^*mol)$
72	$CH_3O + O \Rightarrow CH_3 + O_2$	Arrhenius	$k^f = 1 \text{ E7 } m^3/(s^*mol)$
73	$CH_3O + CH_3O \Rightarrow CH_3OH + CH_2O$	Arrhenius	$k^f = 2 \text{ E7 } m^3/(s^*mol)$
74	$CH_2O + O \Rightarrow CHO + OH$	Arrhenius	$k^f = 6 \text{ E7 } m^3/(s^*mol)$
75	$CH_2O + OH \Rightarrow CHO + H_2O$	Arrhenius	$k^f = 5 \text{ E6 } m^3/(s^*mol)$
76	$CH_2O + H \Rightarrow H_2 + CHO$	Arrhenius	$k^f = 2.4 \text{ E5 } m^3/(s^*mol)$
77	$CH_2 + O_2 \Rightarrow CO + H_2O$	Arrhenius	$k^f = 2 \text{ E6 } m^3/(s^*mol)$
78	$CH_2 + O \Rightarrow CO + H + H$	Arrhenius	$k^f = 3 \text{ E7 } m^3/(s^*mol)$
79	$CHO + O_2 \Rightarrow CO_2 + OH$	Arrhenius	$k^f = 6 \text{ E5 } m^3/(s^*mol)$
80	$CHO + O_2 \Rightarrow CO + HO_2$	Arrhenius	$k^f = 3 \text{ E6 } m^3/(s^*mol)$
81	$CHO + O \Rightarrow CO_2 + H$	Arrhenius	$k^f = 3 \text{ E7 } m^3/(s^*mol)$
82	$CHO + O \Rightarrow CO + OH$	Arrhenius	$k^f = 3 \text{ E7 } m^3/(s^*mol)$
83	$CHO + OH \Rightarrow CO + H_2O$	Arrhenius	$k^f = 3 \text{ E7 } m^3/(s^*mol)$
84	$CH + O_2 \Rightarrow CO_2 + H$	Arrhenius	$k^f = 2.4 \text{ E7 } m^3/(s^*mol)$
85	$CH + O_2 \Rightarrow CO + OH$	Arrhenius	$k^f = 8.4 \text{ E7 } m^3/(s^*mol)$
86	$CH + O \Rightarrow CO + H$	Arrhenius	$k^f = 4 \text{ E7 } m^3/(s^*mol)$
87	$CO + OH \Rightarrow CO_2 + H$	Arrhenius	$k^f = 6 \text{ E5 } m^3/(s^*mol)$
88	$CH + H_2 \Rightarrow CH_2 + H$	Arrhenius	$k^f = 1.4 \text{ E6 } m^3/(s^*mol)$
89	$HO_2 + O \Rightarrow O_2 + OH$	Arrhenius	$k^f = 3.7 \text{ E6 } m^3/(s^*mol)$
90	$HO_2 + H \Rightarrow O_2 + H_2$	Arrhenius	$k^f = 5 \text{ E6 } m^3/(s^*mol)$
91	$HO_2 + H \Rightarrow OH + OH$	Arrhenius	$k^f = 5 \text{ E7 } m^3/(s^*mol)$
92	$HO_2 + OH \Rightarrow O_2 + H_2O$	Arrhenius	$k^f = 3 \text{ E7 } m^3/(s^*mol)$
93	$HO_2 + CH_3 \Rightarrow CH_3O + OH$	Arrhenius	$k^f = 2 \text{ E7 } m^3/(s^*mol)$
94	$CH_3OH + O \Rightarrow CH_3O + OH$	Arrhenius	$k^f = 1.2 \text{ E4 } m^3/(s^*mol)$
95	$H_2O + CH \Rightarrow CH_2O + H$	Arrhenius	$k^f = 1 \text{ E7 } m^3/(s^*mol)$
96	$OH + CH_3 \Rightarrow CH_3OH$	Arrhenius	$k^f = 6 \text{ E5 } m^3/(s^*mol)$
97	$Ar^+ \Rightarrow Ar$	Attachment	$\gamma_k = 1e-6$; $\bar{\epsilon}_k = 2.5 \text{ eV}$;

		coefficient	
98	Ar ⁺ => Ar	Attachment coefficient	$\gamma_k = 0.045$; $\bar{\epsilon}_k = 2.5$ eV
99	Ars => Ar	Attachment coefficient	
100	O ⁻ => O	Attachment coefficient	$\gamma_k = 0.03$; $\bar{\epsilon}_k = 2.5$ eV
101	O ⁻ => O	Attachment coefficient	$\gamma_k = 1E-6$; $\bar{\epsilon}_k = 2.5$ eV
102	O2 ⁺ => O2	Attachment coefficient	$\gamma_k = 0.03$; $\bar{\epsilon}_k = 2.5$ eV
103	O2 ⁺ => O2	Attachment coefficient	$\gamma_k = 1E-6$; $\bar{\epsilon}_k = 2.5$ eV
104	CH4s => CH4	Attachment coefficient	
105	CH4 ⁺ => CH4	Attachment coefficient	$\gamma_k = 0.035$; $\bar{\epsilon}_k = 2.5$ eV
106	CH4 ⁺ => CH4	Attachment coefficient	$\gamma_k = 1E-6$; $\bar{\epsilon}_k = 2.5$ eV
106	CH3 ⁺ => CH3	Attachment coefficient	$\gamma_k = 1E-6$; $\bar{\epsilon}_k = 2.5$ eV
107	CH3 ⁺ => CH3	Attachment coefficient	$\gamma_k = 0.03$; $\bar{\epsilon}_k = 2.5$ eV
108	CH2 ⁻ => CH2	Attachment coefficient	$\gamma_k = 0.03$; $\bar{\epsilon}_k = 2.5$ eV
109	CH2 ⁻ => CH2	Attachment coefficient	$\gamma_k = 1E-6$; $\bar{\epsilon}_k = 2.5$ eV
110	H ⁻ => H	Attachment coefficient	$\gamma_k = 1E-6$; $\bar{\epsilon}_k = 2.5$ eV
111	H ⁻ => H	Attachment coefficient	$\gamma_k = 0.02$; $\bar{\epsilon}_k = 2.5$ eV
112	C2H6 ⁺ => C2H6	Attachment coefficient	$\gamma_k = 1E-6$; $\bar{\epsilon}_k = 2.5$ eV
113	C2H6 ⁺ => C2H6	Attachment coefficient	$\gamma_k = 0.02$; $\bar{\epsilon}_k = 2.5$ eV
114	C2H6 ⁻ => C2H6	Attachment coefficient	$\gamma_k = 1E-6$; $\bar{\epsilon}_k = 2.5$ eV
115	O1d => O	Attachment coefficient	$\gamma_k = 1E-6$; $\bar{\epsilon}_k = 2.5$ eV
116	CH ⁺ => CH	Attachment coefficient	$\gamma_k = 0.02$; $\bar{\epsilon}_k = 2.5$ eV
117	CH ⁺ => CH	Attachment coefficient	$\gamma_k = 1E-6$; $\bar{\epsilon}_k = 2.5$ eV
118	CO ⁺ => CO	Attachment coefficient	$\gamma_k = 1E-6$; $\bar{\epsilon}_k = 2.5$ eV
119	CO ⁺ => CO	Attachment coefficient	$\gamma_k = 0.02$; $\bar{\epsilon}_k = 2.5$ eV
120	CO2 ⁺ => CO2	Attachment coefficient	$\gamma_k = 1E-6$; $\bar{\epsilon}_k = 2.5$ eV
121	CO2 ⁺ => CO2	Attachment coefficient	$\gamma_k = 0.02$; $\bar{\epsilon}_k = 2.5$ eV
122	H ⁺ => H	Attachment coefficient	$\gamma_k = 1E-6$; $\bar{\epsilon}_k = 2.5$ eV
123	H ⁺ => H	Attachment	$\gamma_k = 0.02$; $\bar{\epsilon}_k = 2.5$ eV

		coefficient	
124	H2 ⁺ => H2	Attachment coefficient	$\gamma_k = 1E-6 ; \bar{\epsilon}_k = 2.5 \text{ eV}$
125	H2 ⁺ => H2	Attachment coefficient	$\gamma_k = 0.02 ; \bar{\epsilon}_k = 2.5 \text{ eV}$
126	OH ⁻ => OH	Attachment coefficient	$\gamma_k = 1E-6 ; \bar{\epsilon}_k = 2.5 \text{ eV}$
127	OH ⁻ => OH	Attachment coefficient	$\gamma_k = 0.02 ; \bar{\epsilon}_k = 2.5 \text{ eV}$

In table A2.2 are reported the species involved in the simulation of the DBD plasma model in COMSOL Multiphysics 5.1.

Table A2.2.- Species involved in the simulation of the DBD plasma model

e	C2H6-
Ar	C2H6+
Ars	C2H4
Ar+	CH+
O2	CH+OH
O	H2O
O-	CO
O2a1d	CO+
O2b1s	CO2
O1d	CO2+
O2+	H+
CH4	H2+
CH3	OH-
H-	CH3O2
H2	CH3OH
CH2-	CH3O
CH4s	CH2O
CH4+	HO2
H	CHO
CH3+	
CH2	
C2H6	
C	

Annex III Reaction engineering equations for multi-time scale model

COMSOL reaction set

Firstly, the reaction engineering package was used, within which the standard set of equations and parameters for the compression/ignition template were modified and adapted for the reactions within the plasma DBD microreactor:

The compression/ignition systems dependence on a piston cylinder arrangement was removed, deleting everything except the 215 reaction equations and 34 species required for this study.

In order to predict the influence of propane in the POM the following additional reactions were added into the model (R202-R207). The kinetic parameters were found in NIST Chemical Kinetics Database.

Any equations which included nitrogen or argon were disabled as they were not present in the system studied.

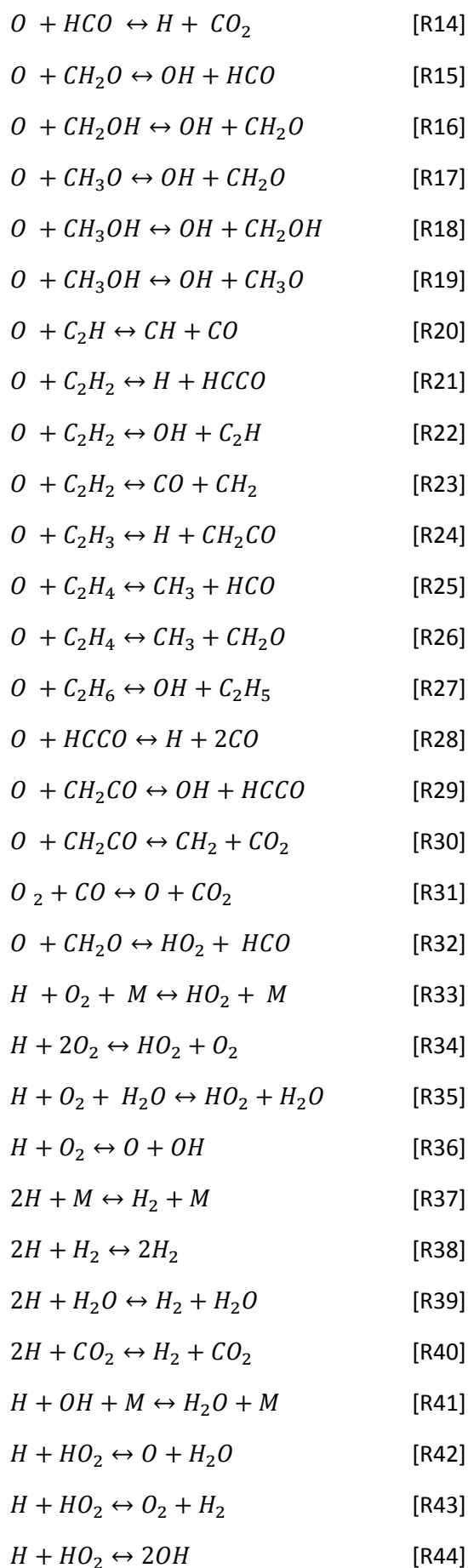
Species

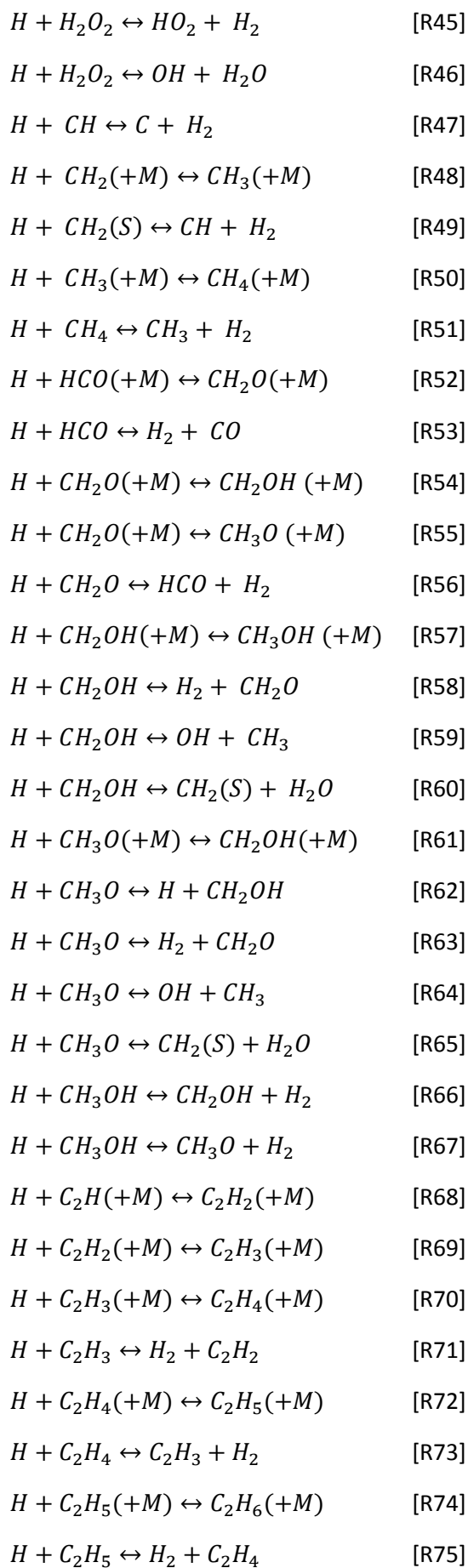
C_3H_6	[S1]
CH_2CO	[S2]
CO_2	[S3]
$HCCO$	[S4]
H_2O_2	[S5]
$CH_2(S)$	[S6]
CH_2CHO	[S7]
HO_2	[S8]
CH_3OH	[S9]
CH_4	[S10]
CH_3	[S11]
CH_2	[S12]
CH_2OH	[S13]
CH_3CHO	[S14]
C	[S15]
O	[S16]
H	[S17]
O_2	[S18]
CH_3O	[S19]

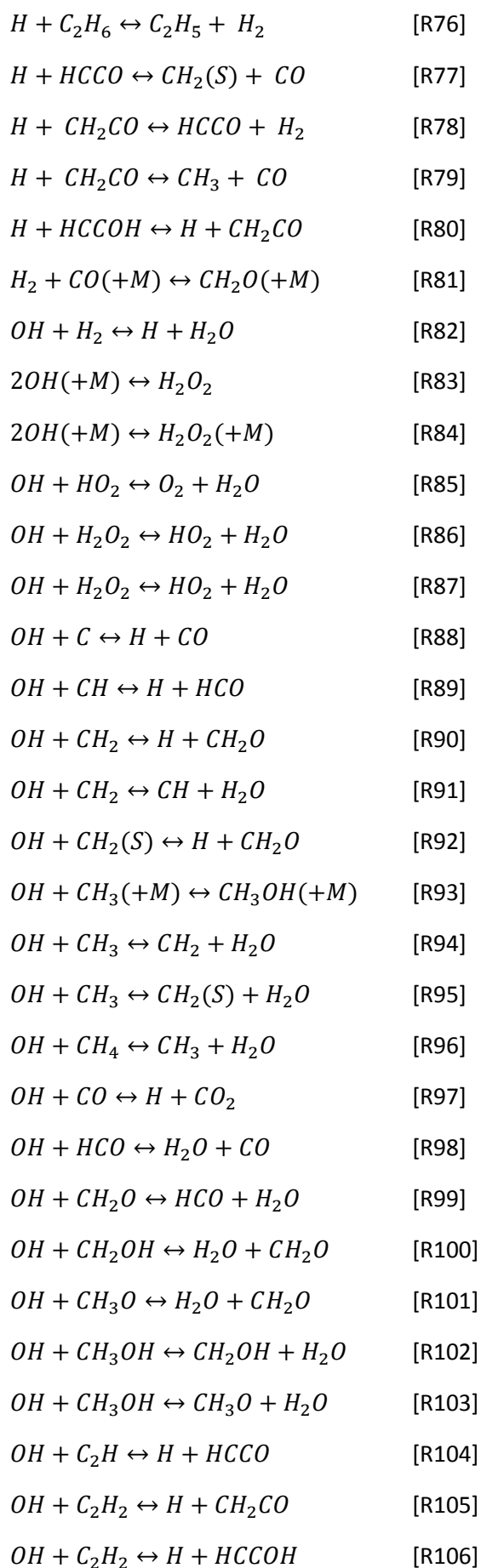
C_2H	[S20]
H_2O	[S21]
OH	[S22]
HCO	[S23]
CH_2O	[S24]
C_2H_4	[S25]
C_2H_3	[S26]
C_2H_2	[S27]
CH	[S28]
$HCCOH$	[S29]
H_2	[S30]
C_2H_6	[S31]
C_2H_5	[S32]
C_3H_7	[S33]
CO	[S34]
C_3H_8	[S35]

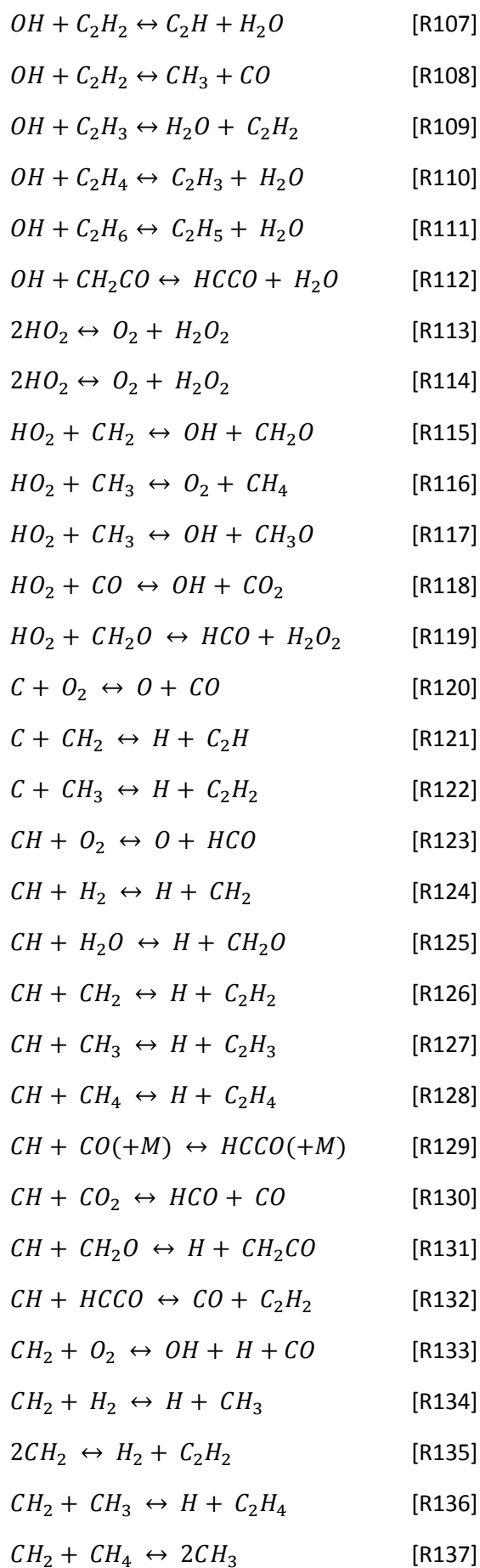
Reactions

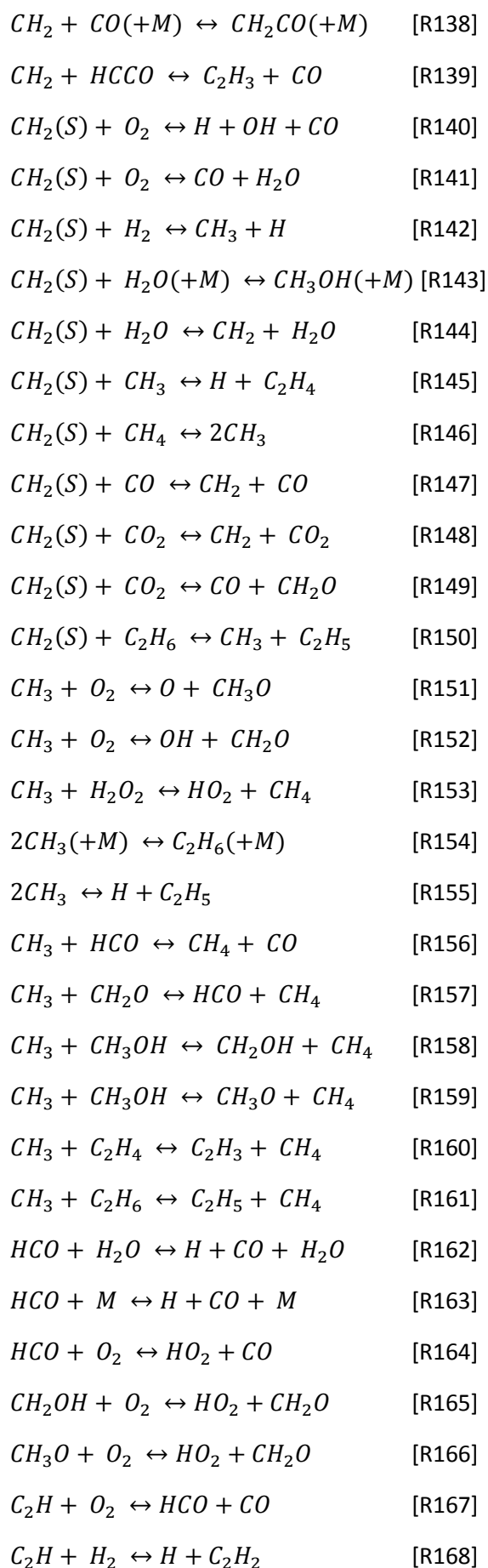
$2O + M \leftrightarrow O_2 + M$	[R1]
$O + H + M \leftrightarrow OH + M$	[R2]
$O + H_2 \leftrightarrow H + OH$	[R3]
$O + HO_2 \leftrightarrow OH + O_2$	[R4]
$O + H_2O_2 \leftrightarrow OH + HO_2$	[R5]
$O + CH \leftrightarrow H + CO$	[R6]
$O + CH_2 \leftrightarrow H + HCO$	[R7]
$O + CH_2(S) \leftrightarrow H_2 + CO$	[R8]
$O + CH_2(S) \leftrightarrow H + HCO$	[R9]
$O + CH_3 \leftrightarrow H + CH_2O$	[R10]
$O + CH_4 \leftrightarrow OH + CH_3$	[R11]
$O + CO (+M) \leftrightarrow CO_2(+M)$	[R12]
$O + HCO \leftrightarrow OH + CO$	[R13]

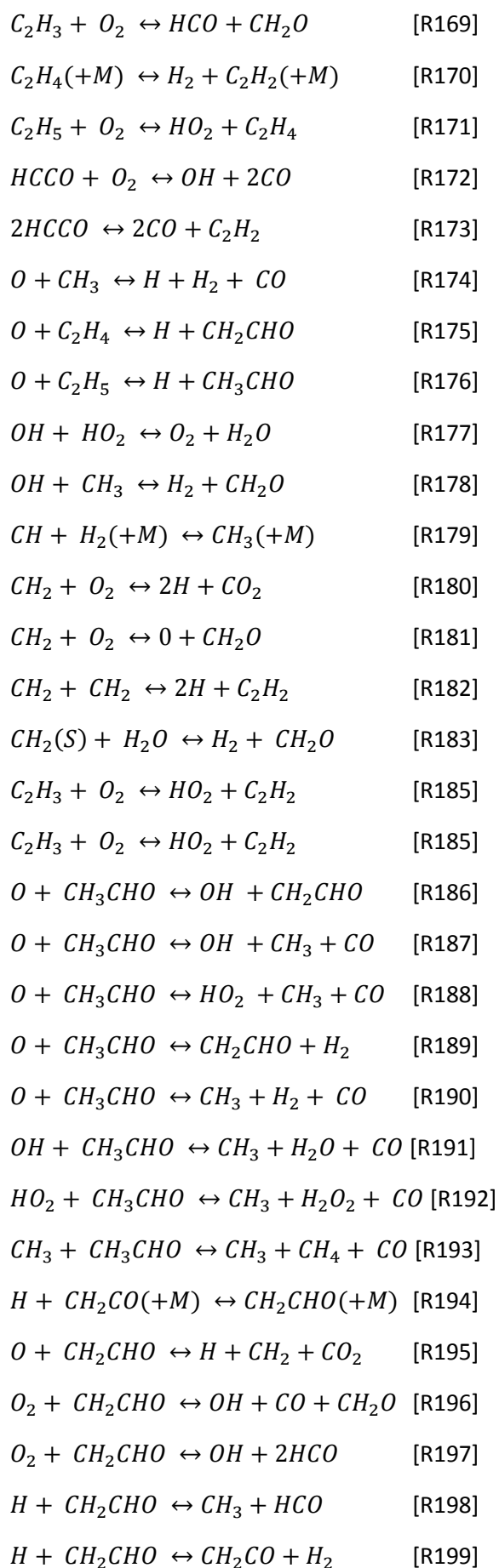


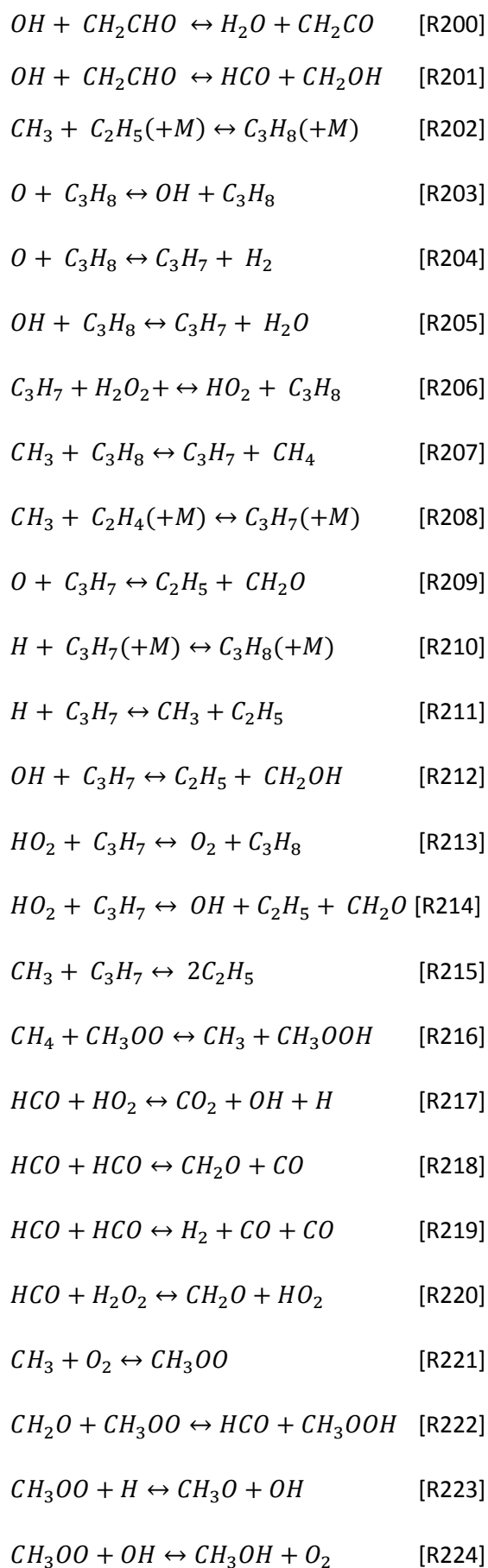


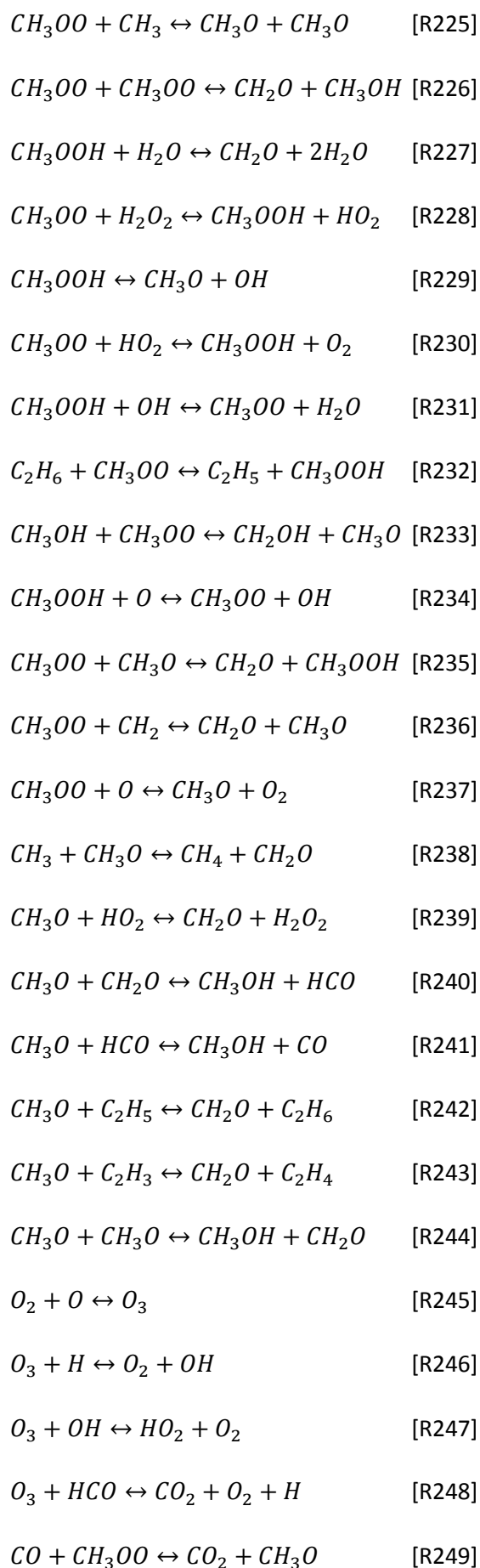


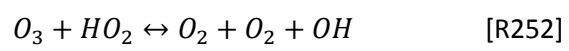
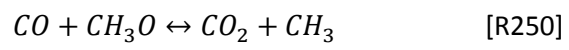












List of figures

Figure 1.1. Proven world natural gas reserves by geographical region in 2015 [6]	18
Figure 1.2. World primary energy consumption from 1990 to 2015 [6]	19
Figure 1.3. The global annual mean Earth's energy budget for the March 2000 to May 2004 period ($W m^{-2}$). The broad arrows indicate the schematic flow of energy in proportion to their importance [7].....	20
Figure 1.4. World consumption (2015) in Million tonnes oil equivalent of the energy sources [6].	21
Figure 1.5. Global methane budget in millions of tons of CH_4 per year [9].	22
Figure 1.6. Selectivity control in Fisher-Tropsch synthesis by process conditions and catalyst modifications [18].....	26
Figure 1.7. The dependence of voltage upon current for various kinds of DC discharges [38].	36
Figure 1.8. Schematic diagram of a corona discharge reactor in a coaxial wire-cylinder configuration [11].....	37
Figure 1.9. Schematic diagram of a corona discharge reactor in a point-to-plate configuration [11]....	37
Figure 1.10. Schematic diagrams showing different forms of corona discharges in a point-to-plate electrode configuration [11].	38
Figure 1.11. Schematic diagram of a gliding arc discharge reactor [11].	39
Figure 1.12. Schematic diagrams of planar, coaxial and surface DBD configurations [34].	40
Figure 1.13. Schematic diagram of the plasma DBD reactor a) [45], b) [46] c) [47]	43
Figure 1.14. Methanol selectivity behavior as a function of methane conversion reported in the literature [45], [46], [50], [51].....	45
Figure 2.1. Electric scheme utilized for the measurements of energy from Lissajous curve	51
Figure 2.2. Cross-section view of an image intensifier tube utilized in a Princeton instrument ICCD camera [55].....	52
Figure 2.3. Schematic description of a gas chromatograph.....	53
Figure 2.4. Example of a GC chromatogram of different organic compounds.....	54
Figure 2.5. A schematic diagram of a two-channel Agilent 490 micro-GC with thermal conductivity detection.	55
Figure 2.6. Gas chromatograms using Plot-U (a) and molecular sieve (b) in an Agilent 490 micro-GC with thermal conductivity detection.....	57
Figure 2.7. Schematic diagram of a typical thermal conductivity detector [57].....	58
Figure 3.1. Typical oxidation of electrode (made with copper) in presence of oxygen.	64
Figure 3.2. Principle of the multistep process investigated: (a) laser engraving, (b) electrode elaboration and (c) cellule assembly.	65
Figure 3.3. Geometry and dimensions of the plasma millireactor cellule.....	66
Figure 3.4. SEM Images at 2 mm (a) and 300 micrometers (b) of the bottoms and the roughness profile ($\Delta=140\mu m$) by mechanical profilometer (c) of the bottoms in the reactor.	67
Figure 3.5. a) Graphical diagram of the operation of Sputter deposition and b) interior view photo.	68

Figure 3.6. (a) Argon (50 sccm) discharge performed within the millichannel and (b) Transparent plasma millireactor cellule. The experiment was carried out at atmospheric pressure and room temperature (10.8 kV, 1 kHz).	72
Figure 3.7. Energy per period injected in the reactor as a function of frequency at constant tension equal to 10.8 kV, O ₂ /CH ₄ ratio equal to 0.5 (v/v) and concentration of argon equal to 0.375 (v/v)75	
Figure 3.8. Energy per period as a function of the frequency at two different values of tension for the reaction mixture for a flow rate of 48 sccm, O ₂ /CH ₄ ratio equal to 0.5 (v/v) and concentration of argon equal to 0.375 (v/v).....	76
Figure 3.9. Energy per period injected in the reactor as a function of argon concentration at constant tension, frequency, O ₂ /CH ₄ ratio and flow rate equal to 10.8 kV, 3000 Hz, 0.3 v/v and 48 sccm respectively.....	77
Figure 3.10. Energy per period injected in the reactor as a function of O ₂ /CH ₄ ratio without presence of argon at constant tension, frequency, and flow rate equal to 10.8 kV, 3000 Hz, and 48 sccm respectively.....	78
Figure 3.11. Images of the reactor channel taken with an Intensified Charge Coupled Device (ICCD) camera, they show the three different pure gases (methane, argon and oxygen) at constant power of 3 Watts and 48 sccm.	79
Figure 3.12. Images of the reactor channel taken with an Intensified Charge Coupled Device (ICCD) camera. Effect of the power (Watts) in the reactive mixture a) 2, b) 2.5, c) 3, d) 3.8 at a constant flow of 4.8 sccm.	80
Figure 3.13. Images of the reactor channel taken with an Intensified Charge Coupled Device (ICCD) camera, to show the effect of the flow rate in the reactive mixture (ml.min ⁻¹) a) 48, b) 36, c) 24 d) 14.4, e) 9.6, f) 4.8 at a constant Power of 3W.....	81
Figure 4.1. Methane conversion as a function of SIEM at different values of flow rate (4.8;14.4;24;48 sccm), constant value of O ₂ /CH ₄ ratio (0.5 v/v) and concentration or argon (0.375 v/v).....	85
Figure 4.2. Methane and oxygen conversion as a function of SIEM at constant value of O ₂ /CH ₄ ratio (0.5 v/v) and argon concentration (0.375 v/v).....	86
Figure 4.3. Selectivity of the POM's compounds (a) hydrocarbons (b) CO and H ₂ (c) CO ₂ as a function of SIEM at different values of flow rate (4.8;14.4; 24; 48 sccm), constant value of O ₂ /CH ₄ ratio (0.5 v/v) and concentration of argon (0.375 v/v).....	87
Figure 4.4. Percent of missing carbon as a function of SIEM at constant value of O ₂ /CH ₄ ratio (0.5 v/v) and concentration of argon (0.375 v/v).....	88
Figure 4.5. The methanol selectivity as a function of SIEM at different values of flow rate (4.8,14.4, 24, 48 sccm), constant value of O ₂ /CH ₄ ratio (0.5 v/v) and concentration of argon (0.375 v/v).....	89
Figure 4.6. H ₂ /CO and CO ₂ /CO as a function of SIEM at different values of flow rate (4.8;14.4; 24; 48 sccm), constant value of O ₂ /CH ₄ ratio (0.5 v/v) and concentration of argon (0.375 v/v).....	91
Figure 4.7. CO ₂ /CO ratio (a) and H ₂ /CO ratio (b) as a function of methane conversion at different conditions.....	92
Figure 4.8. Percent of methane conversion (a) and methanol selectivity (b) as a function of SIEM and methanol selectivity in function of methane conversion (c) at different values of argon's concentration (0,0.3,0.375 v/v), constant value of flow rate (48 sccm) and O ₂ /CH ₄ ratio (0.3 v/v).	94
Figure 4.9. Methane conversion (a) and methanol selectivity (b) as a function of SIEM; methanol selectivity as a function of methane conversion (c) at different values of O ₂ /CH ₄ ratio (0.14, 0.3, 0.5, 0.76, 1 v/v) and constant value of flow rate (48 sccm) without presence of argon.	98

Figure 5.1. Graphical description of 1D DBD plasma model.....	113
Figure 5.2. Graphical description of 0D and 1D DBD plasma model.....	115
Figure 5.3. Evolution of the instantaneous power (a) and the concentrations of the main radical species (b) during 2 nanoseconds of the simulation at constant tension equal to 10.8 (kV pp), O ₂ /CH ₄ ratio of 0.3 (v/v) and argon concentration equal to 0.375 (v/v).	116
Figure 5.4. Calculated current evolution during sinusoidal discharge. Applied voltage: 10 kV pp; frequency: 4 kHz. Initial mixture: Ar = 0,4 / CH ₄ = 0,4 / O ₂ = 0,2.....	118
Figure 5.5. Simulation results of total capacitive absorbed power during sinusoidal discharge. Applied voltage: 10 kV pp; frequency: 3 kHz. Initial mixture: Ar = 0,4 / CH ₄ = 0,4 / O ₂ = 0,2.	119
Figure 5.6. Mean total capacitive power values (simulated and experimental data) as a function of applied voltage amplitude and Argon molar fraction. Calculations for frequency at 3 kHz and O ₂ /CH ₄ =0.5.	120
Figure 5.7. Calculated evolution of ions and radicals as a function of time within 1 ms. Applied voltage= 6500V; frequency= 4kHz. Initial mixture molar fractions Ar=0.4/CH ₄ =0.4/O ₂ =0.2.	121
Figure 5.8. Calculated evolution of main radicals as a function of time within 0.017 s. Applied voltage= 6500V; frequency= 4kHz. Initial mixture molar fractions Ar=0.4/CH ₄ =0.4/O ₂ =0.2.	122
Figure 5.9. Products evolution during sinusoidal discharge. Applied voltage: 5kV; frequency: 4kHz; Initial mixture: Ar=0,4/ CH ₄ =0,4/O ₂ =0,2.....	123
Figure 5.10. Products evolution during sinusoidal discharge a) linear scale et b) logarithmic scale. Applied voltage: 5kV; frequency: 4kHz; Initial mixture: Ar=0,2 / CH ₄ =0,53/O ₂ =0,27.	124
Figure 5.11. Comparison between the experimental and simulated behavior of the energy dissipated during one period as a function of the concentration of argon at constant O ₂ /CH ₄ ratio of 0.3 (v/v).	127
Figure 5.12. Experimental and simulated comparison of the energy applied as a function of the O ₂ /CH ₄ ratio without presence of argon.	128
Figure 5.13. Rate of production of radicals in a single discharge with different concentrations of argon at constant value of tension equal to 10.8 kV and ratio O ₂ /CH ₄ equal to 0.3.	129
Figure 5.14. The rate of production of radicals in a single discharge at different ratios of O ₂ /CH ₄ without argon and constant value of tension equal to 10.8 kV.	130
Figure 5.15. The simulated energy (J/period) requirement in both models (sinusoidal and multi-scale time) at constant O ₂ /CH ₄ ratio equal to 0.5 (n/n)	131
Figure 5.16. Methane conversion (a) and the main products formed (b) for the two different models (sinusoidal and discharge-postdischarge) at SIEM = 70 kJ/mol _{methanein}	132
Figure 5.17. Experimental and simulated methane conversion in function of SIEM at different values of O ₂ /CH ₄ ratio in the absence of argon.	135
Figure 5.18. Experimental and simulated methane conversion in function of SIEM at different values of argon concentration.	136
Figure 5.19. Methanol selectivity as a function of methane conversion, as a comparison between experimental and simulated data at different values of argon's concentration (0, 0.3, 0.375 v/v), constant value of flow rate (48 sccm) and O ₂ /CH ₄ ratio (0.3 v/v).	137
Figure 5.20. Methanol selectivity as a function of methane conversion, as a comparison between experimental and simulated data at different values of O ₂ /CH ₄ ratio (0.14, 0.5, 1 v/v) and constant value of flow rate (48 sccm) without presence of argon.	138

List of tables

Table 1.1. Main reactions in the Fischer-Tropsch synthesis, where n , x and y are integers and M represents a metal catalyst [17].....	25
Table 1.2. Subdivision of plasmas by temperature, where T_0 = gas temperature, T_i = ion temperature, T_r = rotational temperature, T_v = vibrational temperature and T_e = electron temperature (Hippler et al., 2001).....	30
Table 1.3. The main plasma processes. A and B represent atoms and M stands for a temporary collision partner [31].	32
Table 1.4. Comparison methanol selectivity and methane conversion by different authors	46
Table 3.1. Deposition protocol for ITO/Au/ITO films.	71
Table 3.2. Values of breakdown voltages for different pure gases and gas reaction mixtures at constant flow rate of 48 sccm	73
Table 3.3. Semi-empirical values of breakdown voltage for methane, oxygen and argon at 38 (Torr.cm), [29] c), [62] a), b).	74
Table 5.1. List of species included in the model for the $Ar/CH_4/O_2$ gas mixture.	110
Table 5.2. Experimental and simulated results in sinusoidal and multi-time scale	133